Nano-resonators for high resolution mass detection

Davis, Zachary James; Hansen, Ole; Boisen, Anja

Publication date:
2003

Document Version
Publisher's PDF, also known as Version of record

Nano-resonators for high resolution mass detection

Ph. D. Thesis

Zachary J. Davis[1]

March 31, 2003

[1]Mikroelektronik Centret, Technical University of Denmark, Building 344, 2800 Lyngby, Denmark

Preface

This thesis has been written as a partial fulfillment of the requirements for obtaining the Ph.D.-degree at the Technical University of Denmark (DTU). The Ph.D. project has been carried out at Mikroelektronik Centret (MIC) at DTU in the period from the 1st of February 2000 to the 31st of March 2003.

This Ph.D. project has been a part of the BioProbe project at MIC and has been supervised by the following people:

Project leader, Dr. Anja Boisen
Main supervisor

Associate Professor, Ole Hansen
Co-supervisor

This work has been funded by the EU NANOMASS project, which has lead to a strong collaboration of MIC with three other institutes namely the Electrical Engineering Department at the Universitat Autónoma de Barcelona (UAB), Instituto de Microelectrónica de Barcelona (IMB-CNM) and the Solid State department at Lund University (LU). This project was created by the collaboration of MIC with UAB back in 1998, when Gabriel Abadal was working on Si based resonators at MIC. Since then the common goal of creating a extremely flexible and highly sensitive resonator based mass sensor has fuelled the project from just a few people to almost 20 people to date, including four Ph.D. students at MIC.

I would like to thank the main driving forces behind the NANOMASS project, which are Nuria Barniol, Francesc Peréz-Murano and Gabriel Adabel. I would also like to thank the other members of the NANOMASS project, Jaume Verd for the work on the CMOS design, Xevi Borrisé which has worked on AFM lithography, F. Campabadal and Eduard Figueras, which have contributed to the CMOS integration and J. Esteve for all his support and ideas. I would also like to thank the Lund group Sara G. Nilsson and Ivan Maximov for their work on E-beam lithography and Lars Montelius for all his support and fruitful discussion.

The BioProbe project must also have their recognition. First of all, I would like to thank Anja Boisen, for her support and guidance and for giving me the chance to be a part of the BioProbe project. I would also like to thank Peter Rasmussen for his vast experience with cleanroom processing and for a fruitful friendship, Esko Forsn for his work on AFM fabricated cantilevers and for taking over my work so that I can write this thesis, Maria Holmberg for her help with some last minute AFM measurements, Ramona Matieu, Rodolphe Marie, Montserrat Calleja and Alicia Johansson for their overall friendship and support. Finally, I would like to thank Bjarne Helbo and Mingdong Dong for their undying efforts under my co-supervision. I don't think a better project or group exists that can collaborate and help each other on such a high plain.

I would also like to thank the rest of MIC for providing a really fruitful working atmosphere. A special thanks to Ole Hansen for his wisdom on just about everything and for his advice and help on the development on the SPICE model. Also I would like to thank the tovholder group for their friendship and the free-child meetings. Next, I would like to thank the administrative staff and the laboratory technicians for always having time to help in any way they can. A special thanks to Helle Vendelbo Jensen for her help with the thin resist UV lithography. I am also grateful to Jamil El-Ali, Christian B. Nielsen, Jacob Thaysen and Salim Bouaidat for a good friendship throughout my time at MIC. Finally, I would like to thank the director Pieter Telleman for supporting this project.

Yet the greatest thanks is to my wife and two adoring children, for their love, support and encouragement.

Kgs. Lyngby, March 31. 2003

Zachary James Davis
Mikroelektronik Centret, Building 345east
DK-2800 Kgs. Lyngby
Denmark

Abstract

Cantilever based sensors have been demonstrated to be a very flexible and wide ranging micro-electro mechanical system (MEMS). Compared to static mode, dynamic mode operation of cantilever based systems are able to measure both stress and pure mass changes of the cantilever. Furthermore, by reducing the dimensions of the sensor to the nanometer scale, the sensor can become faster, cheaper and more sensitive.

The goal of this Ph.D. project has been to design, fabricate and characterize a cantilever based mass sensor. The design of the device is based on electrostatic actuation of a laterally vibrating cantilever and the readout is based on measuring capacitance changes between the vibrating cantilever and a static parallel electrode. Furthermore, the width of the cantilever is to be reduced to the submicrometer scale in order to increase the mass sensitivity and spatial resolution.

In order to facilitate with the design a model of the capacitive based device has been developed. This model is based on SPICE and is able to simulate both the mechanical and electrical behavior of the device. It was found through simulations that the capacitive readout of the device is only possible if the parasitic capacitances are very low, due to the sub-micron dimensions of the cantilever device. This lead to the integration of the mass sensor with CMOS technology. By integrating the mechanical device with CMOS circuitry, the parasitic capacitances are reduced enough to achieve capacitive readout. Furthermore, the CMOS can be used to increase the functionality of the sensor.

It was decided that, as a first attempt, the fabrication of the cantilever will be a post processing module using one of the CMOS poly-Si layers. A post-processing sequence for fabricating 500nm wide laterally vibrating cantilevers on CMOS circuitry was developed. Furthermore, fabrication of cantilevers that have been defined by laser and E-beam lithography has been successful. In addition, single-crystal Si and Al, non-integrated cantilevers, have been fabricated using atomic force microscopy (AFM) and UV lithography respectively.

Non-electrical characterization has been performed on poly-Si test cantilever in

and out of vacuum in order to determine the sensor performance. Furthermore, electrical characterization of a CMOS integrated cantilever has also been performed.

Mass measurements have been performed using vertically vibrating Al cantilevers. The measurements have been performed in vacuum using the SEM detector signal as a readout for the cantilever. Electron beam induced deposition (EBID) was used to deposit carbon on the apex of the cantilever.

Dansk Resume

Bjælke baseret sensorer har demonstreret at være et meget fleksibelt mikroelektro mekanisk system (MEMS). I forhold til statisk mode, kan dynamisk mode bjælkebaseret systemer både måle stres og masseændringer på bjælken. Sensoren kan blive hurtigere, billigere og mere følsom ved at reducere bjælkens dimensioner.

Formålet med dette Ph.D. projekt har været at designe, fremstille og karakterisere en bjælkebaseret massesensor. Designet af komponenten er baseret på elektrostatisk aktuering af en lateral vibrerende bjælke, og udlæsning af bjælkens udbøjning sker ved at måle kapacitance ændringer mellem den vibrerende bjælke og en stationær elektrode. Desuden skal bredden af bjælken reduceres til under 1 mikrometer, for at optimere sensorens masseføls omhed og dens rummelige sensitivitet.

For at letteregøre designet at massesensoren, blev en model udviklet, som kan modellere det kapacitive system. Modellen er baseret på SPICE og kan simulere både den elektriske og mekaniske opførsel af komponenten. Da bjælkens dimensioner er meget små , blev det fundet at den kapacitive udlæsning af komponenten kun kan lade sig gøre, hvis de parasitiske kapacitancer er meget lave. Dette fund giver anledning til at komponenten bliver integreret med CMOS-teknologi. Ved at integrere bjælken med et CMOS-kredsløb kan de parasitiske kapacitancer reduceres nok til at muliggøre den kapacitive udlæsning. Desuden kan CMOS'en bruges til at forøge funktionaliteten af sensoren.

Det første forsøg på at integrere CMOS og bjælker er efter-fremstilling af et af CMOS'ens poly-silicium lag. Der blev udviklet en efter-proces der kan fremstille 500nm brede bjælker på en CMOS chip. Desuden, er bjælker defineret med laser og EBL blevet fremstillet. Udover disse poly-silicium bjælker, er enkeltekrystallinske-silicium og aluminiumsbjælker også blevet fremstillet, uden CMOS.

Ikke-elektriske karakteriseringer er blevet gennemført på poly-silicium test komponenter (uden CMOS) både i vakuum og i luft. Desuden er elektriske karakteriseringer blevet gennemført på en CMOS integreret poly-silicium komponent.

Massemålinger er blevet gennemført ved brug af en vertical vibrerende Al bjælke. Målinger er udført i vakuum, og udlæsning foretaget ved brug af SEM'ens elektron detektor signal. Elektron induceret deponering blev brugt til at deponere kulstof på bjælken.

Contents

1 Introduction **1**
- 1.1 Cantilever based sensors . . . 1
  - 1.1.1 Static mode sensors . . . 2
  - 1.1.2 Dynamic mode sensors . . . 3
  - 1.1.3 Static versus dynamic mode . . . 4
- 1.2 Actuation and readout principles . . . 5
  - 1.2.1 Actuation methods . . . 5
  - 1.2.2 Readout methods . . . 7
- 1.3 CMOS integrated sensors . . . 9
- 1.4 The EU NANOMASS project . . . 10
  - 1.4.1 Application possibilities of the NANOMASS sensor . . . 11
  - 1.4.2 NANOMASS work package descriptions . . . 12
- 1.5 Overview of this thesis . . . 13
  - 1.5.1 Outline of chapters . . . 14

2 General Theory and Modelling **15**
- 2.1 Cantilever Theory . . . 15
- 2.2 SPICE Model . . . 18
  - 2.2.1 Large signal model . . . 19
  - 2.2.2 Symmetric cantilever . . . 22
  - 2.2.3 SPICE implementation . . . 24
- 2.3 Spring softening effects . . . 26
  - 2.3.1 Frequency noise . . . 27
- 2.4 Fringe effects . . . 28
- 2.5 Non-linear effects . . . 30
- 2.6 SUGAR model . . . 30
  - 2.6.1 Snap-in voltage simulations . . . 31
  - 2.6.2 Fringe factor effects . . . 32
- 2.7 Summary . . . 33

3 Lithography Techniques **35**
- 3.1 UV lithography . . . 35
- 3.2 Laser lithography . . . 37

3.3 AFM lithography . . . 38
3.4 E-beam lithography . . . 39
3.5 Summary . . . 41

4 CMOS Circuitry Design and Fabrication 42
4.1 General design considerations . . . 42
4.1.1 Parasitic capacitances . . . 42
4.1.2 One versus two electrode configuration . . . 45
4.2 CMOS technology . . . 46
4.3 Circuit design . . . 49
4.3.1 BS circuits . . . 49
4.3.2 AC circuits . . . 50
4.4 1st Generation chip design and layout . . . 51
4.4.1 BS circuit . . . 51
4.4.2 AC circuit . . . 53
4.4.3 1st generation problems . . . 53
4.5 2nd generation chip design and layout . . . 54
4.5.1 BS circuit . . . 54
4.5.2 AC circuit . . . 55
4.6 Summary . . . 57

5 CMOS Integrated Cantilevers 60
5.1 Poly0 optimization . . . 60
5.2 Process sequence . . . 61
5.3 Mask definition . . . 63
5.3.1 Laser fabricated cantilevers . . . 63
5.3.2 EBL fabricated cantilevers . . . 70
5.3.3 AFM defined cantilevers . . . 71
5.4 Dry release techniques . . . 72
5.4.1 Freeze-drying technique . . . 74
5.4.2 Resist technique . . . 75
5.5 Anti-stiction layers . . . 77
5.6 Post-processing effects on CMOS . . . 78
5.6.1 Metal deposition effects . . . 79
5.6.2 SEM and EBL effects . . . 79
5.7 Summary . . . 80

6 Non Integrated Cantilevers 83
6.1 AFM defined Si cantilevers . . . 83
6.1.1 Process sequence . . . 83
6.1.2 Local oxidation with AFM . . . 84
6.1.3 Fabrication results . . . 89
6.2 Metal cantilevers . . . 93

6.2.1 Fabrication process 94
6.2.2 1st generation metal cantilevers 96
6.2.3 Future generation metal cantilevers 98
6.2.4 CMOS integration 98
6.3 Summary 98

7 Characterization 100
7.1 Non-electrical characterization methods 100
7.1.1 Visual characterization 100
7.1.2 SEM characterization 101
7.1.3 AFM characterization 101
7.2 Characterization of poly-Si cantilevers 103
7.2.1 Air measurements 105
7.2.2 Vacuum measurements 109
7.2.3 Air versus vacuum measurements 113
7.3 CMOS integrated cantilevers 114
7.3.1 Visual measurements 114
7.3.2 Electrical measurements 114
7.3.3 Electrical characterization summary 119
7.4 Metal cantilevers 119
7.4.1 Dynamic measurements 119
7.4.2 Mass measurement 121
7.5 Summary 123

8 Conclusions 124

A List of publication 141

B SUGAR program 144

C CMOS post processing sequence using laser lithography 147

D Freeze-drying process sequence 148

E Resist-release process sequence 149

F Al cantilever process sequence 150

List of Figures

1.1 Static mode detection principle 2
1.2 Dynamic mode sensor 3
1.3 Resonant sensor principle 6
1.4 NANOMASS mass sensor concept 10

2.1 Laterally vibrating cantilever 16
2.2 Mass spring model 17
2.3 Capacitive system diagram 19
2.4 Equivalent electrical network 21
2.5 Final spice model 24
2.6 Fringe factor approximation 29
2.7 Frequency response simulations 30
2.8 Non-linear frequency response simulations 31
2.9 SUGAR simulations 32
2.10 Snap-in simulations using SUGAR and SPICE 33
2.11 SUGAR simulation, snap-in versus fringe factor 34

3.1 UV lithography schematic 36
3.2 Laser lithography setup 38
3.3 AFM lithography setup 39
3.4 EBL setup 40

4.1 Mass sensor design 43
4.2 SPICE simulations 43
4.3 SPICE simulations 44
4.4 SPICE simulations 46
4.5 SPICE simulations 47
4.6 CNM CMOS process sequence 48
4.7 BS circuit diagram 49
4.8 AC circuit diagram 51
4.9 1st generation chip layout 52
4.10 1st generation BS circuit layout 52
4.11 1st generation AC circuit layout 53

4.12 2nd generation chip layout 54
4.13 2nd generation BS circuit layout 55
4.14 BS circuit characterization 56
4.15 2nd generation AC circuit layout 57
4.16 2nd generation AC circuit layout 57
4.17 2nd generation AC circuit layout 58
4.18 Frequency response of BS and AC circuit 58

5.1 poly0 surfaces 61
5.2 Post processing sequence 62
5.3 Laser defined masks 64
5.4 Laser writing concept 65
5.5 Laser writing concept 66
5.6 Laser defined cantilever on CMOS 67
5.7 SEM images of Al surfaces 68
5.8 AFM images of Al surfaces 69
5.9 EBL fabrication results 70
5.10 SEM images of EBL defined cantilevers 71
5.11 AFM defined patterns on CMOS chip 73
5.12 Stiction cantilevers 74
5.13 Freeze-drying setup 75
5.14 Contaminated surface after freeze-drying 75
5.15 Freeze drying process sequence 76
5.16 Resist encapsulated cantilever 77
5.17 Test CMOS chip 78
5.18 Test cantilevers on CMOS 79
5.19 Metallization effects on CMOS 80
5.20 SEM effects CMOS 81

6.1 Fabrication process using AFM lithography 84
6.2 Cantilever versus tip/sample displacement 85
6.3 Contact versus adhesion mode AFM 86
6.4 Waterbridge illustration 88
6.5 Nc-AFM oxidized patterns 88
6.6 Nc-AFM oxide lines 89
6.7 Aligning with adhesions mode AFM 89
6.8 Poly-Si cantilever defined by AFM lithography 91
6.9 AFM and laser lithography 91
6.10 AFM and laser defined device 92
6.11 AFM and laser defined device 92
6.12 Process sequence for Al cantilevers 95
6.13 Al mask layout 96
6.14 Al structure on Si substrate 97

6.15 Al cantilever before and after underetching 97

7.1 Visual characterization setup 101
7.2 SEM characterization setup 102
7.3 Ceramic chipcarrier, holder and cables 102
7.4 AFM characterization setup 103
7.5 Poly-Si non-integrated cantilevers 104
7.6 Static visual measurement 106
7.7 Static AFM measurement 107
7.8 Frequency response of device1 108
7.9 Resonant frequency versus sum of applied voltages squared in air 108
7.10 Static measurements in SEM 110
7.11 Static measurements in SEM 110
7.12 1st and 2nd mode of cantilever 111
7.13 Frequency response in vacuum 112
7.14 Resonant frequency versus sum of applied voltages squared in vacuum 113
7.15 Lateral vibration of CMOS integrated cantilevers 115
7.16 Parasitic capacitance diagram 116
7.17 Output voltage versus the gate voltage and input voltage 116
7.18 Electrical readout of laser cantilever 117
7.19 Resonant frequency versus the sum of the applied voltage squared 118
7.20 Electrical measurement and SPICE simulations 118
7.21 Vertical vibration of Al cantilever 120
7.22 Frequency response of Al cantilever 121
7.23 Frequency response using SEM detector 122
7.24 Al cantilever before and after carbon deposition 122

List of Tables

2.1 Mass resolution for different cantilever dimensions. 18
2.2 The frequency noise due to voltage noise for three devices 28

3.1 Summation of the lithography techniques 41

5.1 poly0 roughness values 61
5.2 Roughness value for Al coated Si and SiO_2 surfaces 70

6.1 mass resolution for different materials with a given cantilever dimensions 93
6.2 mass resolution for different materials with a length calculated for a given stiffness 94

7.1 Main findings of the characterization of poly-Si cantilevers in air . 109
7.2 Main finding of the characterization of poly-Si cantilevers in vacuum 113
7.3 Comparison of air and vacuum measurements on the same cantilevers 114
7.4 Main finding of the characterization of CMOS integrated poly-Si cantilevers in air 119

Chapter 1

Introduction

In the beginning of the 1970's technologies generated from the microelectronics industry started to be used for fabrication of mechanical systems, so called micro electro-mechanical systems (MEMS)[1]. Since then, micrometer scale mechanical systems have been moving towards nanometer scale mechanical systems or nano electro-mechanical systems (NEMS). Miniaturization from the micro to nano scale offers the potential for faster, cheaper and more sensitive sensors.

1.1 Cantilever based sensors

One of the most flexible mechanical sensor systems is the cantilever based sensor [2][3]. The main feature of a cantilever based sensor is transducing the mechanical behavior of the cantilever into a measurable signal, where the mechanical properties are altered by physical changes in the environment. Cantilever based sensors have a wide range of applications. Cantilevers have been demonstrated in such applications as gas, temperature, pressure, biological and force sensors [4][5][6][7][8][9][10][11][12][13]. The two types of operation modes of a cantilever based sensor are static and dynamic mode. In static mode the bending of the cantilever is used to transduce the desired physical quantity to a measurable signal. In dynamic mode the cantilever's resonant behavior is used, where shifts in the resonant frequency and the damping of the cantilever transduce the physical quantities.

One of the first cantilever based sensors is the atomic force microscope (AFM), invented by Binning *et al.* in 1986 [14]. In AFM, a tip is integrated onto the apex of a cantilever and forces acting on the tip are transduced using static or dynamic mode [15][16]. In static mode AFM, the tip is typically in contact with the surface and by scanning the cantilever across the surface and measuring the bending of the cantilever, the topography of the surface is obtained. In dynamic mode, the tip is not in full contact with the surface and the resonant frequency

shift due to the atomic forces acting on the tip serves as a measurement of the surface topography. Force sensitivities down to 10^{-10}N are routinely achieved [16].

1.1.1 Static mode sensors

If the field of chemical or biological sensors the induced surface stress when molecules are immobilized onto a surface induces a bending of the cantilever. In this case the whole cantilever surface acts as the sensor and not the tip at the cantilever apex as in AFM. A schematic drawing of the principle can be seen in figure 1.1, where in (a) the cantilever is stress free and in (b) bending is induced by molecular immobilization. Several examples of surface stress sensors have been demonstrated and typically a surface stress of 10^{-5}N/m can be detected [17].

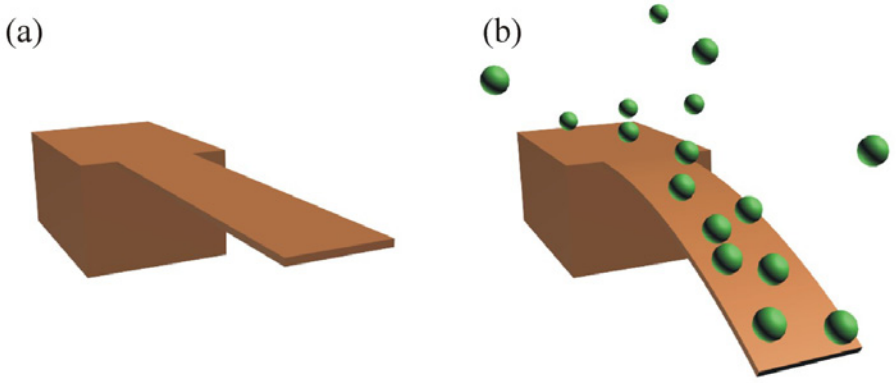

Figure 1.1: In (a) the cantilever is stress free and in (b) molecules have immobilized on the surface inducing surface stress and bending of the cantilever.

Several papers have demonstrated detection of alcohols in gas phase. These experiments have been performed by coating the cantilever with a polymer layer [18][19]. The cantilever is placed in a chamber where the alcohol is introduced and absorbs into the polymer, inducing stress into the cantilever, due to swelling of the resist. Partial pressures on the μl range has been demonstrated for different alcohols.

The detection of immobilization of single stranded DNA oligonucleotides and hybridization of the complementary oligonucleotide has been demonstrated by Fritz *et al.* [20] and Wu *et al.* [21] . In this experiment gold coated cantilever surfaces where functionalized by thiolated probe DNA. Then the target DNA strand is introduced and by measuring the static bending of the cantilever by optical means, the surface stress change induced by the hybridization was observed.

Concentrations on the nM scale have been measured. Selectivity between 12-mer oligonucleotides with one base differences has also been demonstrated.

Thaysen *et al.* [22] describe a novel piezoresistive readout of the cantilever bending, which is independent of the bulky optical readout system traditionally used. This sensor is integrated in a fluid handling system with inlets and outlets and ten cantilever sensors per chip. Measurements of gold etching and immobilization of thiolated probe DNA on gold have been achieved.

1.1.2 Dynamic mode sensors

There have also been numerous dynamic mode sensors, where not only stress changes can be measured but mass changes of the cantilever as well. The schematic principle of operation can be seen in figure 1.2. In (a) the cantilever is vibrating at its resonant frequency and in (b) the added mass and stress, due to the immobilization of molecules, shifts the resonant frequency.

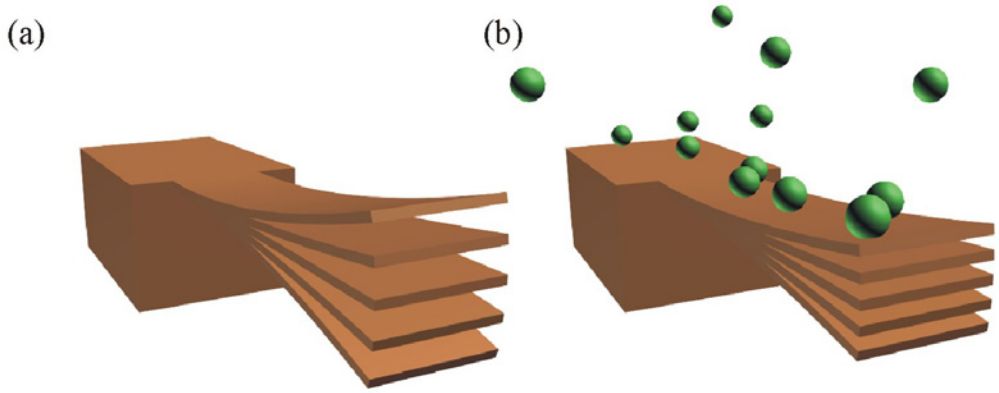

Figure 1.2: In (a) the cantilever is vibrating at its resonant frequency and in (b) the resonant frequency shifts due to the added molecules.

Through a theoretical treatment of a cantilever based sensor, Sader *et al.* [23] have found that the resonant frequency shift, due to the deposition of an evenly distributed mass on the cantilever surface, is induced by a surface stress change as well as a mass increase. Furthermore, the two components can be separated.

Baltes *et al.* [24][25] have demonstrated high sensitivity alcohol measurements on a cantilever integrated with CMOS circuitry. The cantilever is excited thermally and an integrated piezoresistor reads out the cantilever's vibrational amplitude. A thin polymer layer is deposited on the cantilever and the absorbed alcohol is

measured by measuring the resonant frequency shift of the cantilever.

Yang *et al.* [26] and Cleland *et al.* [27] have demonstrated the fabrication of nanometer sized resonant structures. The feature size of the mechanical sensor is defined by E-beam lithography. The actuation and detection principle is magnetomotive. The excitation of the device is achieved by passing an AC current through the beam structure and applying a high magnetic field perpendicular to the device, which generates a Lorentz force that drives the beam. The readout is performed by measuring the electromotive force (EMF) across the beam. The deposition of gold has been detected with a sensitivity in the attogram range [28].

Several gas sensors have also been demonstrated, where the mass change of a polymer coated cantilever due to chemical gas absorbtion has been performed [29][30][31][32].

Yang *et al.* [33] have measured hydrogen absorbtion in carbon nanotubes with ultra thin cantilevers with a thickness down to 20nm. A bundle of nanotubes is attached to the apex of the cantilever and the cantilever is placed in a vacuum chamber. The cantilever is excited by a piezo-actuator and the readout is achieved by a laser doppler system. After measuring the resonant frequency of the nanotube bundle the cantilever is placed in a hydrogen gas so that the nanotubes absorb the gas. Then the cantilever is placed back into the vacuum chamber and the resonant frequency is measured again. This system also demonstrated attogram sensitivity [34].

The ultimate mass sensor, based on a nanotube cantilever, has been demonstrated by Wang *et al.* [35]. In this experiment a TEM is used to observe individual nanotubes in a bundle. An electrode is approached from the top and the outermost nanotube in the bundle is excited electrostatically and the vibration of the nanotube is observed by the TEM. Then a latex sphere is attached to the apex of the nanotube and the resonant frequency is measured again. With this sensor a mass sensitivity of 10^{-20}g/Hz is reported, which is the best mass sensitivity achieved to date.

1.1.3 Static versus dynamic mode

Static mode detection of biochemical species depends on the induction of surface stress changes on the cantilever surface. This means that the absorbtion or immobilization of the biochemical species must be on only one side of the cantilever in order to maximize the measurable stress signal. This is usually achieved by funtionalizing one side of the cantilever so that only one surface is receptive to the wanted biochemical species. The problem of unspecific binding of the wanted or other biochemical species to non-functionalized surfaces is always an issue.

With dynamic mode measurements, both surface stress changes and mass changes of the cantilever can be detected. This means that the desired biochemical species do not have to be confined to one side of the cantilever but the entire surface area can be used. Thus unspecific binding to the back-side of the cantilever is not a problem.

In dynamic mode both the resonant frequency and the damping of the cantilever can be measured. In this way more information can be accessed by the sensor. Sader *et al.* and Chon *et al.* [36][37] have demonstrated that by measuring the cantilever's resonant frequency and damping effects, the viscosity and density of the gas or fluid around it can be determined, without the need for functionalization of the cantilever. This type of measurement is impossible with static mode detection.

The sensitivity of a static mode biochemical sensor is dependent on the interaction forces between the molecules in a biochemical detector. Typical values of surface stress induced by hybridization of target DNA with probe DNA is on the order of 3×10^{-3}N/m [38]. Hansen *et al.* have estimated that for probe immobilization, with a probe density of approximately 10^{13} strands of ssDNA/cm^2, which leads to an approximate sensitivity of 5pg/nm [39] for static mode. Ilic *et al.* has demonstrated cell detection in air with mass sensitivities of 0.13pg/Hz [40] for dynamic mode. The main disadvantage of dynamic mode is that operation in liquids is more complicated and that damping of the cantilever reduces the sensitivity.

1.2 Actuation and readout principles

A schematic diagram of the resonant sensor principle is shown in figure 1.3. The sensor consists of the vibrating mechanical structure and an actuation and detection unit. The actuation unit actuates the mechanical structure into resonance and the readout unit converts the vibration of the sensor into an electrical signal. The signal can then be feed back to the actuation unit in order to maintain peak resonance of the structure. Some of the most common actuation and readout schemes are described below.

1.2.1 Actuation methods

Electrostatic actuation

This technique uses two electrodes where one of the electrodes is the resonator structure. By applying an alternating voltage between the driver plate and the resonator structure one exerts a periodic force on the resonator, thus actuating it.

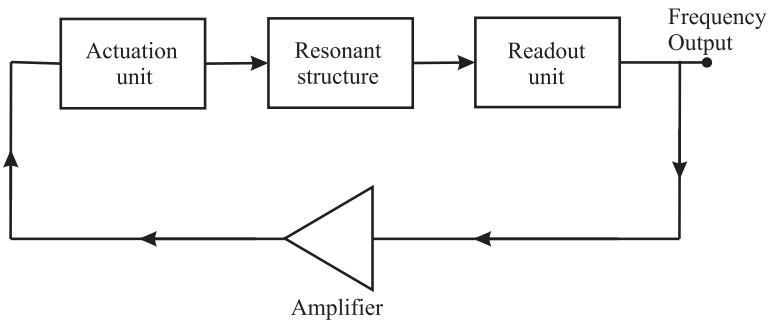

Figure 1.3: Diagram of the resonant sensor principle, which consists of an actuation unit, a vibrating structure and a readout unit.

This technique is very good when working in vacuum, since air would otherwise damp the motion on the resonator. Otherwise, one has to ensure easy airflow around the resonator. This type of actuation has been used for AFM cantilevers by Blanc *et al*. [41].

Piezoelectric actuation

This technique utilizes the electromechanical coupling found in piezoelectric materials, such as single-crystalline quartz. The technique is to sandwich a piezoelectric material between two metal contacts, which is then placed on a silicon resonator. By again applying an alternating voltage across the piezoelectric material, one can actuate the resonator. The drawbacks of this technique are that most piezoelectric materials are not easy to work with and are not cleanroom compatible, containing Zr oxides [42]. Cleland *et al*. [43] have fabricated nanometer sized piezoelectric aluminum nitride resonant structures, which might be used for this actuation principle.

Thermal actuation

This technique uses the bi-morph effect of a cantilever with several layers each having a different thermal expansion coefficient. The cantilever is heated by placing a resistor on or near the cantilever. When a current is passed through this resistor, the temperature rises locally on the resonator and the material expands, bending the resonator due to stress. Usually the resistor is an integrated diffused resistor, or poly-Si that is deposited on the resonator. This method is good since it requires no external drivers, but if one wanted to do an in-situ measurement the heat could possibly deflect or damage the particles to be detected. Furthermore, dynamic oscillation would require that the expanding material has a fast cooling time constant, in the order of 10^{-5} second, which requires careful design. Thermal actuation has been demonstrated to dynamically excite a cantilever up to

16kHz in GaAs cantilever beams [7]. Furthermore, resonant frequencies as high as 400kHz have been actuated and actuation frequencies in the MHz range are claimed to be possible, with cantilevers integrated on CMOS circuitry [24][25]. Thermal actuation has primarily been used for static actuation [44][45], due to the large forces that can be induced.

Instead of heating, the natural thermal vibrations, due to fluctuations in the temperature of the structure can be used. For a cantilever the vibrational amplitude is dependent on the square root of the temperature and the square root of the inverse spring constant of the cantilever. This type of thermal actuation has been demonstrated by *Ilic et al.* [40]. By scaling down the dimensions of the cantilever the relative vibrational amplitude increases. The challenge is to accurately measure the vibration of the cantilever, due to the small vibrational amplitude. This method can be coupled with the resistive heating, by passing a DC current through a resistor on the cantilever, which increases the temperature and thus the thermal vibrational amplitude of the structure.

Magnetomotive actuation

This is done by applying a static magnetic field perpendicular to a beam structure and alternating an AC current through the beam. The Lorenz forces acting on the electrons will drive the beam. The advantages are that this is a rather straight forward and simple method. The disadvantages are that in order to achieve a large actuation force, large magnetic fields need to be applied. This technique or similar techniques has been demonstrated in other works [26][46][47].

Magnetic actuation

In this method the cantilever is a magnetic material and an oscillating magnetic field is applied parallel to the vibration of the cantilever. The magnetic field induces a force on the cantilever. Several examples of this actuation method have been demonstrated [48][49]. The main problem with this method is the need for a magnetic material on the cantilever and the aligning of the magnetic field to the cantilever.

1.2.2 Readout methods

Capacitive readout

This detection technique can be used in the first three excitation setups discussed above. The idea is that two electrodes separated by any material has a capacitance and this capacitance changes when the distance between the electrodes changes. Thus, one can detect the resonance of the resonator by measuring the capacitance. The method has been demonstrated as the integrated readout of an

AFM sensor by Blanc *et al.* [41]. Sensitivities at the sub-Ångström have been achieved with this method [50][51].

Piezoresistive readout

This is an often used readout technique since both single-crystal Si and poly-Si are good piezoresistive materials at the right doping level [52][53]. The idea is that when the resonator bends, the resistance of the piezoresistor changes due to the stress in the material. Thus, one could detect the bending of a cantilever by simply measuring the resistance of the piezoresistor. A drawback for this detection method is that one needs to have a circuit on the actual resonator structure. This limits the minimum size of the resonator in the case of the cantilever, because one needs two contacts to the cantilever. Piezoresistive readout has been demonstrated for Si based AFM cantilevers [54][55], Si based gas flow sensors [56][57] and even plastic based stress sensors [58]. Displacement sensitivities of $(\Delta R/R)/\text{Å}=1.1 \times 10^{-5}$ have been demonstrated [59].

Optical detection

The movement of the cantilever is detected by reflecting a laser beam off the cantilever and onto a position sensitive photo diode. When the cantilever bends, the movement is registered by the photo diode. This method is used in most AFM microscopes. However, since the typical laser spot diameter is approximately 10μm, the minimal size of the mechanical device is limited. Another disadvantage is that this type of detection method requires a laser and photo diode, which takes up lots of space, and is not compatible with some possible applications. Sub-Ångström unit sensitivity is routinely achieved with this method [16].

Summary

In order to have a mass sensor device, which has an integrated readout and actuation unit and which has the potential to have a high sensitivity, the electrostatic actuation and capacitive readout are among the best choices. This allows the design of a simple cantilever system, which does not contain several layers, thus the dimensions of the sensor can be scaled down. Furthermore, the capacitive readout can be integrated on the same chip, which will provide a very compact and highly sensitive sensor. Other advantages of a capacitive system are low power consumption, wide operating temperature range, ease of trimming and good linearity [60].

1.3 CMOS integrated sensors

The main problem of capacitive systems is the presence of parasitic capacitances [61], which can degrade or even destroy the mechanical capacitive signal. Furthermore, as the dimensions of the sensor decrease so does the capacitive signal that needs to be measured. The solution of this problem is to integrate the mechanical sensor with an Integrated Circuit (IC). The IC is used to amplify and handle the capacitive signal. The integration of IC can lead to a so-called "smart sensor", which has several functionalities built-in to the sensor, such as self calibration, resonant frequency tracking and Q-factor enhancement [62][63][64][65].

Typically, integration of a mechanical sensor with IC is done through monolithic integration with standard complementary metal-oxide-silicon (CMOS) technology. Several approaches of CMOS integrated mechanical systems have been seen. The three main approaches to CMOS integration are pre-CMOS, intermediate CMOS and post-CMOS integration.

Pre-CMOS integration

In pre-CMOS integration the mechanical system is fabricated before the CMOS. The main disadvantages of this method is that normal IC fabs do not allow pre-processed wafers in their CMOS line, in order to keep the reproducibility of their processes stable. Some examples of pre-CMOS integrated systems are the accelerometer and gyroscope sensors fabricated by Sandia National Labs [66], where poly-Si structures are first surface micromachined in the wafer and then the mechanical structures are protected by SiO_2 filling during the CMOS fabrication. Examples of bulk micromachining, pre-CMOS integration, is the pressure sensor developed by Chavan *et al.* [67]. First a membrane is bulk micromachined into the wafer, then the CMOS is fabricated. The membrane is vacuum sealed by wafer-bonding the CMOS wafer with a glass wafer.

Intermediate CMOS integration

Intermediate CMOS integration involves surface micromachining of the CMOS layers during the CMOS fabrication. This demands an IC fab that has micromachining facilities. The advantage of this process is that it is very flexible and diminishes the overall complexity of the fabrication. An example is the Infineon Technologies Pressure IC, where a poly-Si membrane is surface micromachined with the BiCMOS circuitry [68]. The membrane is released by wet chemical etching the sacrificial layer through holes on the front side of the structure. Then the cavity is hermetically sealed by oxidation under a controlled pressure, which closes the holes.

Post-CMOS integration

Probably the most used integration technique is the post-CMOS integration. In this method the mechanical structure is fabricated after the CMOS. The main reason why it is the most used method is simply that most research centers do not have their own IC fab and are forced to buy IC circuits from outside fabs. It is possible to use add-on structural layers instead of using the CMOS layers, which adds to the flexibility. Furthermore, both surface and bulk micromachining can be performed. Examples of post-CMOS integration are the electroplated ring gyroscope [69][70], resonant cantilever based gas sensors [24][25][71] and an AFM probe [72][73].

1.4 The EU NANOMASS project

In order to develop a highly sensitive and versatile mass sensor the NANOMASS project was initiated in the beginning of the year 2000. The main goals of NANOMASS are:

(1) Development of technologies for combining CMOS processing with novel micro-nano processing.

(2) Development of techniques for fabricating a nanometer-sized cantilever based mass sensor, which is integrated with CMOS circuitry.

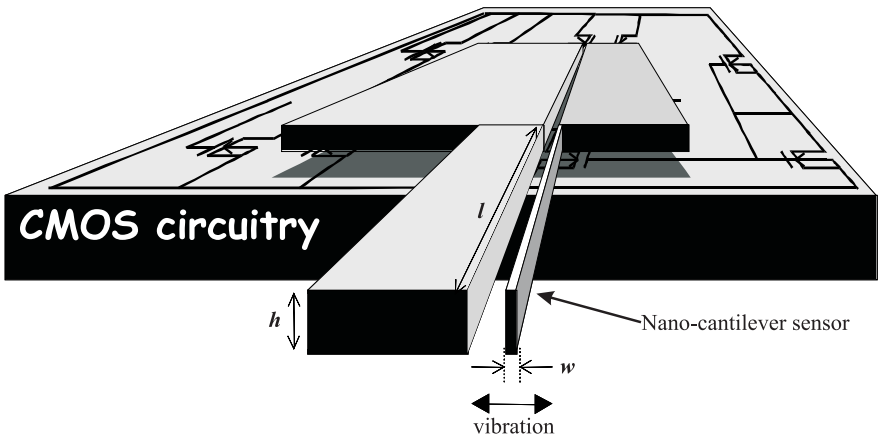

Figure 1.4: Conceptual drawing of the NANOMASS mass sensor.

The concept of the NANOMASS sensor is seen in figure 1.4. The device consists of a resonating nano-cantilever and CMOS circuitry. The cantilever is electrostatically driven into resonance and the vibration of the cantilever is monitored

by measuring the capacitance change in the system. The CMOS circuitry is necessary for the capacitive readout to function and can be used for increasing the functionality of the sensor. The design of the sensor aims at making the mechanical device as small as possible in order to increase the mass sensitivity. This design will allow both high mass sensitivity and high spatial resolution, since the width of the cantilever is the thinnest dimension.

The NANOMASS project is a joint venture between four European research institutes. The partners are:

(1) The electrical engineering department at the Universitat Autònoma de Barcelona (UAB)

(2) Instituto de Microelectrònica de Barcelona (IMB-CNM)

(3) Solid State department at Lund University (LU)

(4) Mikroelektronik Centret at the Technical University of Denmark (MIC)

The four collaborators handle different aspects of the realization of the mass sensor device. UAB and CNM work mainly on circuit design, modelling and fabrication of the CMOS circuitry. MIC and LU are responsible for fabrication of the mechanical cantilever using novel nanolithography techniques, such as laser, AFM, e-beam and nanoimprint lithography. Furthermore, MIC along with UAB is responsible for characterizing the final mass sensor, and finding suitable applications for the mass sensor.

1.4.1 Application possibilities of the NANOMASS sensor

The main goal of NANOMASS is to produce a highly versatile mass sensor, which can be used both in vacuum and in air applications. Some of the main application possibilities are:

Mapping spatial distribution of molecules or atoms

The NANOMASS sensor can be used for the calibration or characterization of evaporation systems, atom beam lithography (ABL)[74][75], molecular beam epitaxy (MBE) [76][52] and focussed ion beam (FIB) [52] systems. This implies that the performance of the device needs to be better than commercial products such as quartz microbalances, which can have sensitivities down to 10^{-12}g/cm^2 [77][78]. Furthermore, a high spatial resolution is needed for most of these applications, which is not possible in other sensor systems.

Vacuum/environmental detector

If the sensor is sensitive enough the out-gasing or absorption of molecules in vacuum, to a sensitive layer on the cantilever, can be detected at extremely low gas pressures.

Bio/chemical sensing

With such a highly sensitive mass sensor the study of single molecular interactions could be possible. Furthermore, an array of cantilevers, each with a specific functionalization, could be used as a highly sensitive detector of bio/chemical agents, such as explosives, anthrax and other hazardous or non-hazardous bio/chemical agents.

1.4.2 NANOMASS work package descriptions

The NANOMASS project is divided in work packages (WP), which work on different aspects of the NANOMASS project. These work packages are:

- WP1 (**Fabrication of sensors based on poly-Si cantilevers**) This work package is based on fabricating the cantilever with one of the poly-Si layers of the CMOS and is the first fabrication approach. The fabrication of the cantilever is based on post-CMOS surface micromachining. The main objective is the realization of cantilevers with a width down to 500nm, integrated with CMOS.
- WP2 (**Fabrication of sensors using SOI technology**) This work package is based on fabricating the cantilever in single crystal Si instead of in poly-Si. The challenge is to fabricate the standard CMOS circuitry using a silicon on insulator (SOI) wafer. This process requires some pre-processing of the SOI, after which the CMOS is fabricated. Finally, the cantilever is post-processed onto the circuit. This work package is still in the development phase of building the CMOS on the SOI substrate. The main objective is the development of 100nm wide cantilevers on CMOS circuitry.
- WP3 (**Fabrication of metal cantilevers**) In this work package metal will be used instead of Si as the cantilever material. The process will be based on the addition of an extra metal layer and surface micromachining. The first phase of this work package is to fabricate metal cantilever without CMOS and to characterize their performance. Then, if the performance is proven to be good, the metal cantilever will be integrated with CMOS circuitry. The first phase objective is to fabricate a 500nm wide cantilever.

- WP4 (**Fabrication of nano-cantilevers using electron beam lithography (EBL)**) In order to minimize the width of the cantilever EBL will be tested, due to its ability to pattern sub-100nm feature sizes [79][80]. The first objective is to investigate the compatibility of EBL and CMOS circuitry. Then, if EBL is compatible, cantilever fabrication will follow.

- WP5 (**Fabrication of nano-cantilevers using nanoimprint lithography (NIL)**) NIL will be used to scale up the production of 100nm wide cantilevers, through parallel processing. Again the objectives are to find whether or not NIL is compatible with CMOS circuitry. If it is compatible, NIL will be used to fabricate cantilevers on CMOS chips.

- WP6 (**Evaluation of applications**) This work package will evaluate the application potentials of the mass sensor and the design will be addressed accordingly.

- WP7 (**Functional evaluation**) In order to characterize the performance of the sensor several types of tests need to be performed, such as calibration of the mass sensitivity and spatial resolution. Furthermore, the evaluation of the sensor in both air and vacuum is needed. These evaluations will be used for future design considerations.

- WP8 (**Dissemination and implementation**) The main objectives here are to evaluate the industrial applications of the device and implementing the appropriate measures to further develop the demonstrators towards industrialization.

Besides the use of EBL and NIL, AFM lithography is also being investigated as a replacement of EBL. One of the main goals is to determine, which nanolithography technique is most compatible with CMOS technology.

1.5 Overview of this thesis

The aim of this thesis is the design, fabrication and characterization of a high sensitive, high spatial resolution mass sensor. Within the NANOMASS project the main work packages that are treated in this thesis are WP1, WP2, WP3 and WP7. Thus the main topics of this thesis are:

- The development of a model, which can both model the electrical and mechanical characteristics of a capacitive cantilever based resonator.

- The design and development of poly-Si cantilevers integrated with CMOS circuitry.

- The fabrication of single-crystal Si cantilevers with atomic force microscopy (AFM) lithography.
- The design and development of metal cantilevers without CMOS circuitry.
- The characterization of cantilevers in air and in vacuum conditions.

1.5.1 Outline of chapters

- In chapter two the general cantilever theory is introduced and two models are presented, which can be used to predict both the electrical and mechanical characteristics of the device.
- In chapter three a brief overview of the different lithography processes that have been used to realize the nano-cantilever is given.
- A brief description of the CMOS design is given in chapter four.
- In chapter five the fabrication of poly-Si cantilever on CMOS circuitry is described in detail and results are presented.
- Chapter six describes the fabrication of single crystal Si and metal cantilevers not integrated with CMOS circuitry.
- In chapter seven the characterization of the CMOS integrated and non-CMOS integrated cantilevers is presented. The characterization results are compared with the model presented in chapter two.
- Finally, in Chapter eight the main conclusions and achievements of this thesis are presented.
- Appendix A is a list of the articles and conference proceedings published during this project.
- Appendix B is the SUGAR program used to perform the SUGAR simulations.
- Appendix C is a detailed process sequence for poly-Si cantilevers integrated with CMOS circuitry.
- Appendix D is a detailed process sequence for the freeze-drying release method.
- Appendix E is a detailed process sequence for the resist release method.
- Appendix F is a detailed process sequence for the Al cantilevers.

Chapter 2

General Theory and Modelling

2.1 Cantilever Theory

In this section some general cantilever theory will be presented. Basically, this will involve a short description of how the cantilever's spring constant and resonant frequency are calculated. Furthermore, the mass resolution of a cantilever based mass detector will be addressed.

The spring constant of any given beam can be defined using Hook's law, which states that the bending of the beam will induce a force in the opposite direction of the bending, which is proportional to the bending and the stiffness or spring constant of the beam [15][16].

$$F = -k \cdot x \tag{2.1-1}$$

where F is the force, x is the bending and k is the spring constant, which is defined as [15]:

$$k = 3\frac{EI}{l^3} \tag{2.1-2}$$

where E is the Young's modulus, which is a material parameter concerning the elasticity of the cantilever material and I is the moment of inertia of the rectangular beam cross-section, which takes into account the geometry of the beam. For a rectangular beam, which has $I = \frac{hw^3}{12}$, the spring constant is:

$$k = \frac{Ehw^3}{4l^3} \tag{2.1-3}$$

where h and w are the height and width of the cantilever as seen in figure 2.1.

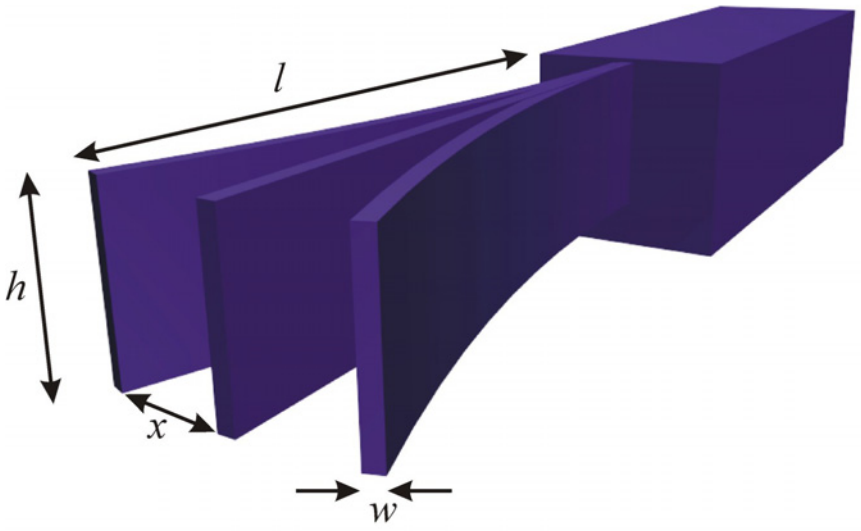

Figure 2.1: Simple cantilever with dimensions w, h and l, the width, height and length respectively. The displacement of the bending cantilever at the apex is denoted by x.

The resonant frequency of a simple spring and mass system, as shown in figure 2.2, is calculated by solving the equation of motion. The equation of motion with no external forces and no damping is:

$$m\ddot{x} + kx = 0 \tag{2.1-4}$$

where m is the dynamic mass of the system and k is the spring constant. A general solution for this equation is $x(t) = Asin(\omega t + \theta)$ and by inserting this into equation 2.1-4 the radial frequency ω can be isolated. The resonant frequency of the system is defined as:

$$f = \frac{\omega}{2\pi} = \frac{1}{2\pi}\sqrt{\frac{k}{m}} \tag{2.1-5}$$

In order to calculate the resonant frequency of a rectangular cantilever, which is rigidly clamped at one end, the dynamic mass of the system is:

$$m_{eff} = \frac{3m_0}{C_n^4},\ C_n = 1.875,\ 4.694,\ ... \tag{2.1-6}$$

where m_0 is the true mass of the cantilever, which is $m_0 = \rho lwh$, and C_n is a

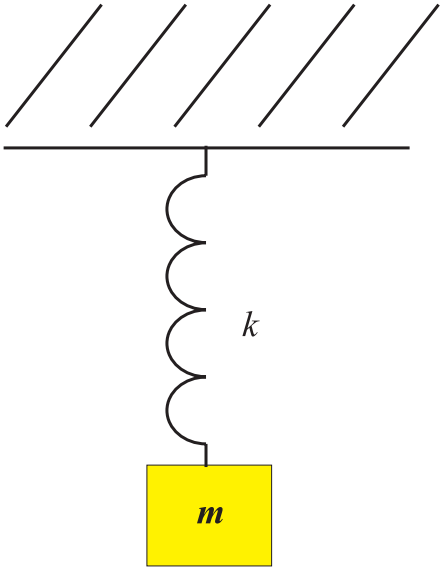

Figure 2.2: The simple spring and mass model with the spring constant k and mass m.

constant corresponding to the resonant mode of the cantilever. By inserting 2.1-6 and 2.1-3 into equation 2.1-5 the resonant frequency of a rectangular cantilever is found to be:

$$f_n = \frac{C_n^2}{2\pi}\sqrt{\frac{k}{3m_0}} = \frac{C_n^2}{4\sqrt{3}\pi}\sqrt{\frac{E}{\rho}}\frac{w}{l^2} \tag{2.1-7}$$

where ρ is the density of the cantilever material. A more detailed description of the calculation of the cantilever's resonant frequency can be found elsewhere [81][15][16].

The minimum detectable mass change of a cantilever based mass sensor is easily deduced by assuming that the mass is evenly distributed on the cantilever and that the spring constant is not effected by the added mass [29][30][31][32]. By differentiating equation 2.1-7 with respect to m, the minimum detectable mass is:

$$\left|\frac{\partial f}{\partial m}\right| = \frac{C_n^2 k^{1/2}}{4\pi\sqrt{2}m^{3/2}} = \frac{1}{2}\frac{f}{m} \tag{2.1-8}$$

$$\Longrightarrow \left|\frac{\Delta m}{m}\right| = 2\frac{\Delta f}{f} \tag{2.1-9}$$

It is seen in this equation that to decrease Δm the resonant frequency of the

cantilever must be high compared to the mass of the cantilever. This means that the minimum detectable mass change can be decreased by scaling down the cantilever's dimensions.

In table 2.1 three values of minimal detectable mass change per frequency are given for different cantilever dimensions. It is obvious from the table that the mass change sensitivity is increased by miniaturizing the sensor. Commercially available cantilevers have a mass sensitivity in the pg range while the NANOMASS final goal cantilever, with a width of 100nm, has a mass sensitivity of 10^{-19}g/Hz, which is the size of single large molecules or proteins.

width	height	length	f_0	$\frac{\Delta m}{\Delta f}$
2000nm	50μm	262μm	41kHz	$3.0{\cdot}10^{-12}$g/Hz
500nm	2μm	22μm	1.4MHz	$7.4{\cdot}10^{-17}$g/Hz
100nm	1μm	3.6μm	11.2MHz	$1.5{\cdot}10^{-19}$g/Hz

Table 2.1: The theoretical resonant frequency and mass resolution for three cantilevers with different dimensions. The length is calculated so that the spring constant is 1N/m.

2.2 SPICE Model

SPICE is a simulation tool for simulating electrical circuits. The circuits are built up in a visual environment, which makes SPICE a fast and easy way to simulate and interact with the device. The electrical characteristics of a cantilever based capacitive excitation/readout system has previously been modelled by a LRC equivalent circuit [82][83][84]. This simple small signal equivalent circuit is able to model the current through the system and thus model the frequency response of the cantilever at its resonance. The shortcoming of this model is that it does not take into account spring softening effect, which occur when electrostatic forces are acting on the cantilever. Furthermore, this model only works in the linear regime and often the operation mode of such systems is in the non-linear regime. Finally, only the electrical aspects of the device are modelled, but often the mechanical aspects are just as important in order to simulate mechanical stability and robustness.

In the model presented below a large signal model is developed and implemented into SPICE, where both the electrical and mechanical characteristics of the system will be addressed. The attractive features of this model are that it will be able to calculate spring softening effects of the cantilever, snap-in voltage and the non-linear effects of the dynamic frequency response as well as the electrical behavior of the device.

2.2.1 Large signal model

In order to avoid losing any higher order effects, a large signal model needs to be developed. The mass detector system is based on electrostatic excitation of a cantilever into resonance and capacitive readout to detect the cantilever's change in vibrational amplitude. In order to calculate the actuation and detection properties an analysis of the capacitive system is needed. Figure 2.3 shows a cantilever and two electrode capacitive system, where the charge on the two electrodes is designated by q_n and the gap between electrode one and electrode two and the cantilever is designated as d_1 and d_2 respectively. In this model the cantilever bending is approximated by a stiff plate displacement where the cantilever is not rigidly clamped at one end, but the whole plate is moving. The consequences of this approximation will be addressed in section 2.6

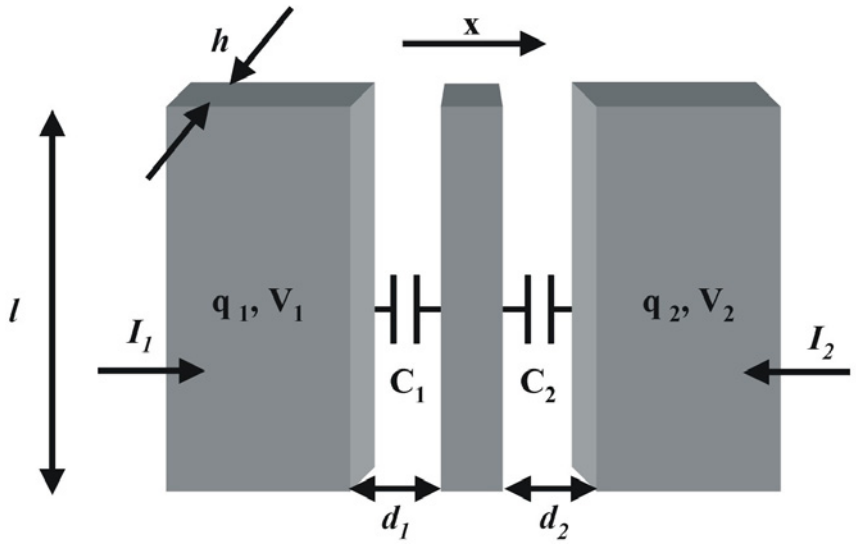

Figure 2.3: Diagram of the simplified device system where the cantilever bending is approximated by a plate displacement.

The potential energy U of the system is:

$$U = \frac{1}{2}kx^2 + \frac{q_1^2}{2C_1} + \frac{q_2^2}{2C_2} \tag{2.2-1}$$

where x is the position, k is the spring constant of the cantilever and C_n is the capacitance between the cantilever and the electrodes. The first term of equation 2.2-1 is the potential energy of the cantilever spring and last two terms describe the total electrostatic energy. The equation of motion is then:

$$m\ddot{x} = \frac{\partial p}{\partial t} = -\nabla U - D\dot{x} \tag{2.2-2}$$

$$= -kx - D\dot{x} - \frac{q_1^2}{2C_1^2}\frac{\partial C_1}{\partial x} + \frac{q_2^2}{2C_2^2}\frac{\partial C_2}{\partial x} \tag{2.2-3}$$

where m is the mass and D is the loss rate. If we rearrange this equation and also insert the potential difference between the electrodes and the cantilever:

$$V_n = \frac{q_n}{C_n} \tag{2.2-4}$$

then we get:

$$m\ddot{x} + D\dot{x} + kx = \frac{q_1^2}{2C_1^2}\frac{\partial C_1}{\partial x} - \frac{q_2^2}{2C_2^2}\frac{\partial C_2}{\partial x} \tag{2.2-5}$$

$$= \frac{1}{2}V_1^2\frac{\partial C_1}{\partial x} - \frac{1}{2}V_2^2\frac{\partial C_2}{\partial x}. \tag{2.2-6}$$

The capacitances can be approximated as the parallel plate capacitance between the electrodes and cantilever:

$$C_1 = \frac{\epsilon A_1}{d_1 + x} \Rightarrow \frac{\partial C_1}{\partial x} = -\frac{C_1}{d_1 + x} \tag{2.2-7}$$

$$C_2 = \frac{\epsilon A_2}{d_2 - x} \Rightarrow \frac{\partial C_2}{\partial x} = \frac{C_2}{d_2 - x} \tag{2.2-8}$$

Then, by inserting equations 2.2-7 and 2.2-8 into 2.2-5:

$$m\ddot{x} + D\dot{x} + kx = -\frac{V_1^2 C_1}{2(d_1 + x)} + \frac{V_2^2 C_2}{2(d_2 - x)} \tag{2.2-9}$$

where the right-hand side terms are the forces from the capacitors. The currents in this system are calculated from the conservation of charge:

$$I_n = \frac{dq_n}{dt} = C_n\dot{V}_n + V_n\frac{\partial C_n}{\partial x}\dot{x} \tag{2.2-10}$$

where the first term is the current from the static capacitance of the system, which is the normal capacitive current, and the second term is the current arising from the mechanical motion of the cantilever. By inserting equations 2.2-7 and 2.2-8 into 2.2-10, the currents flowing into electrode 1 and 2 can be calculated as:

$$I_1 = \frac{dq_1}{dt} = C_1\dot{V}_1 - V_1\frac{C_1}{d_1 + x}\dot{x} \tag{2.2-11}$$

$$I_2 = \frac{dq_2}{dt} = C_2\dot{V}_2 + V_2\frac{C_2}{d_2 - x}\dot{x} \tag{2.2-12}$$

The first version of the equivalent non-linear electrical network diagram of the large signal model is shown in figure 2.4. In order for this model to simulate both the electrical and mechanical properties of the system the non-linear electrical network is divided into the electrical domain and the mechanical domain as designated in figure 2.4. In order to model the mechanical aspects of the device, equation 2.2-9 must be implemented into the circuit. The right hand side of this equation is the mechanical impedance of the cantilever and the left hand side terms are the two non-linear voltage controlled force sources. The voltage controlled force sources are shown in figure 2.4. The velocity in the mechanical domain is then feed back to the electrical domain through two non-linear velocity controlled current sources, also seen in figure 2.4. Equations 2.2-11 and 2.2-12 are used for the velocity controlled current sources.

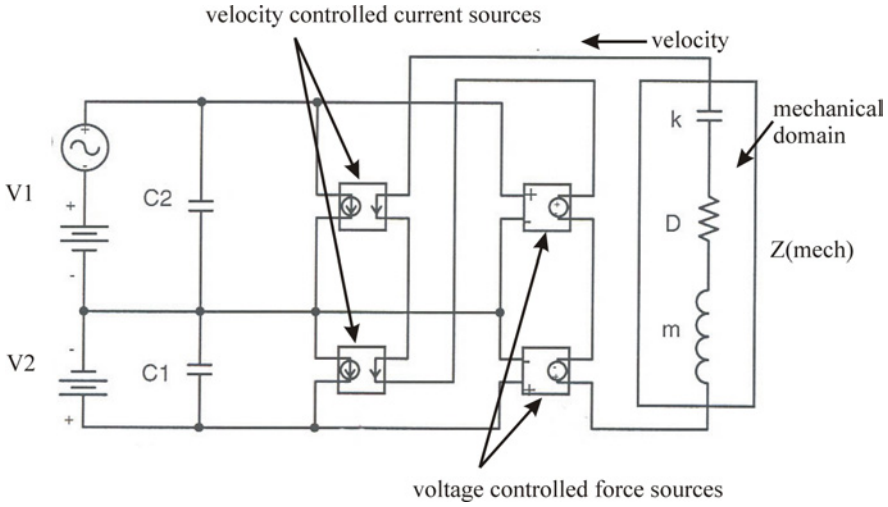

Figure 2.4: Schematic diagram of the equivalent non-linear electric network.

The mechanical impedance of the cantilever is given by:

$$Z_m = sm + D + \frac{k}{s} \tag{2.2-13}$$

where s is the complex angular frequency. In the equivalent circuit the velocity $v(t)$ of the cantilever corresponds to a current and the force F corresponds to a voltage. The equivalent electrical impedance of the cantilever thus becomes:

$$Z_e = sL + R + \frac{1}{sC} \tag{2.2-14}$$

where L is an inductance, R is a resistance and C is a capacitance. By implementing this equivalent circuit into the simulation program SPICE it is possible to simulate both the electrical and mechanical behavior of an electrostatically driven cantilever between two parallel electrodes.

2.2.2 Symmetric cantilever

In order to simplify the model a symmetric device will be considered, where the two electrodes are the same size and at equal distance to the cantilever. That is $d = d_1 = d_2$ and $A = A_1 = A_2$. Furthermore, $A = lh$, where l and h are the length and height of the cantilever. In this symmetric case the capacitances in the system are:

$$C_1 = \frac{\epsilon A}{d + x} = C_0 \frac{1}{1 + \frac{x}{d}} \tag{2.2-15}$$

$$C_2 = \frac{\epsilon A}{d - x} = C_0 \frac{1}{1 - \frac{x}{d}} \tag{2.2-16}$$

where

$$C_0 = \frac{\epsilon A}{d} \tag{2.2-17}$$

Then, the current flowing into electrode 1 and 2 are obtained by inserting 2.2-15 and 2.2-16 into equations 2.2-11 and 2.2-12:

$$I_1 = \frac{dq_1}{dt} = C_0 \frac{\dot{V}_1}{1 + \frac{x}{d}} - \frac{C_0 V_1}{d} \frac{\dot{x}}{(1 + \frac{x}{d})^2} \tag{2.2-18}$$

$$I_2 = \frac{dq_2}{dt} = C_0 \frac{\dot{V}_2}{1 - \frac{x}{d}} + \frac{C_0 V_2}{d} \frac{\dot{x}}{(1 - \frac{x}{d})^2} \tag{2.2-19}$$

In order to implement the mechanical properties into SPICE, a transformation scale factor is needed. By looking at figure 2.4, a transformation is needed between the force and the voltage, the velocity and the current and the mechanical impedance to the electrical impedance:

$$F \longleftrightarrow V_F, v \longleftrightarrow I_v \text{ and } Z_m \longleftrightarrow Z_e \tag{2.2-20}$$

where V_F is the force voltage and I_v is the velocity current. The transformation scaling factor (T) is defined as:

$$T = \frac{C_0}{d} V_R, \text{ unit [C/m] or [N/V]} \tag{2.2-21}$$

where V_R is a fitting constant, which fits the unit and thus has no physical importance. The transformation factor is the link between the electrical and mechanical domain. The mechanical properties of the cantilever system are transformed to:

$$F = T \cdot V_F \tag{2.2-22}$$

$$v = \frac{I_v}{T} \tag{2.2-23}$$

$$Z_m = \frac{F}{v} = \frac{T \cdot V_F}{\frac{I_v}{T}} = T^2 \cdot Z_e \tag{2.2-24}$$

Furthermore, the normalized position $\frac{x}{d}$ can be written as:

$$\frac{x}{d} = \frac{1}{d} \int_0^t v dt = \frac{1}{Td} \int_0^t I_v dt \tag{2.2-25}$$

By inserting equations 2.2-23 into equations 2.2-18 and 2.2-19, the new current equations are:

$$I_1 = C_0 \frac{\dot{V_1}}{1 + \frac{x}{d}} - \frac{V_1 I_v}{V_R (1 + \frac{x}{d})^2} \tag{2.2-26}$$

$$I_2 = C_0 \frac{\dot{V_2}}{1 - \frac{x}{d}} + \frac{V_2 I_v}{V_R (1 - \frac{x}{d})^2} \tag{2.2-27}$$

Finally, the equation of motion can be rewritten by inserting equations 2.2-22 and 2.2-23 into 2.2-9

$$m\ddot{x} + D\dot{x} + kx = m\dot{v} + Dv + k \int_0^t v dt \Leftrightarrow \tag{2.2-28}$$

$$\frac{m}{T} \dot{I}_v + \frac{D}{T} I_v + \frac{k}{T} \int_0^t I_v dt = -\frac{T V_1^2}{2 V_R (1 + \frac{x}{d})^2} + \frac{T V_2^2}{2 V_R (1 - \frac{x}{d})^2} \Leftrightarrow \tag{2.2-29}$$

$$\frac{m}{T^2} \dot{I}_v + \frac{D}{T^2} I_v + \frac{k}{T^2} \int_0^t I_v dt = -\frac{V_1^2}{2 V_R (1 + \frac{x}{d})^2} + \frac{V_2^2}{2 V_R (1 - \frac{x}{d})^2} \Leftrightarrow \tag{2.2-30}$$

$$L\dot{I}_v + R I_v + \frac{1}{C} \int_0^t I_v dt = -\frac{V_1^2}{2 V_R (1 + \frac{x}{d})^2} + \frac{V_2^2}{2 V_R (1 - \frac{x}{d})^2} \tag{2.2-31}$$

Now we have all the equations needed in order to implement the system into SPICE. Since V_R is just a fitting constant, which does not have any physical meaning, it will make the calculations more straight forward by setting $V_R = 1V$.

2.2.3 SPICE implementation

As seen in figure 2.4 the two non-linear voltage controlled force sources transforms the applied voltages into forces, which act on the cantilever. The two non-linear velocity controlled current sources transforms the physical attributes of the cantilever into currents. The right side of equation 2.2-31 is used for the two non-linear voltage controlled force sources for the first and second electrode respectively. Equations 2.2-26 2.2-27 are used for the velocity controlled current sources, where the current velocity, I_v, is feed back along with the cantilever's normalized position, equation 2.2-25. The final SPICE circuit diagram can be seen in figure 2.5. The shaded areas show where the voltage controlled force sources and the velocity controlled current sources are placed. The individual boxes are used to implement the motion and current equations into SPICE. Furthermore, the mechanical equivalent circuit is represented by the LCR branch. The values of L, C and R can be deduced from equations 2.2-30 and 2.2-31 and are given by:

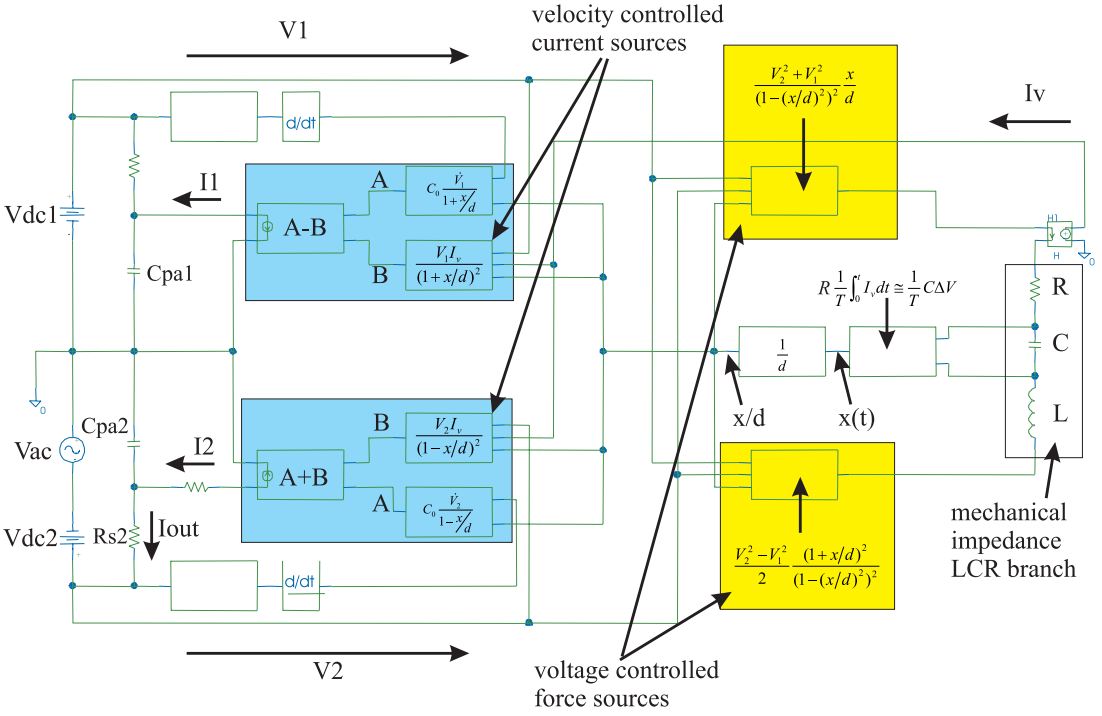

Figure 2.5: The final SPICE circuit diagram of the cantilever based capacitive system where both the electrical and mechanical properties can be simulated simultaneously.

$$L = \frac{m_{eff}}{T^2} \tag{2.2-32}$$

$$C = \frac{T^2}{k} \tag{2.2-33}$$

$$R = \frac{D}{T^2} = \frac{\omega_n m_{eff}}{QT^2} \tag{2.2-34}$$

m_{eff} is again used to compensate for the mass-spring approximation, so the resonant frequency matches that of a cantilever with one end rigidly clamped. The loss rate D is written as a function of the cantilever's angular frequency, the effective mass and the Quality (Q) factor in the following manner:

$$D = \frac{\omega_0 m_{eff}}{Q} \tag{2.2-35}$$

The Q-factor is a measure of the energy lost by the cantilever per cycle [81][85]. A high Q-factor denotes low energy loss, and thus the frequency response of the cantilever will have a large and sharp amplitude. The three main contributions to the Q-factor are acoustic damping Q_a, damping due to imbalances in the cantilever structure Q_s and damping due to internal structure (defects, etc...) Q_i. The total Q factor, is then:

$$\frac{1}{Q} = \frac{1}{Q_a} + \frac{1}{Q_s} + \frac{1}{Q_i} \tag{2.2-36}$$

The resonant frequency of the LCR branch is calculated to:

$$f_n = \frac{1}{2\pi}\sqrt{LC} = \frac{1}{2\pi}\sqrt{\frac{k}{m_{eff}}} = \frac{C_n^2}{4\sqrt{3}\pi}\sqrt{\frac{E}{\rho}}\frac{w}{l^2} \tag{2.2-37}$$

which is exactly the result found from equation 2.1-7. That is, this resonant frequency is the frequency of the cantilever without any external or damping forces acting on it.

The velocity current I_v and the cantilever deflection $x(t)$ are accessed as shown in the circuit diagram. The currents, which flow into electrodes 1 and 2, are shown as I_1 and I_2 respectively. The output current, which contains the device current plus a capacitive current through the parallel parasitic capacitance, $Cpa2$, is denoted as I_{tot}. The voltages of the system are controlled by the two DC and one AC voltage sources. The model can simulate both one and two electrode devices, by using AC and DC2 or by using AC and both DC1 and DC2, dividing the voltage between the two sources.

As mentioned earlier, the two non linear voltage controlled force sources are taken from equation 2.2-31. When performing an AC analysis simulation, which simulates the frequency response of the cantilever, the SPICE program only makes a first order linear expansion around the point of operation. This means that some of the effects are lost, because they are higher order effects. In particular

the SPICE model cannot simulate both the static bending the cantilever and the resonant frequency reduction, due to external forces acting on the cantilever, when equation 2.2-31 is used directly. In order to model these effects equation 2.2-31 needs to be rewritten so that the wanted effects are calculated in the first order.

The rewritten equation of motion, which is directly implemented into SPICE is:

$$L\dot{I}_v + RI_v + \frac{1}{C}\int_0^t I_v dt = \frac{V_2^2 - V_1^2}{2V_R}\frac{1+(\frac{x}{d})^2}{(1-(\frac{x}{d})^2)^2} + \frac{V_2^2 + V_1^2}{V_R(1-(\frac{x}{d})^2)^2}\frac{x}{d} \qquad (2.2\text{-}38)$$

Basically, the first term addresses the static bending of the cantilever. If V_1=V_2 this term disappears resulting in no static bending. The second term addresses the effective spring constant softening effect, which is proportional to the sum of the voltages squared.

2.3 Spring softening effects

One of the desired qualities of the model is the ability to model spring softening effects of the cantilever due to the applied electrostatic forces on the cantilever. By looking at the basic equation of motion 2.1-4 this time including electrostatic forces F_{el} and inserting $x(t) = Asin(\omega t+\theta)$ and by inserting the Taylor expanded electrostatic force, the radial frequency can be solved as [81]:

$$\omega = \sqrt{\frac{k - \partial F(0)/\partial x}{m}} = \sqrt{\frac{k-k_{el}}{m}} \qquad (2.3\text{-}1)$$

where k_{el} represents a spring constant softening. By inserting $f = \omega/2\pi$ and the value for the electrostatic forces as seen in equation 2.2-5, the reduced resonant frequency as a function of the applied voltages is approximately:

$$f_r \simeq f_0 - \frac{2C_0 l^3 f_0}{Ew^3 d^2 h}(V_1^2 + V_2^2) \qquad (2.3\text{-}2)$$

During operation of the cantilever both a DC and AC voltage will be applied to the cantilever. In this case the voltage squared would be:

$$
\begin{aligned}
V^2 &= (V_{DC} + V_{AC})^2 && \text{(2.3-3)}\\
&= V_{DC}^2 + 2V_{DC}V_{AC} + V_{AC}^2 && \text{(2.3-4)}\\
&= V_{DC}^2 + 2V_{DC}V_{ac}\sin(\omega t) + V_{ac}^2\sin^2(\omega t) && \text{(2.3-5)}\\
&= V_{DC}^2 + 2V_{DC}V_{ac}\sin(\omega t) + \frac{1}{2}V_{ac}^2 - \frac{1}{2}V_{ac}^2\sin(2\omega t) && \text{(2.3-6)}\\
\langle V^2\rangle &= V_{DC}^2 + \frac{1}{2}V_{ac}^2 && \text{(2.3-7)}
\end{aligned}
$$

where V_{ac} is the amplitude of the AC signal. Only the average value of the voltages has any spring softening effects but equation 2.3-7 shows that not only the DC voltages but also the AC voltage will reduce the effective spring constant of the cantilever. Usually, in the two electrode configuration the DC voltage is applied to the cantilever and the AC voltage is applied to one of the parallel electrodes, see figure 4.1. So the final dependence of the resonant frequency on the applied voltages is:

$$f_r \simeq f_0 - \frac{2C_0 l^3 f_0}{Ew^3 d^2 h}(V_{DC}^2 + \frac{1}{2}V_{ac}^2) \qquad \text{(2.3-8)}$$

This equation shows that the resonant frequency of the cantilever is linearly dependent on the sum of the applied voltages squared. It is worth noting that this equation is only valid in the linear regime where $x << d$. Also the equation is written so that the slope of the dependence is dependent on the static capacitance of the system, equation 2.2-17. This is done because in the next section the validity of that approximation is discussed and the role of fringing fields, which will increase the value of C_0 compared to the parallel plate approximation, is introduced.

2.3.1 Frequency noise

Due to the dependence of the resonant frequency on the applied voltages, any noise from the voltage source will also fluctuate the resonant frequency. The level of frequency fluctuation or noise can be determined by differentiating equation 2.3-2:

$$\frac{\partial f}{\partial V} = \frac{4C_0 l^3 f_0}{Ew^3 d^3 h}V \qquad \text{(2.3-9)}$$

thus the frequency noise as a function of the voltage noise is:

$$\delta f = \frac{4C_0 l^3 f_0 V}{E w^3 d^3 h} \delta V \tag{2.3-10}$$

In table 2.2 the frequency noise due to voltage noise is seen for three device geometries at a applied voltage of 10V. It is seen that when scaling down the device the frequency noise increases. In the last column the maximum voltage source noise, in order to achieve a 1Hz fluctuation, is calculated.

width	length	height	gap	f_0	$\frac{\delta f}{\delta V}$	δV
2000nm	50μm	262μm	5μm	41.3kHz	-384Hz/V	2.6mV
500nm	2μm	22μm	1μm	1.4MHz	-5610Hz/V	178μV
100nm	1μm	3.6μm	0.5μm	11.2MHz	-28272Hz/V	35.4μV

Table 2.2: The frequency noise $\frac{\delta f}{\delta V}$ due to voltage noise for three device dimensions. In the last column the acceptable voltage noise in order to have a 1Hz frequency fluctuation is calculated.

It is seen that the frequency noise increases as the dimensions of the device decrease and that the tolerable voltage noise is on the mV-μV range. Typical voltage sources have voltage noises on the order of 500μV, which is higher than the acceptable noise for the two smallest devices in table 2.2. This means that measures need to be taken in order to minimize the voltage output noise, in order to have a high resolution.

2.4 Fringe effects

In the calculations above the capacitance between the cantilever and parallel electrode was approximated by a parallel plate capacitance between the side wall surfaces. In this approximation the fringing fields are neglected. If the gap size between the cantilever and electrode has the same magnitude as the height of the cantilever and electrode then these fringing field can not be neglected anymore. In order to include these effects in the model the fringing fields can be approximated by increasing the effective height of the parallel plate capacitor, as seen in figure 2.6. The total capacitance between the cantilever and parallel electrode now becomes:

$$C_{tot} = \frac{\epsilon A}{d}(1 + \alpha) \tag{2.4-1}$$

where α is the fringe factor. The fringe factor will depend on the width and height of the cantilever and the cantilever material. Furthermore, the fringe factor is very difficult to calculate analytically, thus this factor remains empirical.

One would expect that as the height increases, compared to the gap distance, the fringing contribution to the total capacitance would decrease.

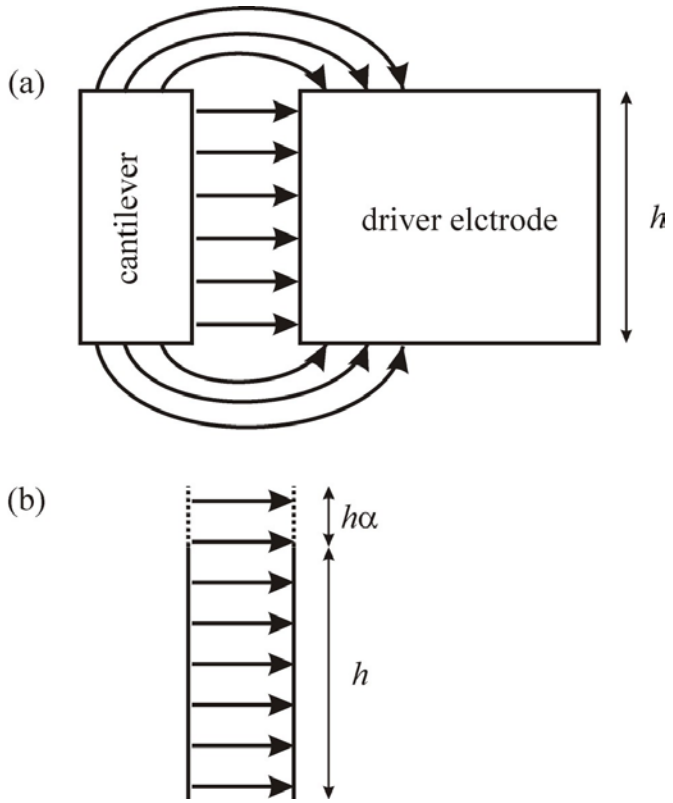

Figure 2.6: In (a) the actual fringing fields are shown at the edges of the cantilever/driver system and in (b) the system is approximated by extending the plate with αh.

In order to implement the fringe effects into the SPICE model, C_0 in equation 2.2-17 is replaced with equation 2.4-1. In figure 2.7 frequency response of a cantilever with width, height, length and gap of 1μm, 0.6μm, 40μm and 1μm is simulated with α values of 0 and 1. The applied voltages are V_{AC}=100mV and V_{DC}=35V. In figure 2.7a the amplitude of the vibration has increased and the resonant frequency has shifted. This is expected because the capacitance of the device is increased, thus the forces acting on the cantilever are also increased, which increases the amplitude and lowers the resonant frequency due to spring softening effects. In figure 2.7b the output current is simulated with a parasitic capacitance of 10fF. Again, both the current amplitude and resonant frequency are changed.

The fringe factor will be estimated through experimental measurements.

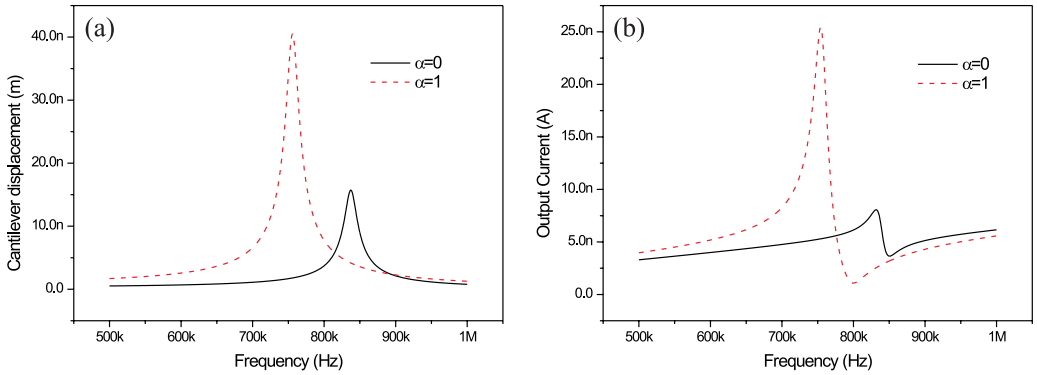

Figure 2.7: Simulated frequency responses of (a) the vibrational amplitude and (b) the output current, using α=0 and α=1.

2.5 Non-linear effects

It has been observed that when the vibrational amplitude of the cantilever approaches the gap distance between the cantilever and electrode, the cantilever shows non-linear behavior [86][87]. As stated one of the objectives of the SPICE model was to be able to simulate the non-linearities. This is possible by performing a transient analysis and measuring the oscillation amplitude of the cantilever at different AC frequencies. Figure 2.8 shows the simulated frequency response of the cantilever's oscillation amplitude in the non-linear regime. In this simulation the cantilever dimensions were 1μm, 0.6μm, 40μm and 1μm for the width, height, length and gap distance respectively. The applied voltages were 100mV AC and 22V DC. It can be seen that the frequency response of the cantilever is not symmetrical. As the frequency increases the amplitude increases very dramatically and then falls again at a slower rate.

2.6 SUGAR model

The main weakness of the SPICE model is that it is based on the stiff plate approximation, thus the true bending of the cantilever is not correct. This means that the SPICE model can be used for simulating the values of the snap-in voltage, the resonant frequency reduction due to spring softening effects and the electrical behavior, but not the true cantilever deflection. Furthermore, in order to successfully model the mechanical behavior, the displacement $x(t)$ needs to be reduced be a certain effective value. In order to determine this value a simple finite element (FE) model has been used, which can simulate the static behavior of the cantilever/electrode system.

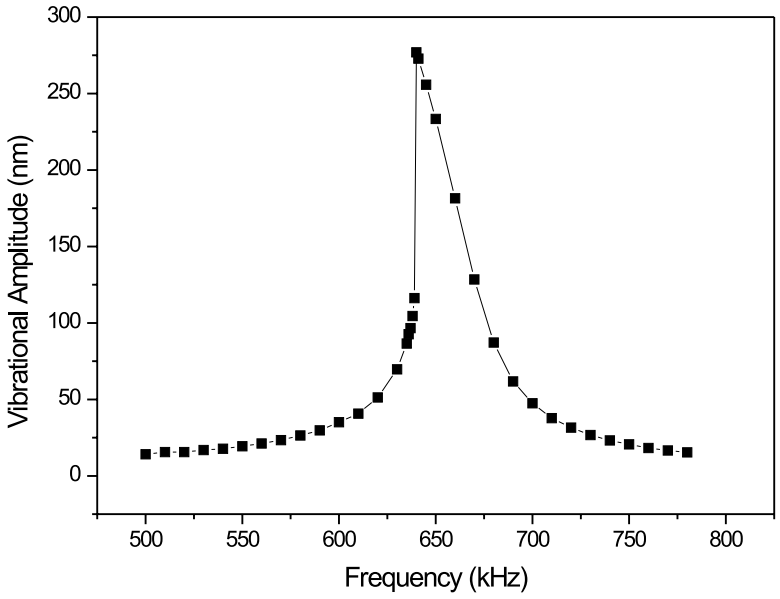

Figure 2.8: The simulated frequency response illustrating the non-linear effects due to large vibrational amplitudes.

The 2D FE modelling has been performed with SUGAR, whose main components are *netlist* interpreter models written in MATLAB or C, describing the characteristics of different components. With a command line and GUI (graphical user interface), SUGAR allows visualization and interaction of the device.

In this model the objective is to model the cantilever bending when a DC voltage is applied between it and a parallel electrode. First, the device is built up, where the material properties and the actual dimensions of the device are built up in a *netlist* input file. The actual *netlist* files can be seen in Appendix B. When the device is built up a static analysis is performed on the device. In the static analysis the equilibrium state of the device is found. Then the device is displayed. The final program written in MATLAB can also be found in Appendix B. The variable parameters are the cantilever dimensions, the gap distance between the cantilever and electrode and the fringe factor.

2.6.1 Snap-in voltage simulations

In figure 2.9a a device consisting of a 40μm long, 1μm wide and 2μm high device is shown separated 2μm from a parallel electrode. Figure 2.9b shows the result

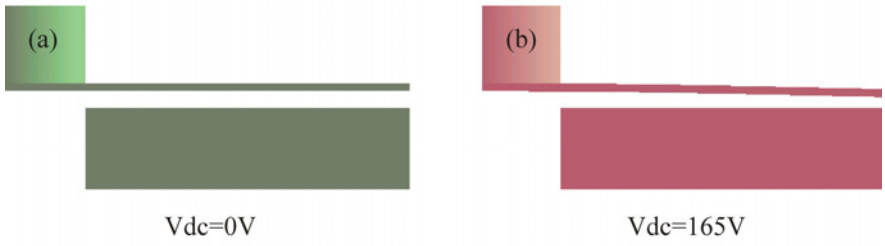

Figure 2.9: Graphical display of the SUGAR model device with (a) no electrostatic forces acting on the cantilever and (b) with a DC voltage of 185V applied between the cantilever and electrode.

of a static analysis of the device when a voltage of 165V is applied between the cantilever and static electrode with the same dimensions and a fringing factor of 0. In figure 2.10 the static deflection at the apex of the cantilever is shown as a function of the DC voltage. The snap-in voltage of the device is approximately 176V. In the same figure a SPICE simulation, with the same device dimensions, is performed and the simulation predicts a snap-in voltage of 68.4V, which is much lower than the SUGAR model. A displacement reduction factor R is multiplied to the $x(t)$ seen in the SPICE circuit diagram, figure 2.5. By setting R to 0.1512 the snap-in voltage of the SPICE model now matches that of the SUGAR model. Furthermore, the actual displacement of the cantilever for the SPICE model is lower than the SUGAR model, which is expected, since the SPICE model is built upon the stiff plate approximation.

2.6.2 Fringe factor effects

In the above simulation the fringe factor is zero, but in a real system the fringe factor will probably be around 1. In figure 2.11a the snap-in voltage of the device is calculated for different fringe factors. It is seen that the snap-in voltage decreases dramatically at small values of the fringe factor then at higher fringe factors the dependance is less. This dependence can be deduced from simply equating the electrostatic forces, $F_{el} = \frac{\varepsilon h V^2}{2(d-x)^2}$, to the spring constant force, $F_{sp} = kx$, and solving for the snap-in criteria, which is [88]:

$$\frac{\partial V}{\partial x} = 0 \tag{2.6-1}$$

Solving the equation for x and plugging that back into the equated forces, the snap-in voltage dependence on the capacitance is found to be:

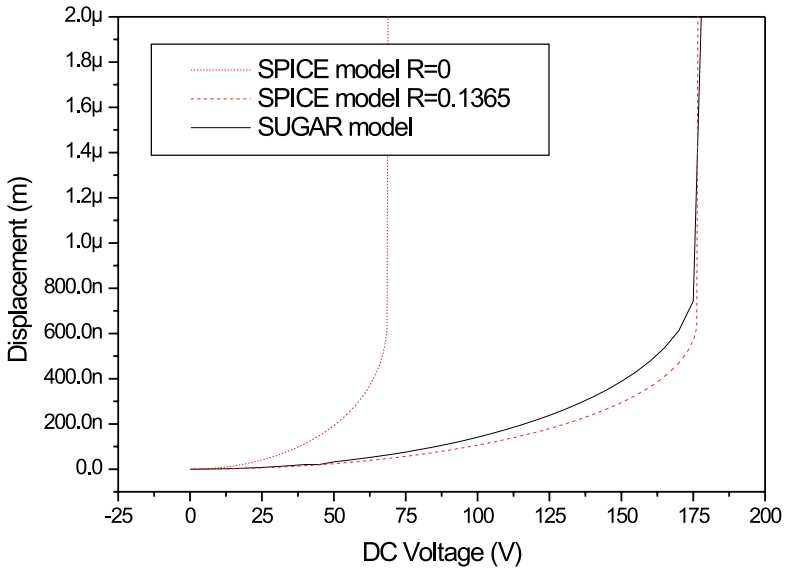

Figure 2.10: Simulation results of the displacement at the cantilever apex performed by the SUGAR model and the SPICE model with R=0 and R=0.1512. The fringe factor is 0 in this simulation.

$$V_s \sim \frac{1}{\sqrt{C}} \sim \frac{1}{\sqrt{\alpha}} \tag{2.6-2}$$

By inverting the squared value of the snap-in voltage and plotting it against the fringe factor a linear dependence is seen, figure 2.11b.

2.7 Summary

In this chapter the general cantilever theory has been presented, which presented the spring constant and dynamic behavior of a rectangular cantilever and ended with a simple calculation of the theoretical mass sensitivity. It was seen that the mass sensitivity increases upon miniaturization of the cantilever and that mass sensitivities on the order of 10^{-19}g/Hz are achievable for cantilevers with widths down to 100nm.

Two models were used to model the mass sensor device. The main model, which is capable of predicting the electrical and mechanical behavior of the capacitive cantilever/electrode system, even in the non-linear case, is the SPICE model. With this model the current output of the device can be simulated with different

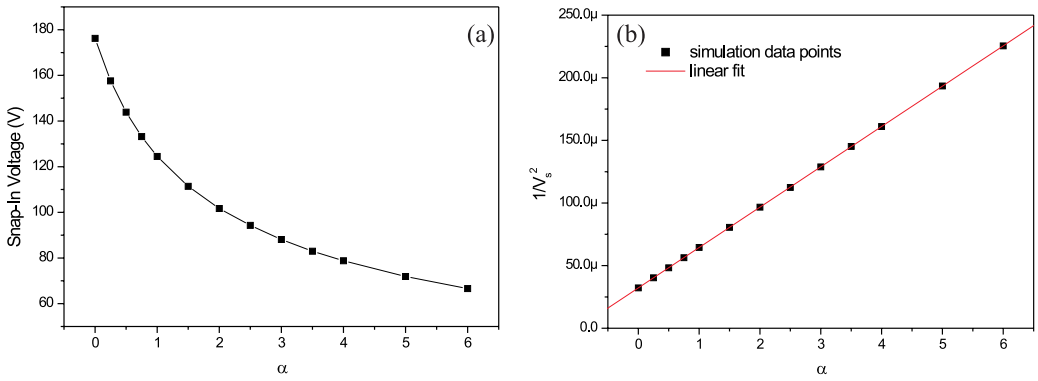

Figure 2.11: The SUGAR simulation of (a) the snap-in voltage as a function of the fringe factor and (b) the inverted snap-in voltage squared as a function of the fringe factor.

cantilever/driver configurations and with different parasitic capacitances. Furthermore, the resonant frequency and the snap-in voltage of the cantilever can be simulated. The fall back of this model is that it is based on stiff components, where the real cantilever bending is approximated by a plate displacement. This means that in order to predict the resonant frequency and the snap-in voltage, a displacement reduction factor must be placed in the model.

In order to calibrate the SPICE model, a 2D FE SUGAR model was used, which is capable of modelling the precise bending of the cantilever. With this model the precise snap-in voltage can be calculated, and by knowing this, the SPICE model can be calibrated to predict the same snap-in voltage with the appropriate displacement reduction factor.

Another important factor that could have a large influence on the performance of the device is the fringe factor. The fringe factor is introduced as a factor that increases the total capacitance of the cantilever/electrode system due to the fringing fields, which at these geometries are probably very dominant. This factor is purely empirical and can only be determined through characterization of the real device.

Chapter 3

Lithography Techniques

In order to achieve the highest sensitivity for a cantilever based sensor, it was seen that the resonant frequency to mass ratio must be as large as possible, see equation 2.1-9. Thus, by decreasing the cantilever dimensions the mass sensitivity increases. The cantilever is fabricated using silicon based processing techniques. The critical fabrication step for defining the cantilever dimensions is the lithography process. Many types of lithography techniques can be used to define silicon based mechanical devices. In this chapter several lithography techniques will be presented, that have been used to fabricate the mass sensor device, namely, UV, laser, atomic force microscopy (AFM) and electron beam lithography (EBL).

In the NANOMASS project, one of the main objectives is to ascertain which lithography technique is best suited for fabricating approximately 100nm wide cantilevers with the best speed and reproducibility. As stated in section 1.4, there are some specific objectives within the NANOMASS project which are treated in this thesis. In this chapter, the main objective is the width of the cantilever based sensor. As seen in section 1.4.2 of the introduction, in work package (WP) 1 the minimum width of the polysilicon based cantilever demonstrator is defined as 0.5μm. In WP 2,4 and 5 the minimum width of the single crystal silicon based cantilever demonstrator is 100nm, which puts large demands on the lithography technique. In WP 3 the minimum width of the metal based cantilevers is 500nm, without CMOS.

3.1 UV lithography

The two basic methods of UV lithography are called contact mask and projection UV lithography. Both setups are shown in figure 3.1. Before UV exposure, a wafer or substrate is coated with a thin layer of photoresist. The polymer based photoresist is dispensed in a liquid phase on the substrate and subsequently spun at a certain rotational velocity until the photoresist is evenly coated on the sub-

strate. Then, the substrate is baked until the photoresist hardens. The thickness of the resist layer is controlled by (1) the viscosity of the resist upon dispensing and (2) the spinning rotational velocity, and can range from below 1μm to several μm.

In contact mask lithography the photolithography mask, which has the desired design, is placed above the substrate and the sandwich structure is irradiated with UV wavelength light, figure 3.1(a). The mask protects the photosensitive resist in certain areas so that the design on the mask can be transferred to the photoresist. After UV exposure of the substrate, either the exposed or unexposed areas can be removed with a chemical etchant, corresponding to a positive or negative photolithography process.

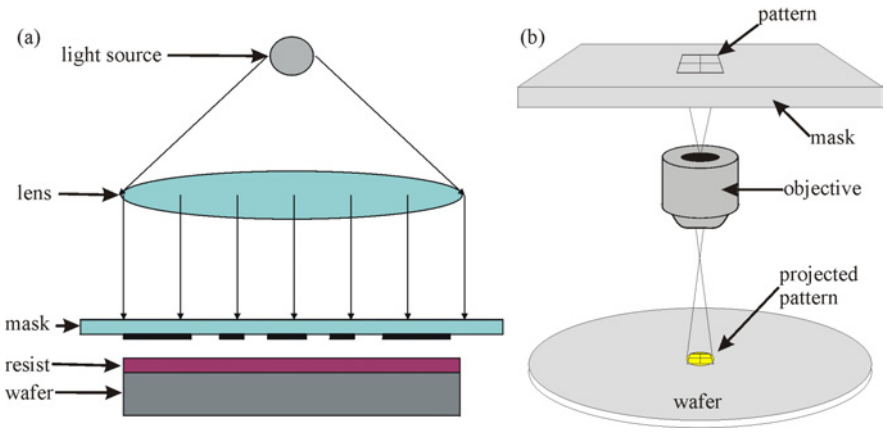

Figure 3.1: Schematic drawing of (a) contact mask and (b) projection mask optical lithography.

The minimum feature size (the minimum width that can be transferred to the photoresist) is given by [79]:

$$s_c = \alpha\sqrt{\lambda \cdot (g + \frac{d}{2})} \tag{3.1-1}$$

where λ is the wavelength of light used to expose, g is the gap between the mask and the resist, d is the thickness of the photoresist and α is an empirical constant on the order of 1, depending on the lithography system. The minimum feature size can be decreased by minimizing λ, the gap g and the resist thickness d. In high resolution systems the gap size is zero, so the UV wavelength and the resist thickness are the two limiting factors. Typically, with a thin resist, line-widths down to a 200-500nm are obtainable, but depend on a very precise and well defined contact mask, which is usually fabricated with electron beam lithography (EBL). Furthermore, the best resolutions depend on the surface being ultra-flat,

with no particles or structures, in order to have a reproducible line-width on the entire wafer.

In projection lithography the mask is separated from the wafer by an objective, which projects the mask design onto the wafer. The advantages of this system compared to the contact mask method is that (1) the mask is not in contact with the wafer, thus there is no risk of damaging the wafer or mask and (2) since the objective can have finite demagnification, the feature sizes on the mask is not critical. Normally, the mask is projected in sections onto the wafer with a stepper technique [53][89]. The minimum feature size of the projection UV lithography is given by [79]:

$$s_p = \beta \frac{\lambda}{NA} \tag{3.1-2}$$

where β is an empirical constant on the order of 1, depending on the illumination system, and NA is the numerical apperature of the magnifying objective. This UV lithography technique is widely used in the IC industry, where feature sizes down to 100-200nm are needed. State of the art microelectronic foundries can have line-widths under 100nm, but more typical values are between 100-500nm. Furthermore, this technique is rarely found in research facilities, with the line-width mentioned above, since the equipment is high maintenance and expensive.

3.2 Laser lithography

The laser lithography process at MIC is a direct writing process. This process has a very high pattern definition flexibility where new patterns can be implemented immediately. However, only one device mask is made at a time, thus this is not a batch process like UV lithography.

The schematic diagram of the direct writing laser facility is shown in figure 3.2. The laser is a continuous-wave argon ion laser with UV option. Beam conditioning and focusing optics, focus the laser beam onto a high-resolution x-y translation stage. The focus point in the z-direction is controlled by an objective, which is mounted on a z-axis stage. The operating laser wavelength for the laser lithography is 488nm, which corresponds to the blue spectrum. There is also an A/O modulator, which serves as an on/off switch for the laser beam. Both x-y and z stages plus the A/O modulator are all controlled via a CPU unit. Through programming software specific patterns can be scanned onto any substrate, which is placed on the x-y stage.

This direct writing laser lithography can be used for prototyping Al coated undoped Si or SiO2, which is a technique developed at MIC by Karen Birkelund

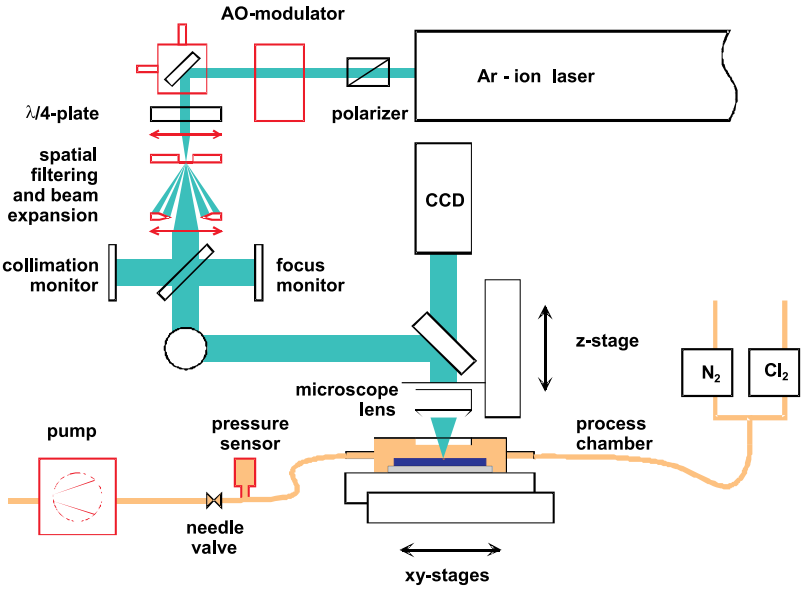

Figure 3.2: The laser lithography setup consisting of an Argon laser, acoustic modulator, optics and a stage, all controlled by a central CPU.

and Anja Boisen[90][91]. In this technique, direct writing on an Al coated Si or SiO_2 surface can be used to define a highly effective dry etching mask, which can be used to selectively etch Si. Another use for the laser lithography system is direct etching of Si surfaces [92][93]. In this process a Si substrate is placed in a chlorine atmosphere and the laser is focussed on the substrate, heating the Si to its melting point, where the chlorine gas reacts with the Si melt, removing it in the gas flow. Finally, the laser lithography facility can also be used to expose photosensitive resist, which is the same process as in UV lithography except that the resist is directly exposed instead of exposed through a mask. The minimum feature size of the laser lithography system is approximately equal to the wavelength of the laser, which is 488nm. Writing speeds are in the range of 0.1-10mm/sec.

3.3 AFM lithography

The third lithography system presented here is atomic force microscopy (AFM) lithography. AFM is based on scanning the surface with a stylus-based microscope technique as seen in figure 3.3. A microcantilever with an integrated tip at the end is raster scanned across the surface. The bending of the cantilever, due to the interaction forces between the tip and sample, is measured and a 3D image of the surface topography is obtained.

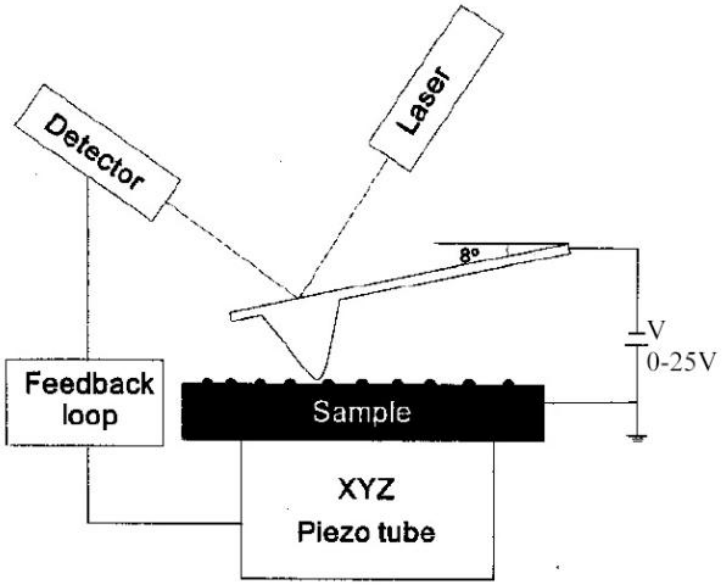

Figure 3.3: The atomic force microscopy lithography setup, where a negative potential is applied between the AFM tip and sample.

Besides imaging of surfaces, AFM has a vast number of other applications, such as manipulation of particles on a surface[94], evaluation of the mechanical or chemical properties of a surface [95], or altering the surface altogether. AFM lithography in this thesis will be defined as local oxidation of a surface by applying a negative potential between the tip and surface as seen in figure 3.3.

Several articles have investigated AFM lithography [96][97][98] and it seems that it is possible to perform highly reproducible local oxidations on silicon, titanium and even aluminum surfaces. The minimum line-width of AFM lithography is directly related to the AFM tip sharpness. It has been demonstrated that 10nm lines on Si surfaces can be produced [99]. The writing speed of this technique is approximately 10μm/sec. Furthermore, jumping and non-contact mode AFM has also been used in AFM lithography, in order to decrease the tip wear and thus increase the writing reproducibility and flexibility.

3.4 E-beam lithography

An electron beam lithography (EBL) setup is shown in figure 3.4 [53][89]. Usually the EBL system is integrated into a scanning electron microscope. The basic

components of the lithography setup are the electron gun, the beam blanker, the deflection coils and the condenser lenses, which focus the e-beam down to 0.01-0.1μm. The electron gun can either be a thermal (TEG) or a field emission gun (FEG). The FEG has a high brightness and a small energy spread and thus has good focussing capabilities even at low acceleration voltages, which is preferred for imaging purposes. Normal e-beam lithography systems use a high acceleration voltage to minimize so called proximity effects due to backscattering electrons. Thus, TEGs are usually used for EBL. The substrate is placed on a high precision stage, which is needed if wanting to expose areas, larger then the electron beam field.

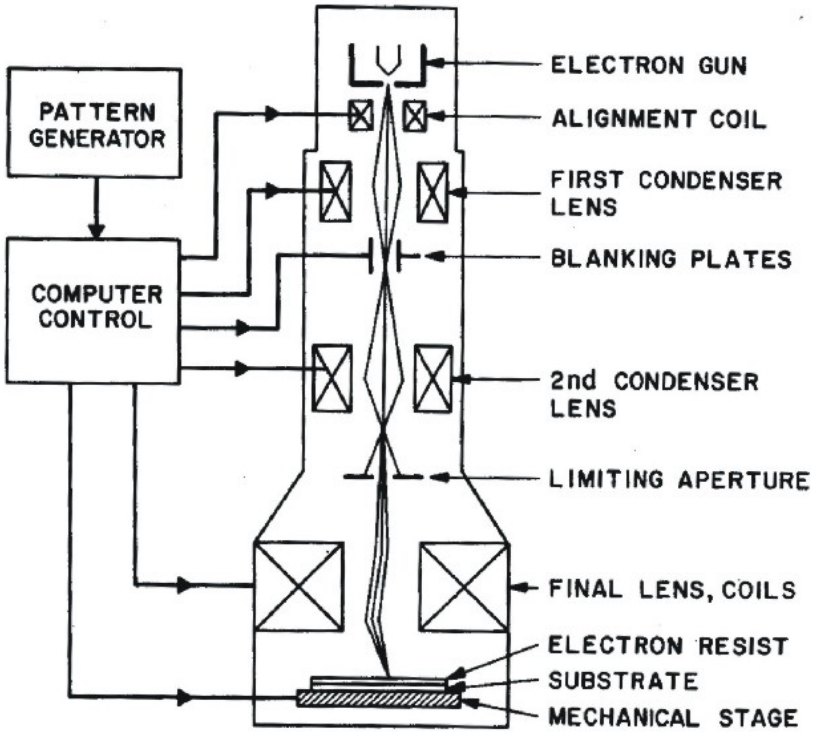

Figure 3.4: A schematic drawing of the EBL setup

The e-beam lithography is a direct writing system where the beam blanker and the deflection coils are used to expose a substrate which has a electron radiation sensitive resist deposited on it. The resist is spun onto the substrate in the same manner as the photoresist mentioned above. A typical e-beam resist is poly(methyl methacrylate) or PMMA, which is spun onto the substrate at a thickness of below 100nm for the best resolution.

There are two methods to expose the substrate; the raster scan and vector scan

method. During raster scan the entire area is scanned, like when doing SEM imaging. The beam blanker is used here to turn on the beam at areas of exposure. During vector scan only the areas to be exposed are scanned. Thus, the e-beam jumps from area to area. If only a small percentage of the total scan area needs to be exposed, the vector scan method is the fastest. Furthermore, variable-beam-shape systems have been developed so that the beam can have different cross section shapes such as rectangles, thereby increasing the writing speed even further. The minimal line-width of EBL is approximately the beam diameter, which can be down to 10nm. Typically, the minimal line-width obtainable is around 50-100nm [80][79]. The writing speed of EBL is typically 100-500μm/sec.

3.5 Summary

In table 3.1 the pros and cons of the techniques presented here are listed. Only UV lithography can achieve batch processing, which ensures the highest throughput. The best UV lithography systems can define features below 100nm, but this limit is practically very difficult to achieve. In order to obtain sub 100nm line-widths, either AFM or E-beam lithography are possibilities. The main differences are that AFM is inherently simple and a cheaper process and that local oxidation can produce line-widths down to 10nm reproducibly. EBL has a higher throughput and can easily achieve the line-widths required for the 100nm wide demonstrator.

technique	line-width	speed	advantages	disadvantages
UV contact mask	300-500nm	batch	cheaper equipment	only flat surfaces high accuracy mask
UV projection mask	sub 100nm	batch	no high accuracy mask structured surfaces ok	high-budget equipment
Laser	500nm	10mm/sec	flexible and fast	reproducibility problems
AFM	10nm	10μm	low minimum line-width low-budget equipment	low throughput
E-beam	sub-50nm	+500μm/sec	high throughput low minimum line-width	high-budget equipment

Table 3.1: A summation of the different lithography techniques discussed in this chapter comparing the minimum line-width and speed and other advantages and disadvantages.

Chapter 4

CMOS Circuitry Design and Fabrication

4.1 General design considerations

In this section the CMOS circuitry design for cantilever based mass detector will be clarified. Previously the general design of the cantilever has been presented as that seen in figure 4.1. Basically, the device consists of a laterally vibrating cantilever separated from one (a) or two (b) parallel electrodes. The cantilever is excited into resonance by applying an AC voltage between the static electrode and the cantilever. The displacement of the cantilever is monitored by the capacitance in the system. In the one electrode system both the AC and DC signal are applied to the electrode and the output current is measured at the cantilever. In the two electrode configuration one electrode is used for driving the cantilever and the other is used for measuring the output current.

4.1.1 Parasitic capacitances

As seen in equation 2.2-10 the current through the system is equal to a regular capacitive current and a mechanical current. In a real system the capacitive current is not just the current through the cantilever electrode capacitance, but also through any parasitic capacitances in the system, C_{pa}, as seen in chapter 2. In the SPICE model the output current, which is the current flowing though Rs2, figure 2.5, can be modelled with different values of parasitic capacitances, which is denoted as Cpa2 in figure 2.5. Figure 4.2 shows SPICE simulations of the output current at three different parasitic capacitances. The physical parameters for this simulation are w=1μm, t=2μm, l=40μm d_0=2μm, Q=50, V_{AC}=1V and V_{DC}=110V. The Q-factor has been chosen based on previous measurements on such cantilevers in air [81][100] where it was found to be 50.
By looking at figure 4.2 it is seen that the vibrational amplitude at the peak is approximately 180nm at a resonance frequency of 706kHz. Since the amplitude

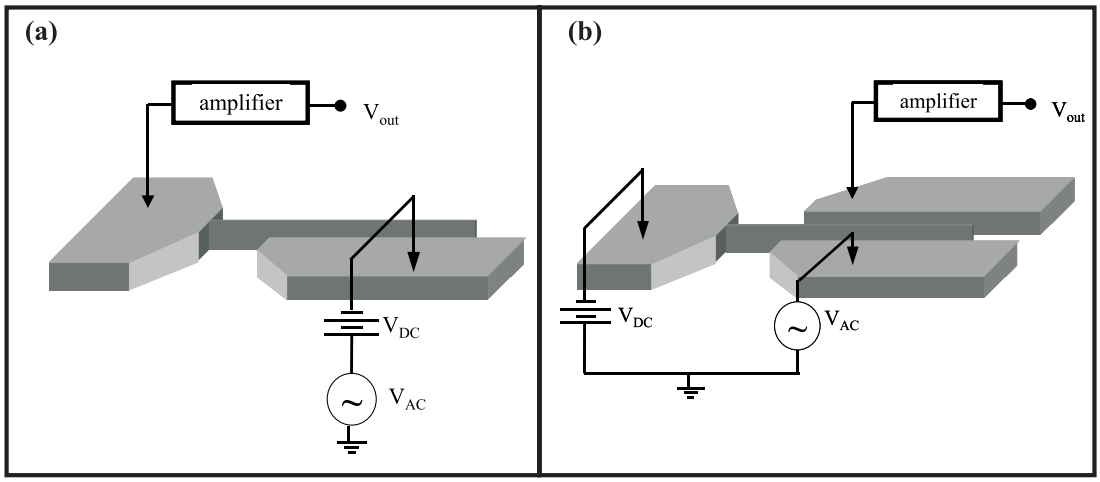

Figure 4.1: Schematic drawing of the (a) one electrode design and (b) two electrode design.

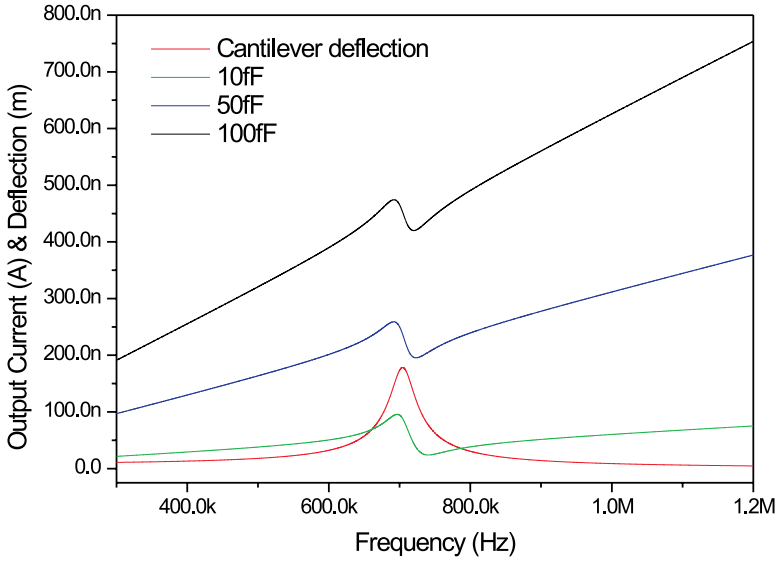

Figure 4.2: SPICE simulations of the vibrational amplitude of the cantilever and the current output with three values of parasitic capacitance, 10fF, 50fF and 100fF.

is below 10% of the gap distance of 2μm, it is assumed that non-linearities do not dominate the system. Along with the vibrational amplitude are three simulations of output current with three different values of parasitic capacitance. It is seen that when increasing the parasitic capacitance the current level is raised. Fur-

thermore, the current seems to be linearly proportional to the frequency around the resonance. This is understood by looking at the first term in equation 2.2-10:

$$I_{cap} \cong (C_{pa} + C_{can})\dot{V}(t) = (C_{pa} + C_{can})\omega V_0 \cos(\omega t) \tag{4.1-1}$$

where $V(t) = V_0 \sin(\omega t)$, C_{can} is the cantilever-electrode capacitance. Furthermore, by increasing the parasitic capacitance C_{pa} the gradient of the linear dependance increases. It is also seen that the current output has a peak and anti-peak current value. This effect is due to an anti-resonance produced by the parallel parasitic capacitance. This anti-resonance approaches the mechanical resonance when the parasitic capacitance increases [101][102]. Thus the mechanical resonance is cancelled out by the anti-resonance at high parasitic capacitances.

In order to see how much parasitic capacitance can be tolerated the SPICE model has been used to calculate the peak to anti-peak current and the peak to anti-peak to peak current ratio $PAPPR$, which is defined as:

$$PAPPR = \frac{I_{peak} - I_{a-peak}}{I_{peak}} \tag{4.1-2}$$

where I_{peak} and I_{a-peak} are the peak current and anti-peak current respectively. The peak to anti-peak current $PAPC$ is a measure of what current resolution is needed to make the measurements. Furthermore, the $PAPPR$ ratio tells us the ratio between what current resolution needed and the current level. The simulation results are shown in figure 4.3.

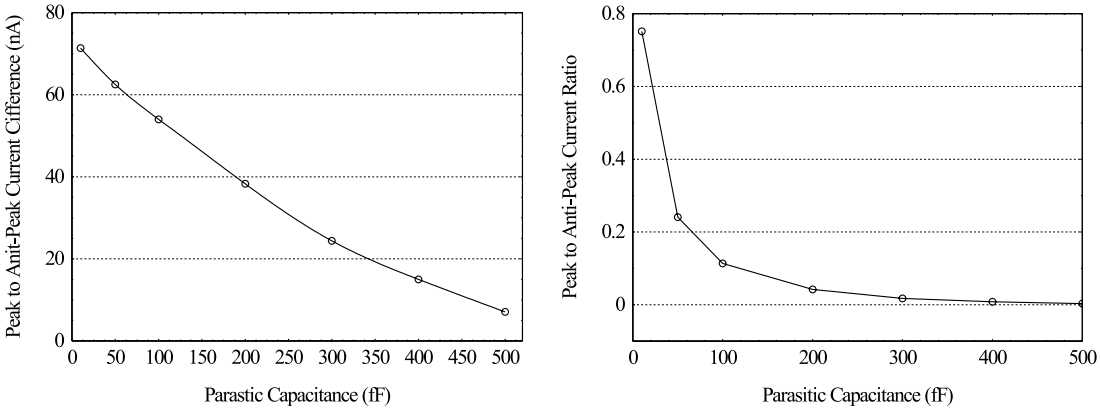

Figure 4.3: SPICE simulation results showing (a) the current peak to anti-peak value and (b) peak to anti-peak to peak current ratio.

By looking at figure 4.3a it is seen that the $PAPC$, as expected, is dropping with the increase in parasitic capacitance. At C_{pa}=500fF the $PAPC$ is approximately

7nA, which is a quite low value, but not impossible with careful readout circuitry design. But, by looking at the $PAPPR$ versus parasitic capacitance a much steeper drop is seen. Already at C_{pa}=100fF the $PAPPR$ is already below 0.1, which means the signal is only 10% of the current level and at 400fF the signal is less than 1%. These results show that the parasitic capacitance should not be more than 300-400fF. Otherwise the mechanical current signal is too low to measure.

4.1.2 One versus two electrode configuration

The mechanical current signal can be increased compared to the parasitic signal by increasing the DC voltage and decreasing the AC voltage. In theory by having a very low AC voltage and high DC voltage the parasitic currents can be lowered substantially. In the one electrode design, the snap-in of the cantilever prevents the increase of the DC voltage beyond a certain value. In figure 4.4a-c the output current for three different values of AC and DC voltage are shown for the same device as above, but with a parasitic capacitance of 500fF. It is shown that by decreasing the AC and maximizing the DC, the PAPPR can be increased to 0.0759, but it is still very low, see figure 4.4. Furthermore, it is seen that by applying high DC voltages the resonant frequency drops considerably, which is unwanted because this decreases the mass resolution. In figure 4.4d the static bending of the cantilever of the one electrode device shows that the DC voltage cannot go beyond 126V DC.

A way to increase the DC without snap-in is to use the two electrode configuration, figure 4.1b. In this configuration, since the electrodes are symmetric a much higher voltage can be applied to the cantilever without snap-in. In figure 4.5 the same device is simulated with the same parasitic capacitance, this time with the two electrode configuration. The AC voltage is held to 0.1V while the DC voltage is increased. Through these simulations it is seen that the cantilever signal is not enhanced as much as the one electrode configuration. The reason for this is because in the one electrode configuration the effective static capacitance C_0 is increased due to the static bending of the cantilever towards the electrode. Since the static cantilever capacitance is proportional to $\frac{1}{d}$, a decrease in the gap leads to a larger increase in mechanical current then the linear dependance of the DC voltage. Another disadvantage is that by applying too high voltages the resonant frequency is decreased, which, again, is undesirable.

In a real system, with an off-chip amplifier, the parasitic capacitances occur through the chip wires, the bonding pads and the external wires. With proper shielding and grounding the parasitic capacitance can be minimized to around 500fF, which is still too high for this capacitive readout based mass detector system. Furthermore, the dimensions here are on the order of microns. With

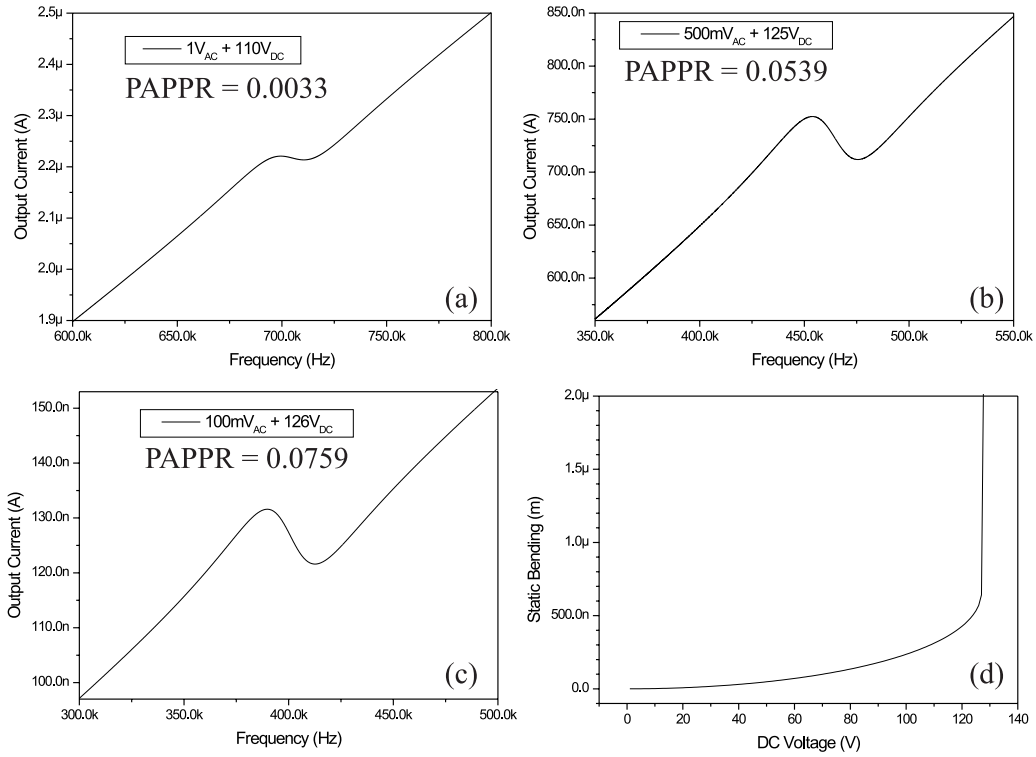

Figure 4.4: SPICE simulations with the 1 electrode configuration showing the current output frequency response for three different voltage configurations, (a) $V = 1V_{AC} + 110V_{DC}$, (b) $V = 500mV_{AC} + 125V_{DC}$ and (c) $V = 100mV_{AC} + 126V_{DC}$. The parasitic capacitance is set to 500fF. (d) the static bending of the cantilever versus the applied DC voltage.

further miniaturization, the cantilever capacitance decreases even further making the mechanical current signal even smaller.

In order to minimize the parasitic capacitance, integration of the mechanical device on the same chip as the amplifier is a distinct possibility. By integrating the mechanical cantilever with standard CMOS circuitry, parasitic capacitance below 10fF can be obtained. Furthermore, integration with CMOS circuitry allows design of tailored circuits, which have the exact characteristics that are needed for the readout system.

4.2 CMOS technology

This section is a description of the CMOS technology, which was utilized for the integration of the cantilever mass detector device. The CMOS fabrication was

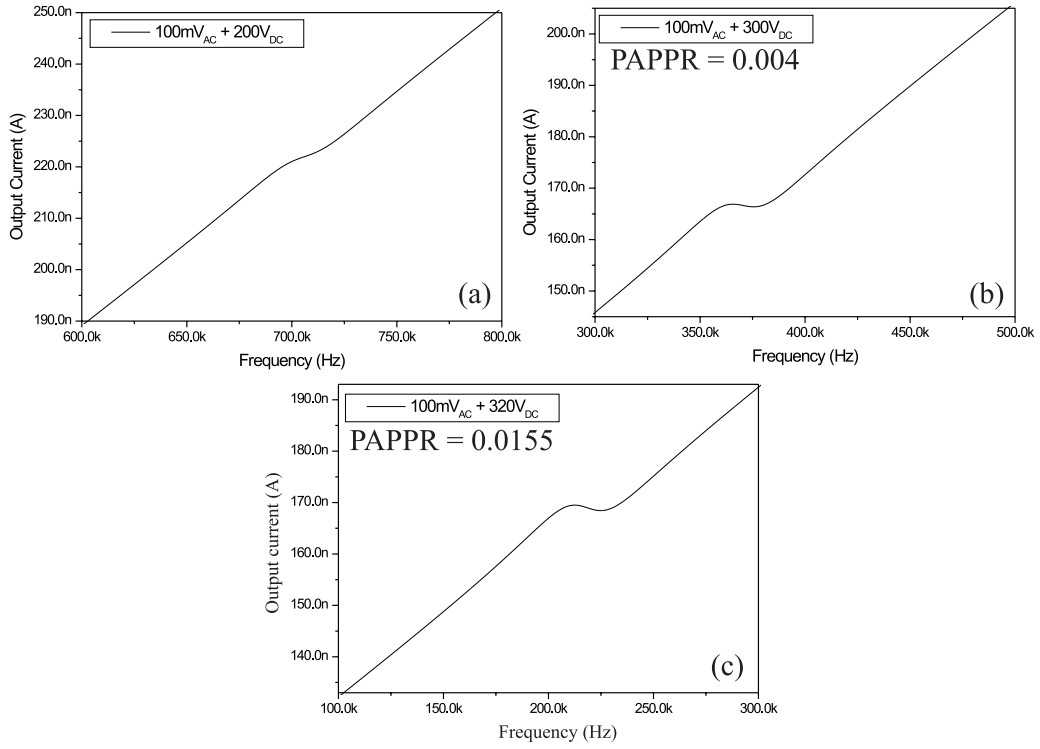

Figure 4.5: SPICE simulations with the 2 electrode configuration showing the current output frequency response for three different voltage configurations, (a) $V = 100mV_{AC} + 200V_{DC}$, (b) $V = 100mV_{AC} + 300V_{DC}$ and (c) $V = 100mV_{AC} + 320V_{DC}$.

performed at Centro Nacional de Microelectrónica (CNM), which is located on the campus of Universitat Autonoma de Barcelona. The standard process is a so-called twin-well, CMOS-2.5μm, 2poly, 1 or 2 metal levels. The process sequence for the standard CMOS fabrication is seen in figure 4.6.

In step (1) the twin N and P wells are defined by photolithography and ion implantation. In step (2) A 1μm thick LOCOS oxide is deposited. Step (3) is the poly0 definition, where an LPCVD poly-silicon is deposited and defined with lithography and wet etching. This poly0 acts as the lower electrode of the capacitors. In Step (4) the poly1 layer is defined. First, a thin gate oxide is grown, which is approximately 365Å thick. Then the poly1 polysilicon layer is deposited by LPCVD and defined using lithography and wet etching. The poly1 acts as the top electrode of the capacitors and the gate electrode. Now, the source and drain are implanted in step (5) using again photolithography and ion implantation. In step (6) a 1.4μm thick BPSG interlevel oxide is deposited and defined using photolithography and wet etching. The interlevel oxide is used for separating the

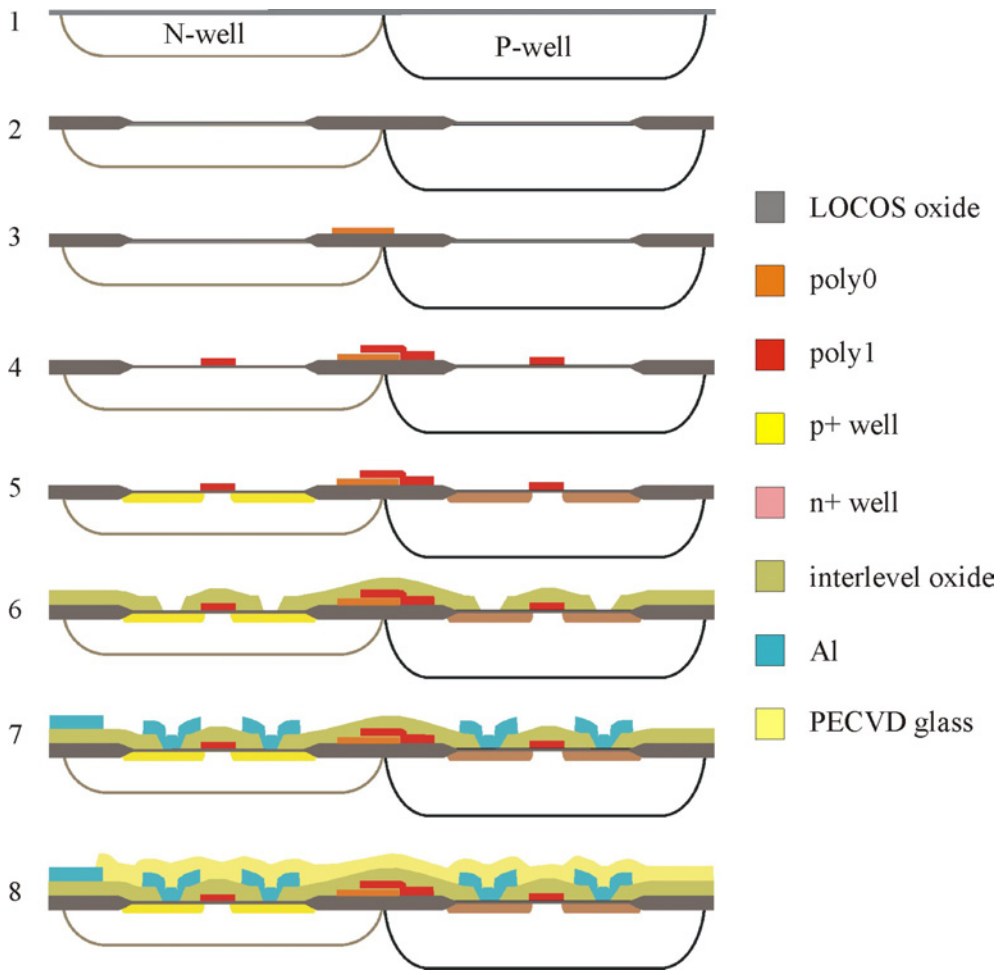

Figure 4.6: Process sequence for the standard 2.5μm CMOS technology. First, the twin wells are defined (1). Then, the thick LOCOS oxide is deposited (2). After that, the first poly0 layer is deposited and defined (3). Then the gate oxide is grown and the top poly1 layer is deposited and defined (4). The source and drain are now defined (5) and the interlevel BPSG oxide is then deposited and defined. Finally, the metal wires and bonding pads are defined (7) and the chips is passivated with a 700nm thick PECVD glass (8).

metal wires from the capacitors and transistors. Next (7), the metal wires and bond pads are defined, by first sputtering a 1μm thick Aluminum layer on the CMOS surface and subsequently patterning it by lithography and wet etching. Finally, in step (8), the whole chip is passivated by depositing a 4000Å thick PECVD oxide and 7000Å thick PECVD nitride. Holes are then opened in the passivation layer in order to access the Al bonding pads.

Previously, silicon based cantilever structures with the capacitive excitation and readout design have been fabricated using a p++ poly-Si/SiO_2/Si sandwich struc-

ture [81][100]. In this structure the top Si layer is used as the device layer where the cantilever and electrodes are defined and the oxide layer acts as a sacrificial layer. The thicknesses were 2μm and 4.5μm for the p++ poly-Si and the SiO_2 layer respectively. In the CMOS process described above a similar sandwich structure is present. The bottom poly0 layer is deposited on top of a 1μm thick oxide layer. This sandwich layer structure is the basis for the first attempts of integration. By using already deposited layers, no add on layers are needed, which simplifies the integration process. Furthermore, electrical connections to the poly0 layer and the transistors are already built into the CMOS fabrication process. The fabrication of the mechanical cantilever is performed as a post processing sequence. In this way all the CMOS processing steps remain standard, which is highly desirable in a CMOS production line.

4.3 Circuit design

In this section the final design of the readout circuit will be presented. However, the details of the circuits will not be discussed here. The main objective of the readout circuitry is to sense the mechanical current produced by the cantilever oscillation and convert this current into a voltage signal, which can be easily measured with an oscilloscope or other voltmeter. Basically, two types of amplification circuits have been designed, which are the amplifier plus voltage follower (BS) and the current amplifier (AC).

4.3.1 BS circuits

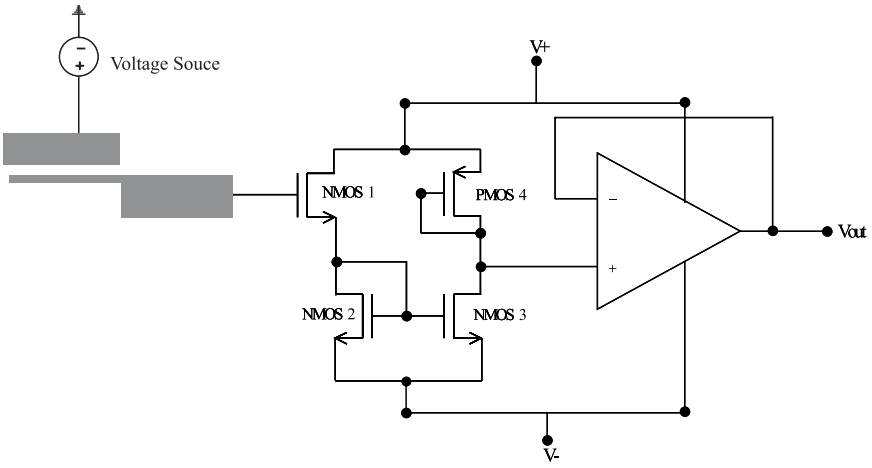

Figure 4.7: Diagram of the BS circuit, which consists of an amplifier and voltage follower.

The simple BS circuit can be seen in figure 4.7. The two main components are the amplifier (source follower) and buffer (voltage follower). The amplifier is a current mirror with three NMOS and one PMOS transistors. Basically, the charge on the cantilever is connected to the gate of the first NMOS transistor. If this transistor is polarized in its linear region, the mechanical current, when the cantilever is in resonance, will fluctuate the gate charge and thus fluctuate the current flowing in the current mirror. The output of the amplifier is connected to an operational amplifier with unity gain, which gives a low impedance at the output of the amplifier.

The gain of the amplifier can be determined from the small-signal model of the transistors. The gain, for a first order model and at low frequencies, is:

$$\frac{V_{out}}{V_{in}} = -\frac{g_{m1}g_{m3}}{(g_{m1}+g_{m2})g_{m4}} \tag{4.3-1}$$

where g_m is the transconductance of the transistors, which depends on the polarization and the dimensions of the transistors according to:

$$g_m = \sqrt{2\mu C_{ox}\frac{W}{L}I_d} \tag{4.3-2}$$

where μ is the mobility of the carriers in the transistors, C_{ox} is the gate capacitance, W and L are the width and length of the gate respectively and I_d is the drain-source current.

The advantage of this type of amplification circuit is that the bandwidth of the operational amplifier remains high since it has a unity gain, thus the bandwidth of the circuit is high.

4.3.2 AC circuits

Two AC amplifiers, denoted AC1 and AC2, are seen in figure 4.8 and are two types of current-voltage converters. The output voltage V_{out} of the AC1 circuit seen in figure 4.8a is:

$$V_{out} = I_{can}(R_1 + R_2)(1 + R_3/R_4) \tag{4.3-3}$$

where I_{can} is the total capacitive and mechanical current through the cantilever/electrode system as defined by equation 2.2-10. Furthermore, the output voltage of the AC2 circuit seen in figure 4.8b is:

$$V_{out} = I_{can}R \tag{4.3-4}$$

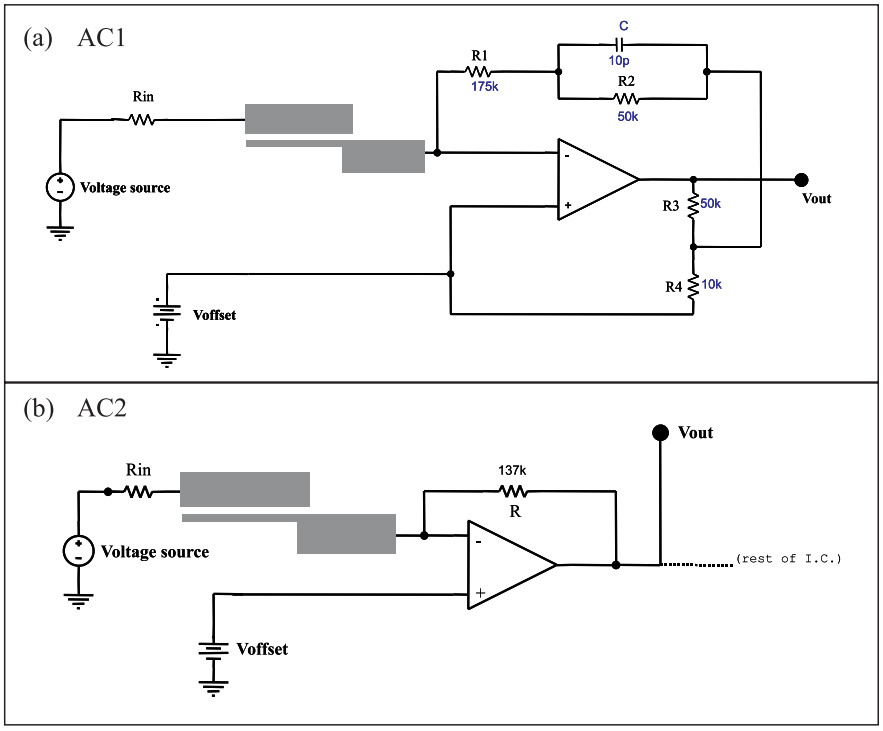

Figure 4.8: Diagram of two types of AC circuits, which are (a) a current-voltage converter and (b) a simple current-voltage converter.

The advantage with the circuit in figure 4.8a is that the same effective transimpedance can be achieved with smaller resistors, which are easier to realize on the CMOS chip.

4.4 1st Generation chip design and layout

Now that the amplification circuits have been described the CMOS chip design and layout will be presented. The 1st generation CMOS chip layout is seen in figure 4.9. The chip layout consists of both BS and AC circuits and several test structures in section A of the chip. The other three sections mainly contain test structures, which are used to evaluate the CMOS parameters during and after post processing of the cantilever device.

4.4.1 BS circuit

In figure 4.10 the 1st generation BS circuit layout is seen. The nanoarea is where the cantilever will be fabricated and consists of the poly0/SiO_2/Si sandwich layer as discussed above. Furthermore, the amplifier and voltage follower are seen. It

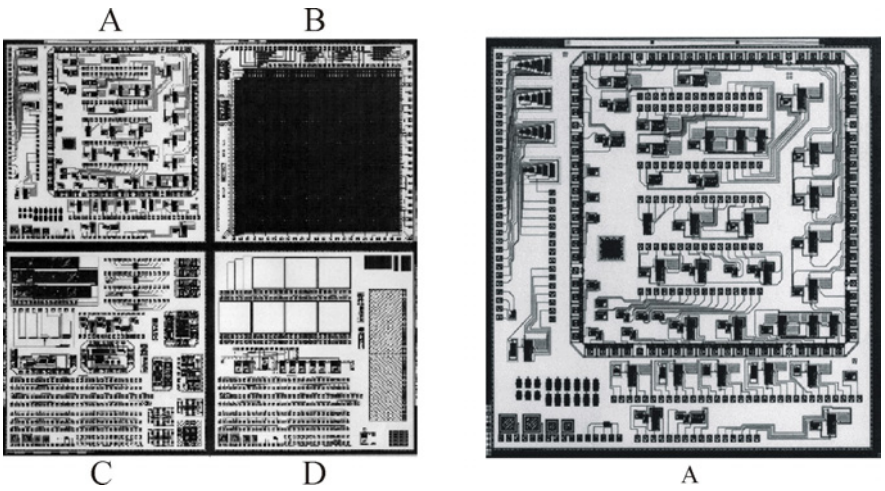

Figure 4.9: Chip layout for the 1st generation CMOS circuitry. The BS and AC circuits are placed in section A.

is worth noting that the underlying Si substrate in the nanoarea is connected to the voltage supply of $V = -2.5V$, which is used to polarize the circuit.

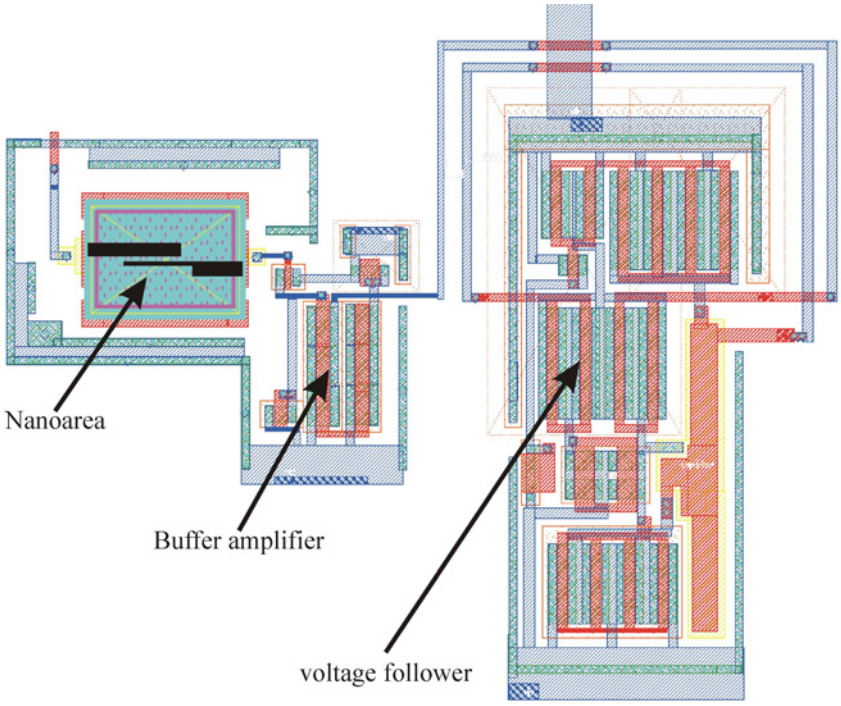

Figure 4.10: Layout of the 1st generation BS circuit. The arrows indicate the nanoarea, the amplifier and the voltage follower.

4.4.2 AC circuit

In figure 4.11 the 1st generation basic AC amplifier layout is seen. Here, the non-inverting input of the operational amplifier is connected to the underlying substrate of the nanoarea, which is grounded during operation. Thus, any parasitic currents through the substrate are short-circuited. Resistor $R1$ is also seen, illustrating how much room is used to make a resistor. The insert in figure 4.11 is an alternative nanoarea, where it is possible to fabricate a two electrode device.

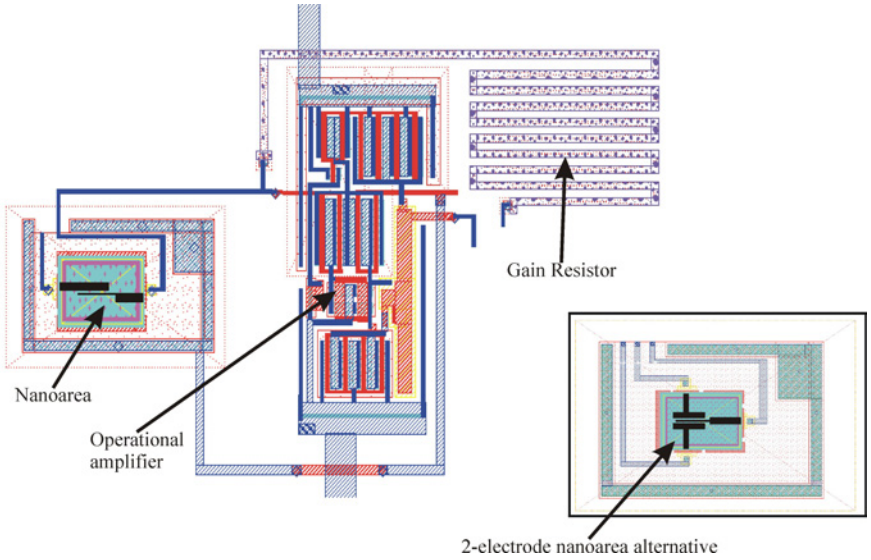

Figure 4.11: Layout of the 1st generation AC circuit. The insert shows the 2-electrode layout of the nanoarea.

4.4.3 1st generation problems

There were two major problems with the 1st generation CMOS chips. The first problem was with the BS circuits, where the underlying substrate in the nanoarea is connected to the -2.5V voltage supply. It was found that the cantilever had a tendency to stick to the bottom substrate during operation. The reason is that in order for the amplifier to work with the maximum gain the cantilever needs to be charged at a certain value. This means that a potential of around 10-15V DC is needed at the voltage input, thus the cantilever has an electrostatic attraction to the bottom substrate, which is -2.5V, and the cantilever collapses to the substrate.

The second problem was that the operational amplifiers had a tendency of resonating in the frequency range of the calculated cantilever resonance.

4.5 2nd generation chip design and layout

In the second generation, some simple design changes where made in order to avoid the problems encountered with the 1st generation. Furthermore, the layout of the chip was changed so that the devices can be more easily accessed with a probecard and still be observed with an optical microscope. The chip layout is seen in figure 4.12. It is seen that the chip is composed of two areas called the B and A, which correspond to the left and right side of the chip respectively. The B section is dedicated to BS circuits and the A side is dedicated to AC circuits.

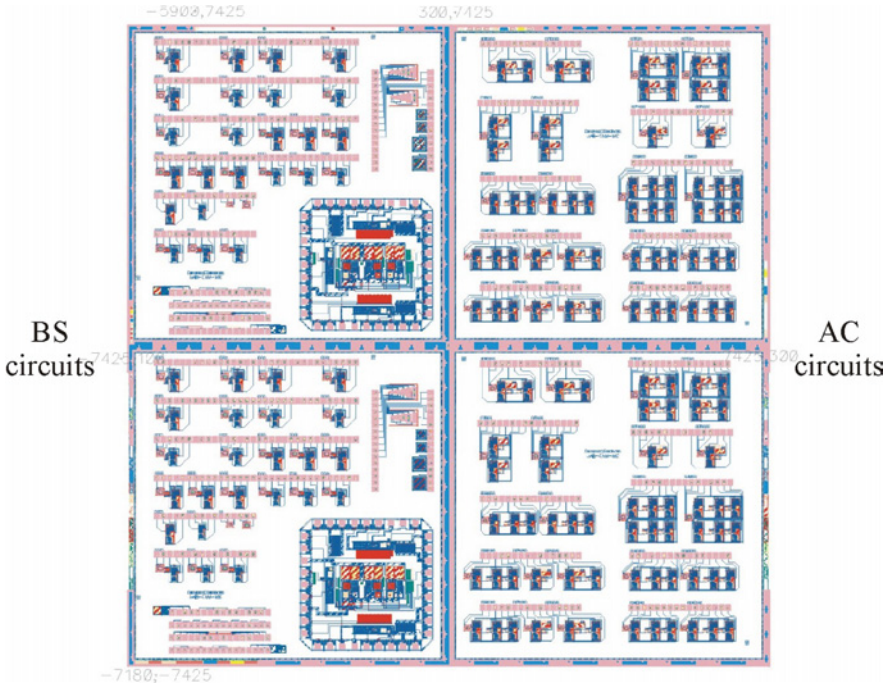

Figure 4.12: Layout of the 2nd generation CMOS circuitry where the left two sections consists of BS circuits and the right two sections consists of AC circuits.

4.5.1 BS circuit

The BS circuits were redesigned in order to solve two problems, which were (1) the underlying substrate is not connected to the -2.5V power supply, but can be accessed from a bonding pad and (2) an extra connection to the nanoarea is added so that the polarization of the amplifier transistor can be done separately from the input voltage. The layout of the new BS circuit can be seen in figure 4.13. Furthermore, the new cantilever design, which consists of the second input electrode connected to a comb capacitor, is also shown in figure 4.13b. The idea of the comb capacitor is that the charge on the cantilever is proportional to the

voltage and the capacitance, see equation 2.2-4. Thus the potential required to polarize the first transistor is reduced because the comb capacitor is larger than the capacitance between the cantilever and driver electrode.

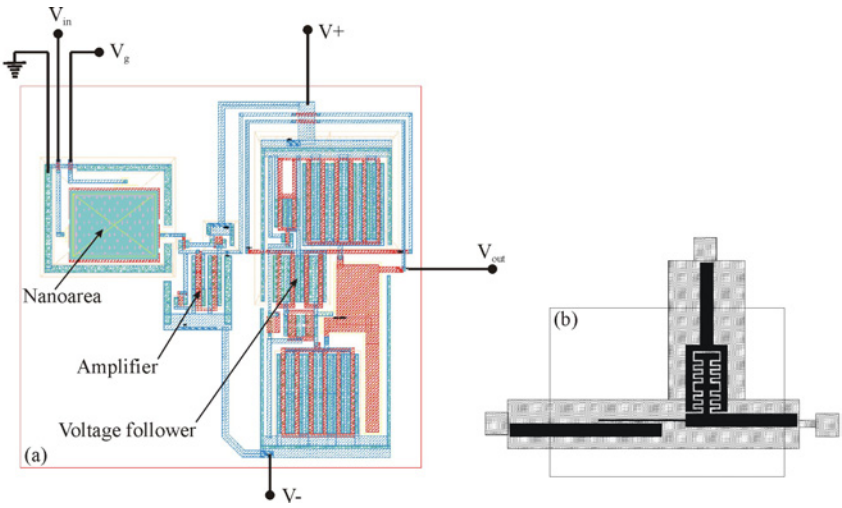

Figure 4.13: The 2nd generation BS circuit layout. Note that the underlying substrate of the cantilever can be accessed from a bonding pad and can thus be grounded.

The electrical characterization of the new BS circuit can be seen in figure 4.14, which shows in (a) the DC voltage output as a function of a static DC voltage input and (b) the gain as a function of an applied AC frequency. This characterization is performed on a test circuit, before the cantilever is fabricated and the poly-Si, with a resistance of 180Ω, is in its place. In figure 4.14a the DC characterization shows that V_{in} voltages below -1V and above 200mV the circuit is either in saturation or closed respectively. In the linear region the maximum gain, which is approximately 16dB. In figure 4.14b the frequency response of the circuit is seen. The bandwidth of the circuit is found to be 1.7MHz, which is quite high. For the cantilever simulations in section 4.1 the resonant frequency is approximately 700kHz. Furthermore, a cantilever with a width, height and length of 100nm, 1μm and 10μm respectively has a fundamental resonant frequency of 1.4MHz, which is still within the bandwidth of this circuit.

4.5.2 AC circuit

The new AC circuits are virtually the same except that the operational amplifier has been altered so that the gain is constant within the frequency range of the cantilever. The Schematic layouts of three types of AC circuits can be seen in figures 4.15 4.16 4.17. In figure 4.15a the four resistors and the capacitor of the circuit are indicated by the arrows, while in figure 4.15b a close-up of the

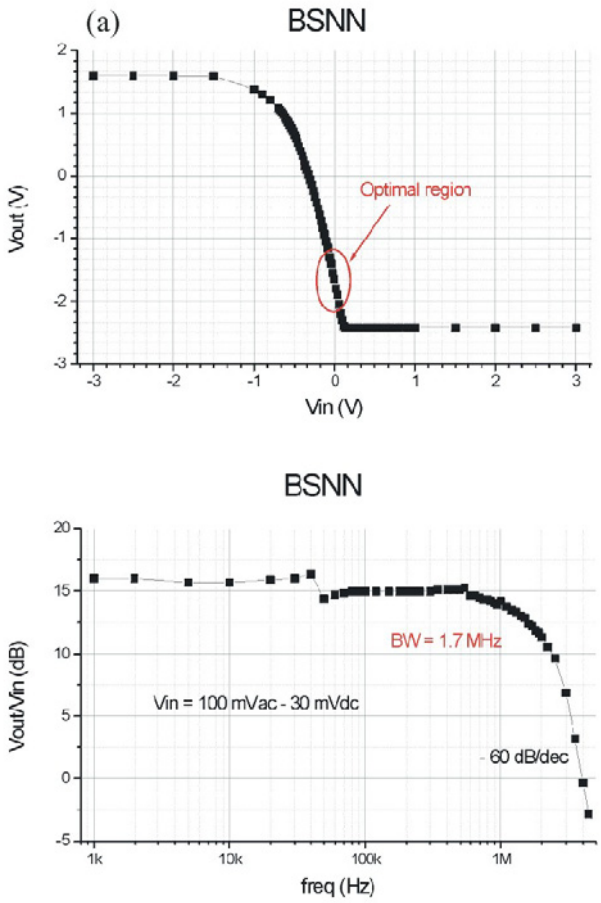

Figure 4.14: (a) the static transfer characteristic and (b) the frequency response of the BS circuit.

nanoarea showing where the cantilever/electrode design will be. In figure 4.16 a two electrode configuration is shown and again the nanoarea is seen in figure 4.16b. Finally, a two cantilever device has been added, which could be used as a differential measurement system. This new differential circuit and nanoarea can be seen in figure 4.17. The idea of this device is to use one cantilever as a reference cantilever while the other is used for measuring a mass change. By subtracting the two outputs from the two cantilevers any outside influences on the cantilever such as temperature variations can be filtered out. Also this device is the first step in designing future devices with an array of many cantilevers.

In figure 4.18 the frequency response of a BS and AC1 circuit is seen. It is seen that as described above, the gain of the BS is around 16dB and the band width is 1.7MHz. The AC1 circuit has a higher gain of around 32dB but a low band width of 150kHz. However these measurements were performed before the poly0

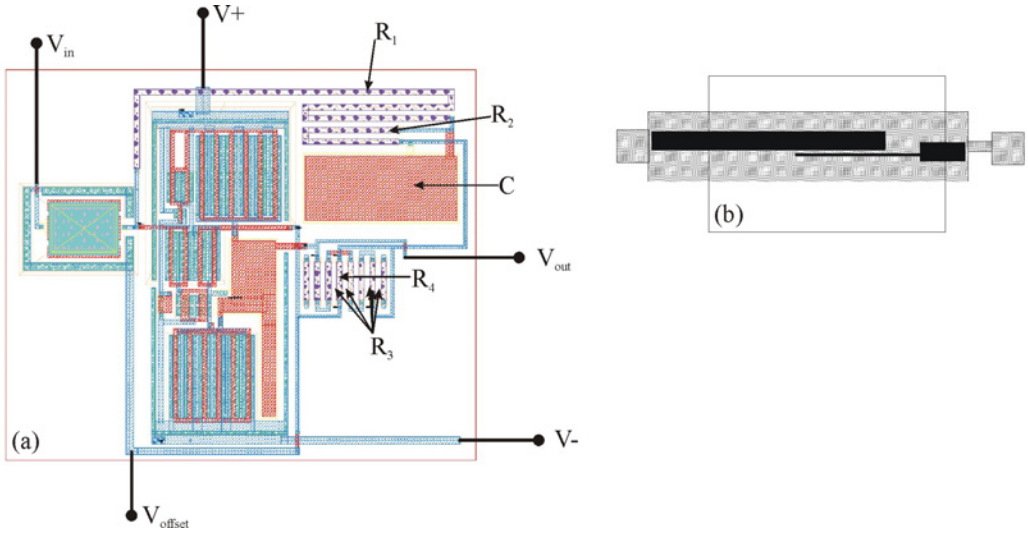

Figure 4.15: (a) Schematic layout of the one electrode AC1 type circuit and (b) a close-up of the nanoarea showing the placement of the cantilever electrode.

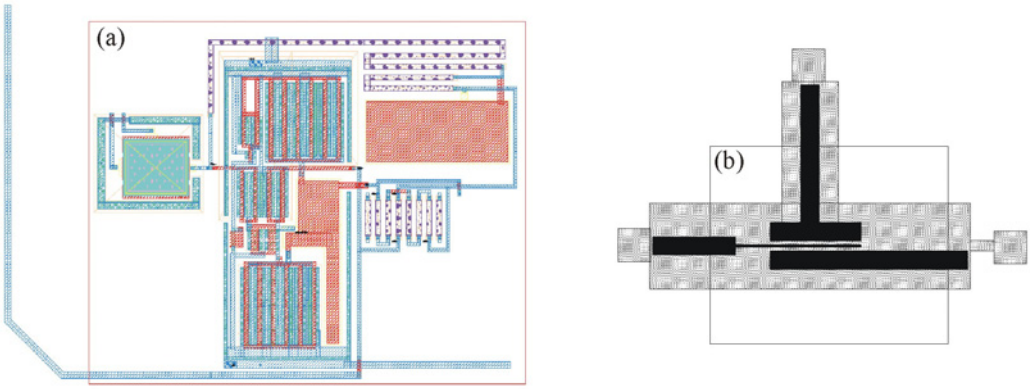

Figure 4.16: (a) Schematic layout of the two electrode AC1 type circuit and (b) a close-up of the nanoarea showing the placement of the cantilever and two electrodes.

layer has been processed to instead of a cantilever a 180Ω resistor is in its place, thus the optimum operating conditions were not used during this measurement.

4.6 Summary

In the beginning the SPICE model was used to illustrate the effects of parasitic capacitances on the cantilever based capacitive system. It was shown that parasitic capacitances below 300fF are needed to achieve the capacitive readout. This

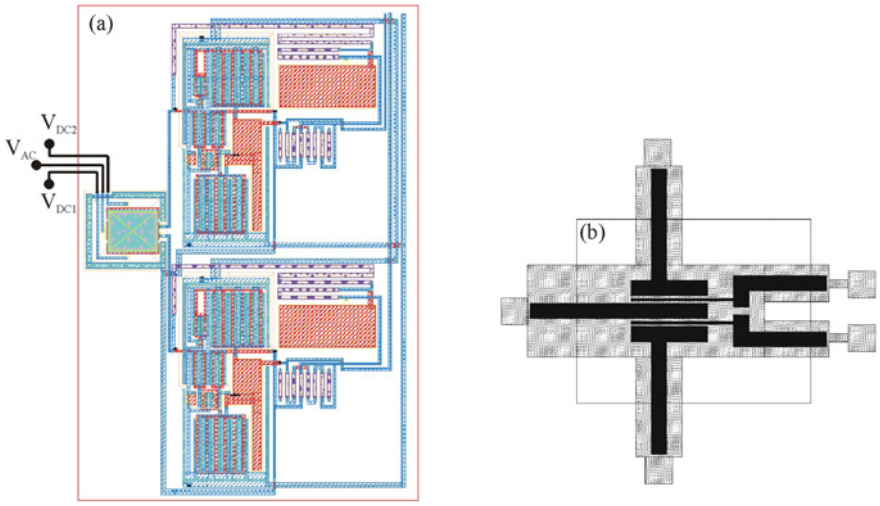

Figure 4.17: (a) Schematic layout of the differential device with two AC1 type circuits and (b) a close-up of the nanoarea showing the placement of the two cantilevers and two electrodes.

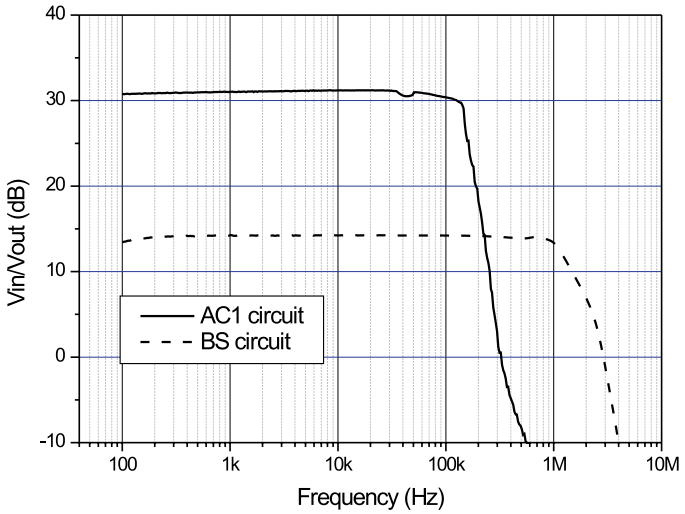

Figure 4.18: Two frequency responses comparing the BS and AC1 circuit. It is seen that the BS has a low gain and high bandwidth, whereas the AC1 circuit has a high gain and low bandwidth.

lead to the realization that integration of the sensor with CMOS is inevitable. Furthermore, the one and two electrode configurations where compared and it was determined that even though a higher DC voltage can be applied with the

two electrode configuration, the signal is not enhanced compared to the one electrode configuration.

The remainder of this chapter introduced the CMOS technology, which was used to realize the CMOS integrated cantilever based mass sensor. It was determined that the first attempt at CMOS integration would be based on a post-CMOS surface micromachining of the bottom poly0 layer of the CMOS. Furthermore, two amplification circuit designs were introduced and explained, namely the BS and AC circuits. Finally, the layout design of the first and second generation CMOS chip was presented.

Chapter 5

CMOS Integrated Cantilevers

5.1 Poly0 optimization

In section 4.2 it was concluded that the first approach to CMOS integration was to use the CMOS poly0 layer as the structural layer and the LOCOS oxide as the sacrificial layer, figure see 4.6. One of the reasons for choosing the poly0 layer is that it was the only layer that can be altered in order to optimize the surface roughness and thickness. A low surface roughness is desirable when performing the lithography processes, in order to decrease the line-width as much as possible. An increased height of the cantilever increases the vertical stiffness of the cantilever, which decreases the risk of vertical snap-in and it will also increase the static capacitance of the device, which will in-turn increase the mechanical vibrational current according to equation 2.2-18 and 2.2-19 by increasing the static capacitance C_0.

The poly0 thickness was increased from 350nm to 600nm, which was the thickest possible value without changing the CMOS characteristics considerably. In order to minimize the surface roughness both the deposition and doping techniques were investigated. The original poly0 was deposited by LPCVD at 610^0C and was doped by $POCl_3$ diffusion. A SEM image of the poly0 surface is shown in figure 5.1a. Figure 5.1b-e shows SEM and AFM images of two modified types of poly0 surfaces. Both poly0 layers are deposited with LPCVD at reduced temperature of 580^0C. Poly0#1 is ion implanted with phosphorus (see figure 5.1b and d) and poly0#2 is doped using the same $POCl_3$ diffusion gas as for the original poly0 (see figure 5.1c and e). Contact mode AFM was used to measure the root mean squared roughness of the samples. Table 5.1 shows the results of these measurements. The overall roughness is lowest on the poly0#2 sample, but the poly0#1 sample has a large overall roughness due to outgrowths. In between the outgrowths, the roughness is actually lower than the poly0#2. This surface is denoted poly0#1b in table 5.1. Energy dispersion spectroscopy (EDS) was used

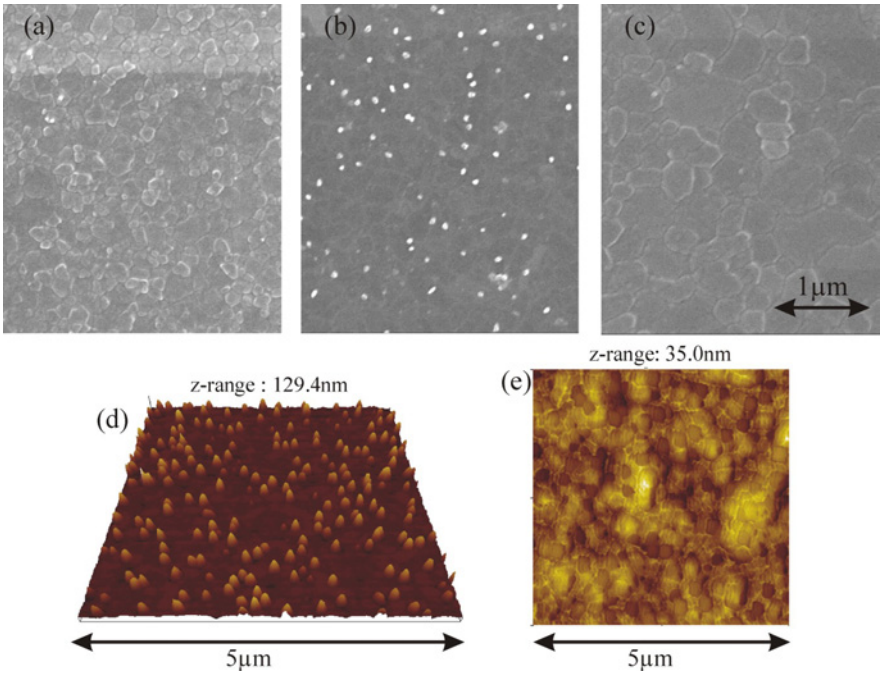

Figure 5.1: SEM images of (a) the original poly0 surface and (b) and (c) altered poly0 surfaces. (d) and (e) are AFM images of the poly0 surfaces seen in (b) and (c).

to analyze the elements in the outgrowths and it was found that they are Si and not contamination. It was decided that the final poly0 deposition and doping will be the poly0#2 recipe.

poly0 type	LPCVD temp (^{0}C)	doping	rms roughness	p-p roughness
poly0	610	$POCl_3$	5.1nm	38.4nm
poly0#1	580	ion implantation	11.2nm	123.4nm
poly0#1b	580	ion implantation	2.8nm	25.4nm
poly0#2	580	$POCl_3$	4.0nm	30.3nm

Table 5.1: The root mean squared (rms) roughness and the peak to peak (p-p) roughness of the poly0#1 and poly0#2 surfaces. poly0#1b is the roughness in between the outgrowths.

5.2 Process sequence

In the previous chapter the process sequence as well as the circuit design for the CMOS were presented. It was decided that the first attempt of integration of a mechanical cantilever will use the existing CMOS poly0 layer as the structural layer of the cantilever and that the LOCOS 1μm oxide will be used as the

sacrificial layer. Furthermore, the cantilever fabrication will be performed as a postprocessing sequence. The process sequence of the cantilever onto the CMOS chip is seen in figure 5.2.

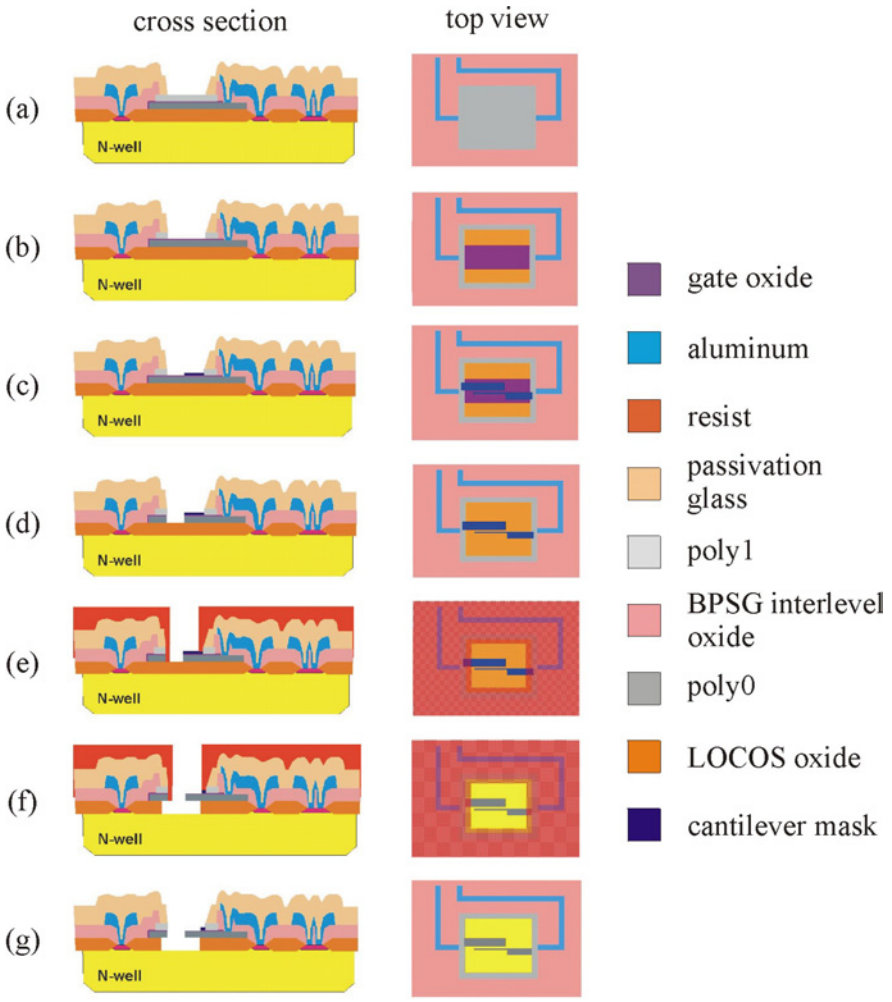

Figure 5.2: The post process sequence for fabrication of cantilever on CMOS circuitry. In (b), the poly1 is dry etched down to the thin gate oxide on top of the poly0, then in (c) the cantilever RIE mask is defined. In (d) the poly0 is RIE defining the cantilever structure in the poly0. In (e) a protective resist layer is deposited and a window is opened over the nanoarea. Finally, in (f) the cantilever is underetched in BFH and in (g) the protective resist is removed.

In the first step, figure 5.2a, a hole is opened in the CMOS passivation layer and the top poly1 layer is etched down to the thin gate oxide using dry etching, figure 5.2b. Now, a mask that defines the cantilever/electrode structure is defined, figure 5.2c. The types of lithography used for this step will be discussed in the

next section. The important thing is that this lithography step defines an etch mask that can withstand dry Si etching. In figure 5.2d the poly0 is etched using an anisotropic reactive ion etching (RIE), which is capable of producing vertical side walls. The RIE process is based on a SF_6 and O_2 plasma, which allows passivation of the side-walls in order to reduce lateral etching. In order to protect the CMOS during sacrificial layer etching, a protective resist is then deposited on the chip and a hole is defined over the nanoarea, figure 5.2e. In figure 5.2f, the underetching is then performed using buffered HF. This step is immediately followed by a drying technique, which is designed to avoid stiction between the cantilever and the bottom substrate or the lateral electrode, figure 5.2g. Two techniques have been investigated and used, which are freeze-drying and resist coating techniques. These techniques will be discussed further in section 5.4. The detailed description of this process can be seen in Appendix C.

5.3 Mask definition

For the realization of the CMOS integrated cantilevers laser and e-beam lithography have been used. UV lithography was not used because the sub-micrometer line-widths that are needed here would be difficult to realize since the mask would be separated from the nanoarea by the poly1 and the passivation layers, which are several microns thick, see figure 5.2c. AFM lithography, was also attempted, but due to the large poly0 surface roughness, finished cantilevers were not fabricated.

5.3.1 Laser fabricated cantilevers

The laser lithography process is based on first coating the chip with a 7-10nm thick aluminum layer. The Al layer is locally annealed by the focused laser beam and the mask pattern is directly written as described in sections 4.4 and 4.5. Then, the pattern is developed by wet etching the non-annealed Al, which leaves the laser annealed Al as an etch mask.

Laser writing optimization

Several measures have been taken in order to optimize the laser writing and Al etch process. As explained in section 3.2 the laser lithography setup consists of a laser, sample stage and optical lenses, which focus the laser onto the substrate on the x,y stage. The stage and AO modulator, which is used to turn off and on the laser, are both controlled by a PC and LabView software. The writing technique is based on converting the wanted pattern into a simple .lmm file, which breaks the pattern into horizontal or vertical lines. Then the pattern is generated by writing one line at a time. The .lmm file contains line segments that consist of two coordinates namely (x1,y1) and (x2,y2). These two coordinates correspond

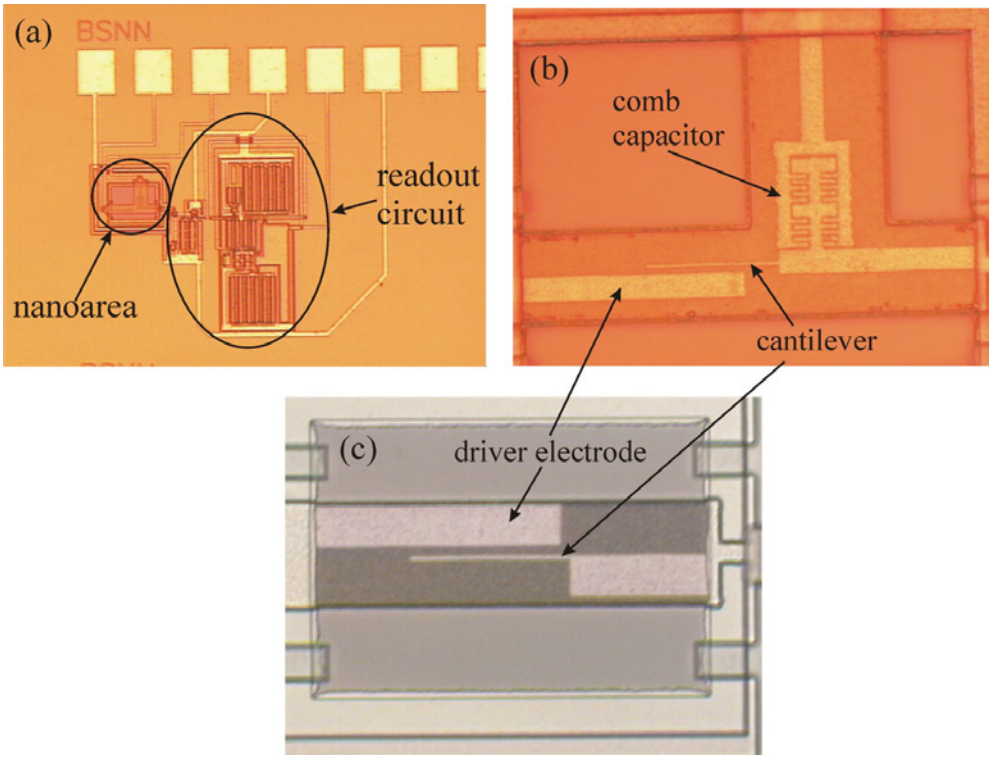

Figure 5.3: (a) The entire BS circuit and nanoarea and the laser defined mask after development for a (b) 2nd generation BS circuit and (c) 1st generation BS circuit.

to the beginning and end of each line segment that the laser writes. It was found that at the beginning and ending of each line, the power dose is higher due to acceleration effects. This results in a widening of the structure at the edges. Furthermore, it was found that the stage overshoots the last coordinate, upon deceleration, which results in a zig-zag line if the lines in the structure are written back and forth, see figure 5.4a. A SEM image of the zig-zag edge can be seen in figure 5.4b. The solution to the widening at the edges is to use a low scan speed, in order to minimize the acceleration effects. In order to resolve the zig-zag effects, the important structures are only written in one direction as seen figure 5.5a. Figure 5.5b shows a SEM image of a laser defined cantilever, where the driver and cantilever are written in one direction, thus reducing the zig-zag edge effect.

The Al etch was performed by immersing the chips into 80% phosphoric acid. The time to etch the 7-10nm thick Al varied between 2-6 minutes. The reason for the large variation is because the natural oxide that grows on the Al has a very slow etch rate compared to the Al. The thickness of the natural oxide depends on how long the Al coated sample has been exposed to air, thus older samples

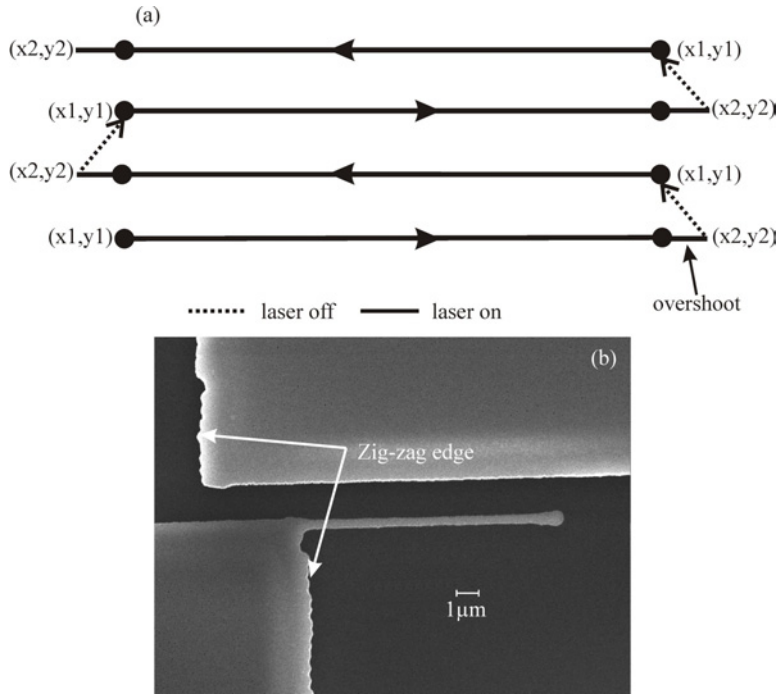

Figure 5.4: In (a) the concept of writing lines back and forth is shown, which can lead to a zig-zag edge effect as seen in the SEM image in (b).

tend to take longer time. Figure 5.3 shows some optical images of laser annealed masks on the nanoarea.

Fabrication results

Figure 5.6 shows some SEM images of final cantilever structures, which have been defined by laser lithography. It can be seen that the side wall roughness is quite large and that the top of the cantilevers are very porous. These problems with the poor structural quality of the cantilevers is due to the poor mask quality of the laser annealed mask. Since the Al thickness, 7-10nm, is comparable to the poly0 surface roughness, pinholes in the mask is very probable. Furthermore, the edges of the laser annealed mask are not very well defined, which could be because of thermal spreading of the heat during the local annealing. The minimum width achieved with laser lithography is approximately 700nm.

Reproducibility problems

Since the laser lithography is a thermal process the thermal properties of the substrate influence the laser annealing greatly. This means that the writing power of the laser is different for different substrate layer thicknesses, such as the poly-Si thickness, the oxide thickness and the Al thickness. Also the doping

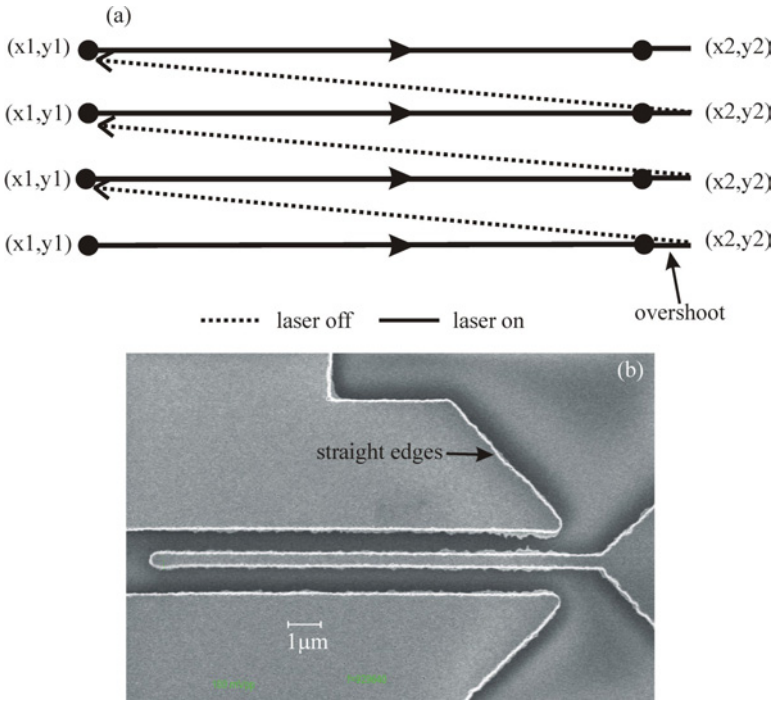

Figure 5.5: In (a) the concept of writing lines in one direction is shown, which reduces the zig-zag edge effect as seen in the SEM image in (b).

level of the poly-Si layer influences the writing. In-fact it was found that laser writing on Al coated p++poly-Si could not define a mask [81][100], which could be because of the high thermal conductivity of this substrate. In order to solve this problem and to make the process more reproducible a thin SiO_2 layer is used between the poly-Si and the Al layers. In the CMOS process the gate oxide is used as this separation layer.

Aluminum surface investigation

It has been seen that the mask quality of the laser annealed mask is quite poor. In order to investigate this, Al was deposited on both clean Si and SiO_2 surfaces at a thickness of approximately 7nm and the surface was examined by SEM and AFM. In figure 5.7a and b SEM images of two types of surface can be seen, which are Al on Si and Al on SiO_2, respectively. Prior to the deposition of Al, the Si substrate was dipped in HF, which etches away any natural oxide and passivates the surface with hydrogen. It is seen that the Al coated SiO_2 has many pinholes and that the Al formes a structure on the surface. Whereas the Al coated Si substrate is very flat without any pinholes. It seems that the surface energy for the Si and SiO_2 surfaces is quite different and that thin Al on SiO_2 does not coat the surface evenly, which can explain the poor mask quality.

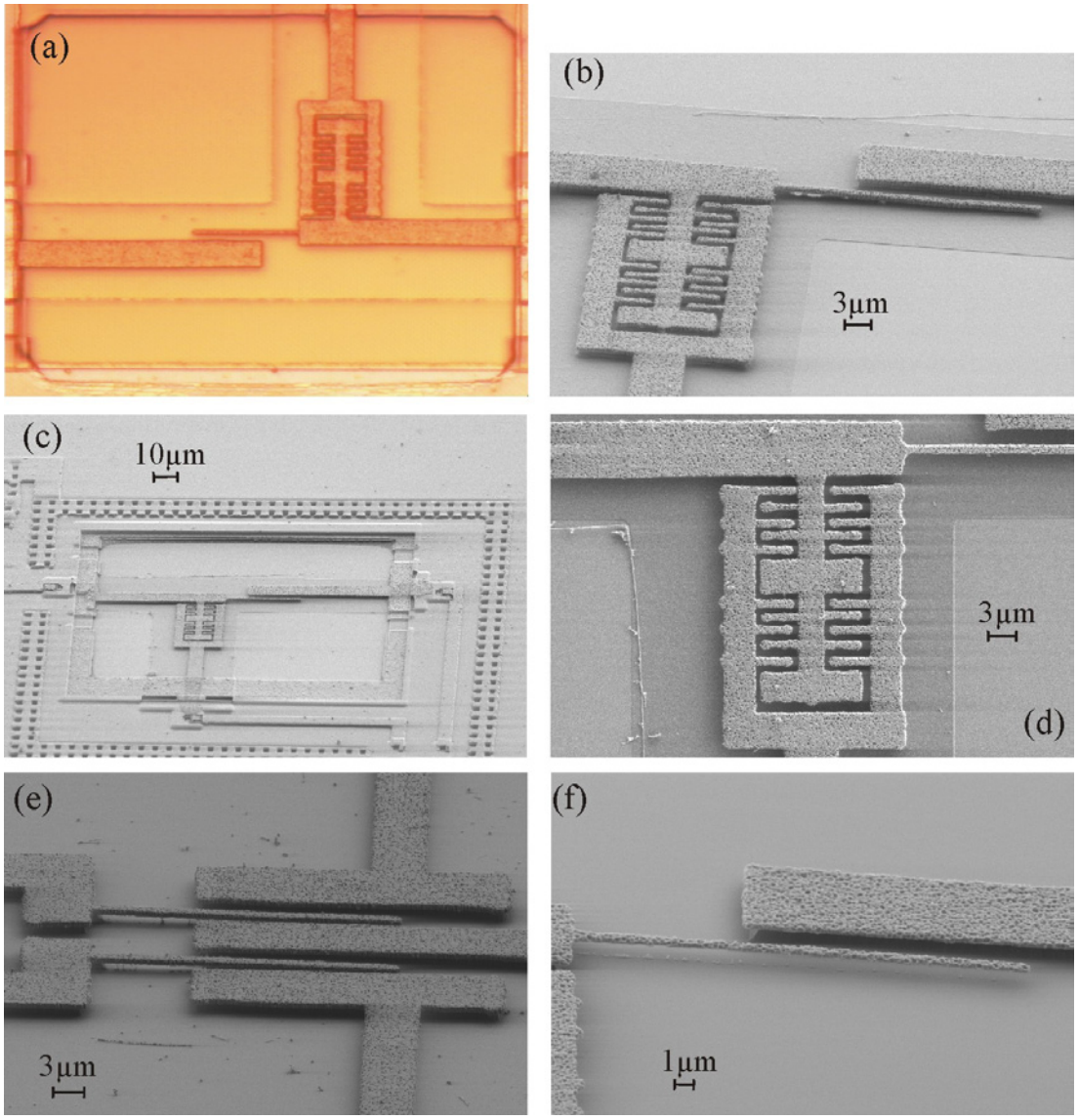

Figure 5.6: (a)-(d) finished BS cantilevers with integrated comb capacitor, which have been defined by laser lithography and (e) the differential cantilever design and (f) a single cantilever device.

In order to solve this problem, several treatments of the SiO_2 surface prior to Al deposition, such as chemical and plasma cleaning treatments and HMDS passivation of the SiO_2 surface, have been investigated. In figure 5.7 the results of the (c) argon plasma treatment and (d) HMDS treatment are seen. It is seen that the pinholes are gone for both treatments. The HMDS process consists of first heating the substrate under vacuum, which desorbs any H_2O in the SiO_2 and then

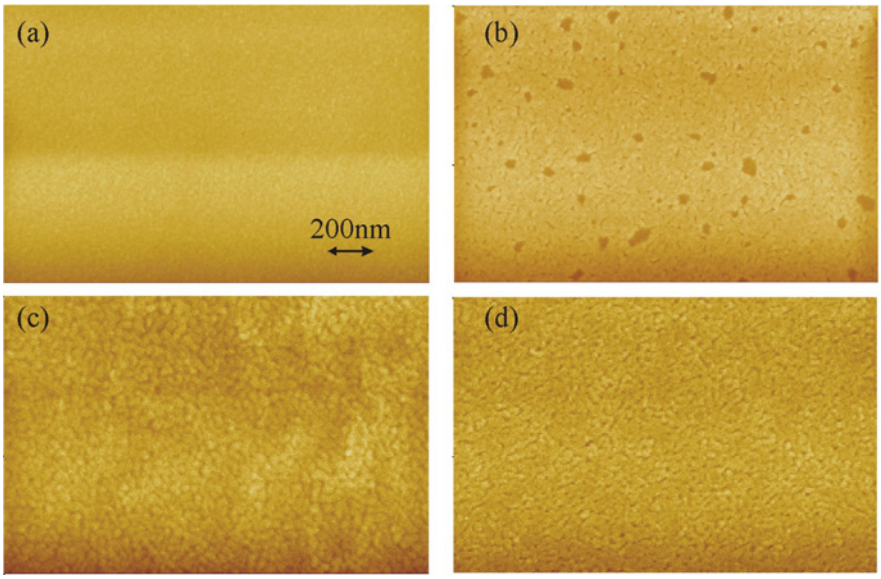

Figure 5.7: SEM images of (a) 7nm Al deposited on hydrogen passivated Si, (b) 7nm Al on SiO_2, (c) 7nm Al on a Argon plasma treated SiO_2 surface and (d) 7nm Al on a HMDS treated SiO_2 surface.

the surface is passivated with HMDS molecules, which has a hydrophobic group on it making the surface hydrophobic. HMDS is normally used as an adhesion promoter between SiO_2 and resist. In figure 5.7d the Al coated SiO_2 surface is pinhole free, which can be explained by the fact that the SiO_2 is clean and not being contaminated due to the HMDS passivation.

In order to measure the surface roughness, AFM has also been performed on the different surfaces. The results can be seen in figure 5.8. In table 5.2 the root mean square (rms) and the peak to peak (p-p) roughness values are listed. The Al coated Si surface has the least roughness whereas the plasma treated SiO_2 surface has the highest rms roughness and the untreated Al coated SiO_2 surface has the largest p-p roughness. The possible reason why the plasma treated SiO_2 surface has the largest rms roughness is that the surface has been physically etched by the Argon plasma prior to Al deposition. By looking at figure 5.8b, the holes are again seen in the surface and the line scan shows that the depth of the holes are approximately 7nm deep, corresponding to the thickness of the Al layer. The HMDS treated surface has the lowest rms and p-p roughnesses for the Al coated SiO_2 surfaces.

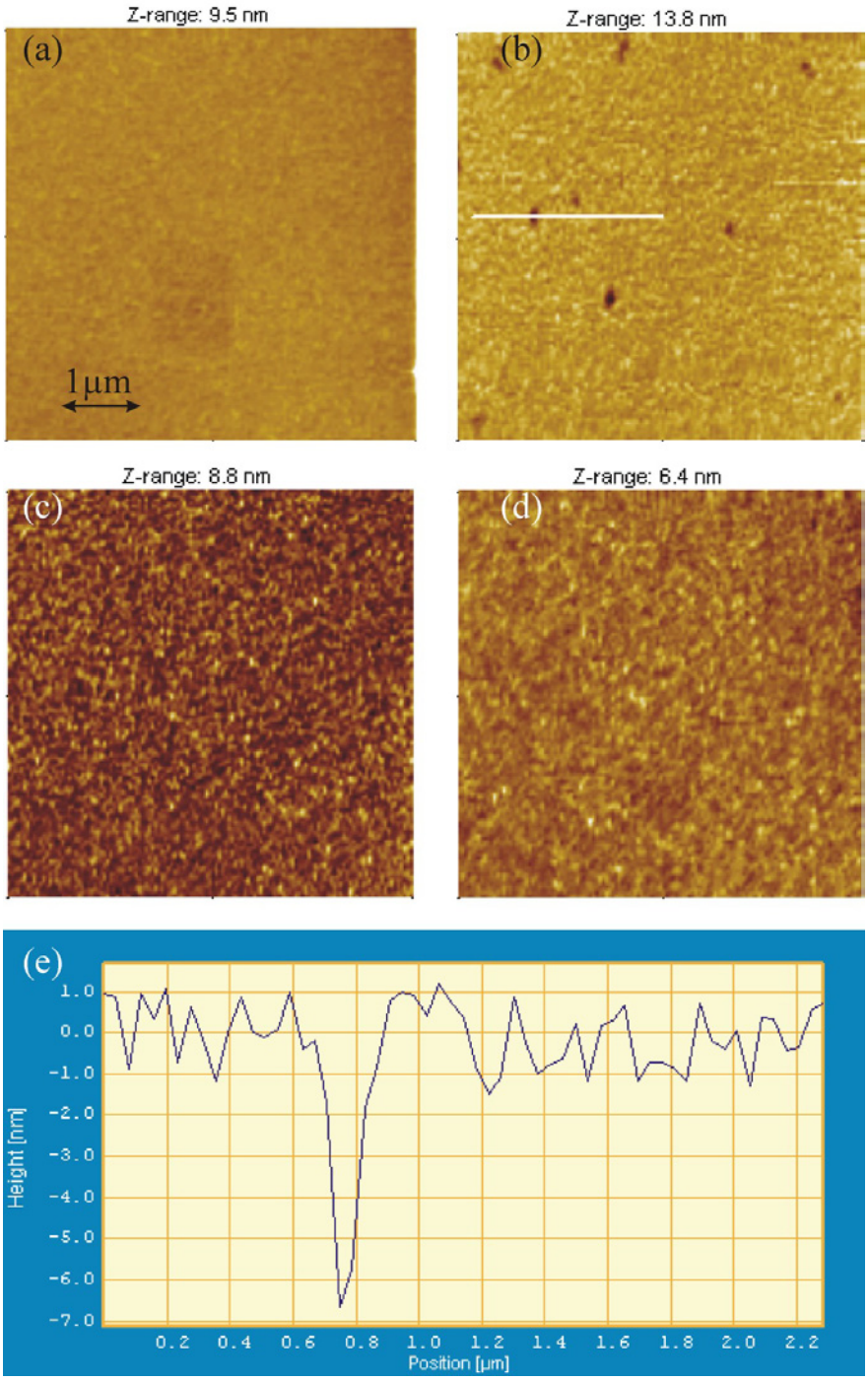

Figure 5.8: AFM images of (a) 7nm Al deposited on hydrogen passivated Si, (b) 7nm Al on SiO_2, (c) 7nm Al on a Argon plasma treated SiO_2 surface and (d) 7nm Al on a HMDS treated SiO_2 surface. In (e) a line trace of image (b) showing the depth of the holes on the surface to be approximately 7nm.

surface treatment	rms roughness	p-p roughness
Al on Si	0.494nm	2.08nm
Al on SiO_2 - no treatment	1.18nm	9.68nm
Al on SiO_2 - 250W Ar plasma	1.34nm	8.35nm
Al on SiO_2 - HMDS	0.685nm	4.46nm

Table 5.2: The root mean squared (rms) and the peak to peak (pp) roughnesses for four Al coated surfaces.

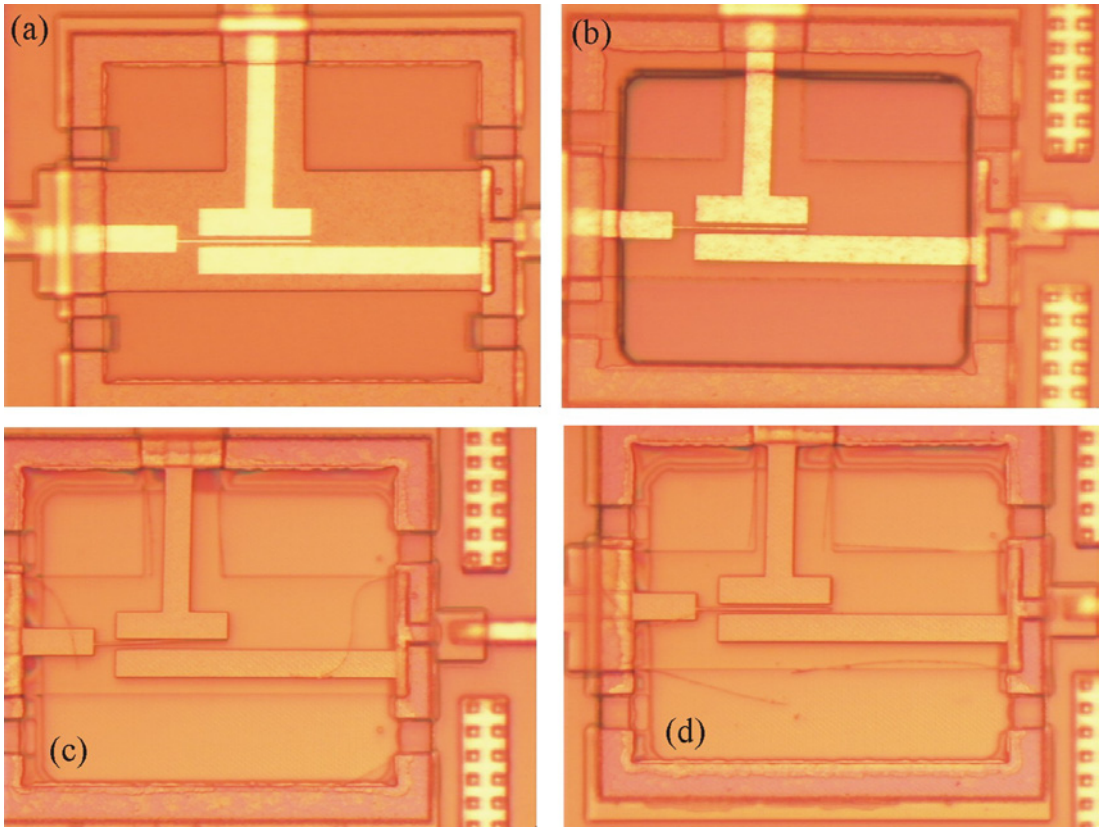

Figure 5.9: Optical images of (a)the EBL defined Al mask (b) the poly0 structure after RIE (c) and (d) the poly0 structure after underetching.

5.3.2 EBL fabricated cantilevers

In order to achieve line-widths below 500nm, which is required according to WP1 (section 1.4.2), EBL was also used to define cantilever etch masks. The EBL system that was used is located at Lund University and the mask patterning is based on a metal lift-off technique, which was developed and performed in Lund [103]. The process sequence is as follows. First, a two layer resist is used, where the top layer is sensitive to e-beam radiation. The resist is exposed and developed in a positive process using direct writing. After development a 30nm thick Al

layer is deposited and then the metal is lifted off by etching the resist in acetone. Optical images of the different process steps can be seen in figure 5.9. In figure 5.9a the 30nm thick Al mask is seen inside the nanoarea, which is used to define the cantilever and electrode structure during RIE. The result after RIE is seen in figure 5.9b, where the structure is very well defined. In figure 5.9c and d and in figure 5.10 optical and SEM images of the finished cantilevers can be seen. It is seen that both the side walls and the surface of the poly0 cantilevers are pinhole free and have very sharp, well defined edges, which proves that the 30nm Al mask is well defined and is a very effective RIE mask.

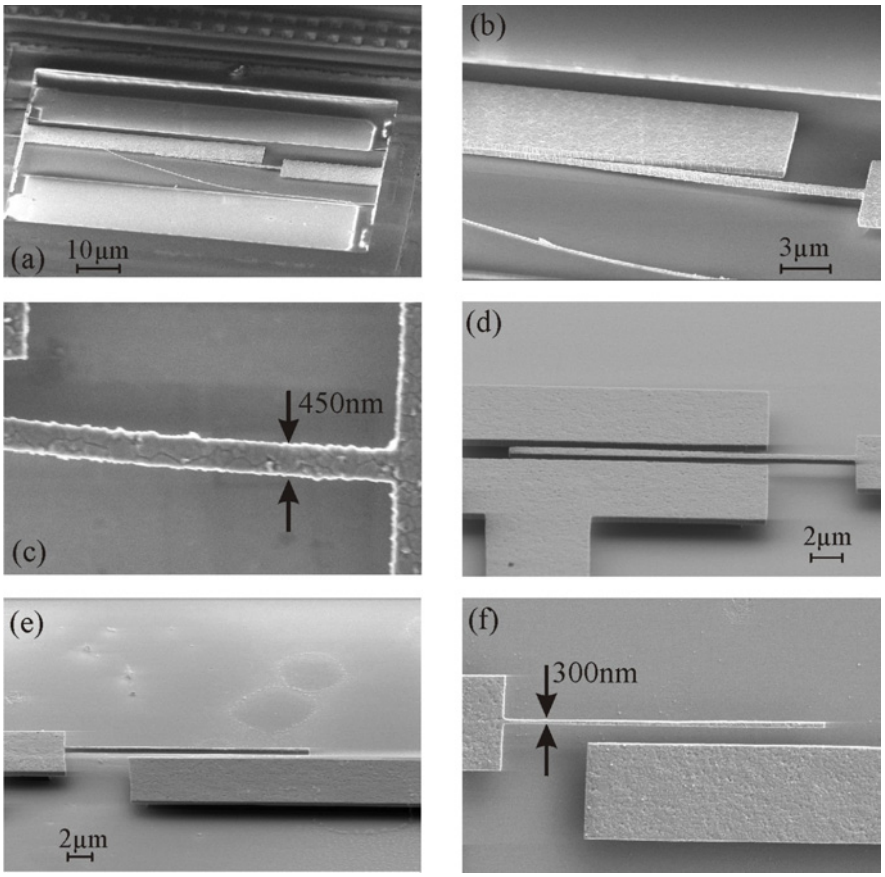

Figure 5.10: SEM images of EBL defined cantilevers which are sticking under the electrode in (a,b and c) and are not sticking in (d,e and f), which is a result to different releasing techniques. The smallest cantilevers have widths of 300nm.

5.3.3 AFM defined cantilevers

As stated in section1.4.2 AFM is being investigated as an alternate nano-lithography technology to EBL. Therefor an attempt of defining the mechanical system in the

nanoarea was made by AFM lithography.

The mask definition is similar to that of laser lithography. First, a thin 7-10nm Al layer is deposited on the CMOS chip. Then, a rough alignment of the AFM tip to the nanofabrication area is done by the optical microscope integrated with the AFM, then the area is scanned and the final alignment is performed. Some results of the AFM oxidation can be seen in figure 5.11. Due to the large roughness of the poly0 surface of approximately 30nm p-p, the AFM oxidation could not be seen with the AFM after oxidation, but in figure 5.11b and c the Al-oxide structure is clearly seen by optical microscopy. In figure 5.11b a close-up of the nanofabrication area is shown, where the AFM oxidized area is seen as the dark pattern inside the circle. In figure 5.11c the Al oxide mask is clearly seen. It is also worth noting that the large optical contrast demonstrates that the refractive index of the oxidized Al has changed significantly. The size of the large rectangles is approximately 6x6μm^2 and the width and length of the line and the gap distance between the line and larger square are approximately 500nm, 8μm and 500nm respectively.

In order to finish this device, laser lithography was used to pattern wires from the AFM defined pattern to the edges of the nanoarea. Unfortunately, during the wet etching of the chip, the Al-oxide/Al-annealed mask was overetched and the structure did not survive the RIE.

Due to the large roughness of the poly0 the reproducibility of the AFM writing is very unstable. Due to the native Al-oxide, high voltages were needed to oxidize the Al and due to the large roughness, dielectric breakdown occurs, which destroys the nanoarea surface completely. In order to remedy this problem non-contact AFM lithography can be used[96][99], but again, due to the large roughness it is very difficult to avoid contact between the AFM tip and sample. In the next chapter the optimization of AFM lithography on flat surfaces is described.

5.4 Dry release techniques

Previous devices that have been fabricated by laser writing on test substrates, without CMOS, have been dried by N2 gas after underetching of the cantilever in BHF and DI water rinsing [81][100]. On the test substrates the thickness of the structural poly-Si layer was 2μm, and the sacrificial layer thickness was 4.5μm thick. With these dimensions stiction of the cantilever to the bottom substrate was never observed. On the CMOS substrate the structural poly-Si layer is only 600nm thick and the sacrificial SiO_2 layer is only 1μm thick. This means that for a cantilever with the same length and width the vertical spring constant will be 37 times smaller (equation 2.1-2), when the cantilever height is reduced from

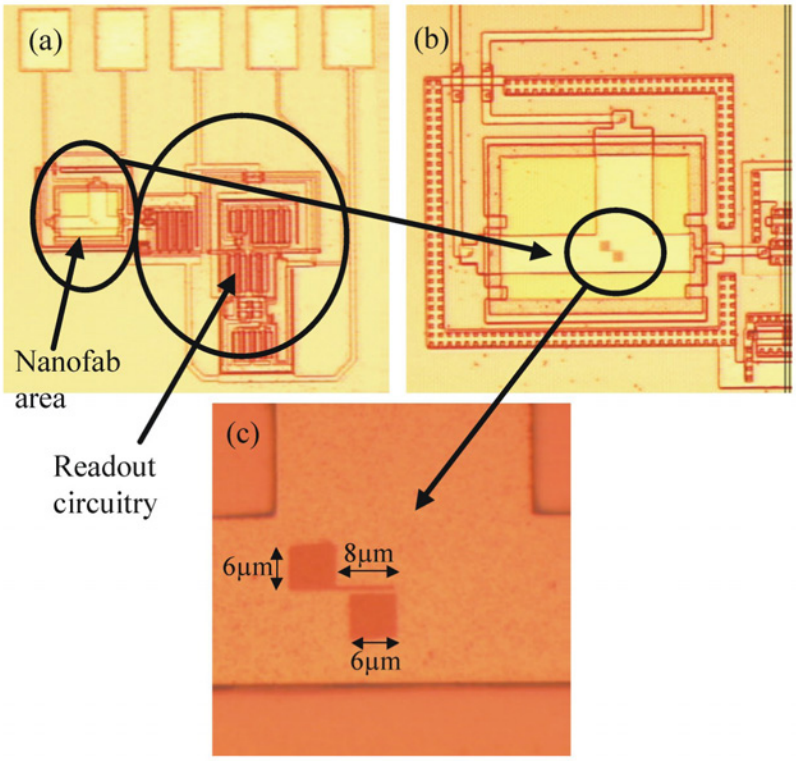

Figure 5.11: In (a) the whole BS circuit and nanoarea is shown. In (b) a close-up image of the nanoarea showing the AFM oxidized pattern and in (c) another close-up showing the details of the structure.

2μm to 600nm. Furthermore, since the gap between the cantilever and bottom substrate is only 1μm, the risk of stiction due to capillary forces upon drying or due to electrostatic forces under operation is much higher. In figure 5.12a a SEM image of a 40μm long, 600nm high and wide cantilever is seen after underetching and N2 drying. As can be seen, almost the entire cantilever is sticking to the substrate.

In order to avoid the capillary forces that cause the cantilever to stick to the substrate during drying the cantilever from a wet state, several dry-release methods can be used [104]. By releasing the structure in a dry state the capillary forces are greatly reduced and stiction during fabrication can be prevented. Two specific release techniques have been investigated which are a freeze-drying [105] and the resist assisted [106] technique.

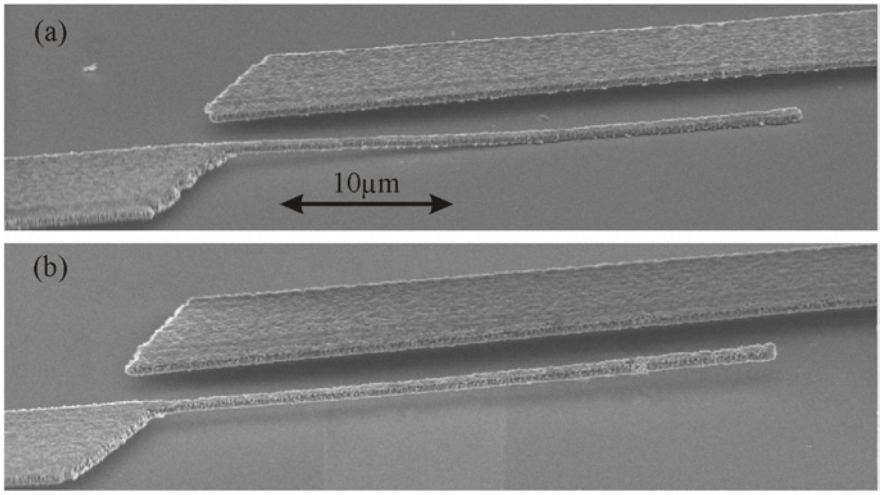

Figure 5.12: SEM images of poly0 cantilever that are approximately 600nm in width and thickness and 40μm long and which in (a) has been dried using N_2 and (b) using the freeze drying technique.

5.4.1 Freeze-drying technique

The freeze-drying process sequence can be seen in figure 5.15. Immediately after underetching the chip is rinsed in DI water several times, figure 5.15b. Then, without letting the chip dry, the chip is transferred to an acetone bath where the protective resist is etched away, figure 5.15c. The chip is then rinsed several times with acetone to make sure all the resist is removed and the chip is then rinsed in proponal. This if followed by the chip being immersed in liquid tert-butanol, which has a high freezing temperature of 25^0C. Finally, the chip is placed on a cooling plate inside a small vacuum chamber, where the tert-butanol solidifies, figure 5.15d. Finally, the tert-butanol slowly evaporates under vacuum, figure 5.15e. An image of the freeze-drying chamber can be seen in figure 5.13. A SEM image of a free-standing cantilever that is not sticking to the substrate can be seen in figure 5.12b, which can be directly compared to the cantilever dried in N_2. A detailed process sequence can be seen in Appendix D.

However, it was seen that the freeze-drying technique is not very stable, which could be due to contamination of the tert-butanol with H_20 or other chemicals that have a lower freezing point. In figure 5.14, images of a surface after freeze-drying with contaminated tert-butanol is shown. Because of this, other dry release options where examined and a resist based technique was then adopted.

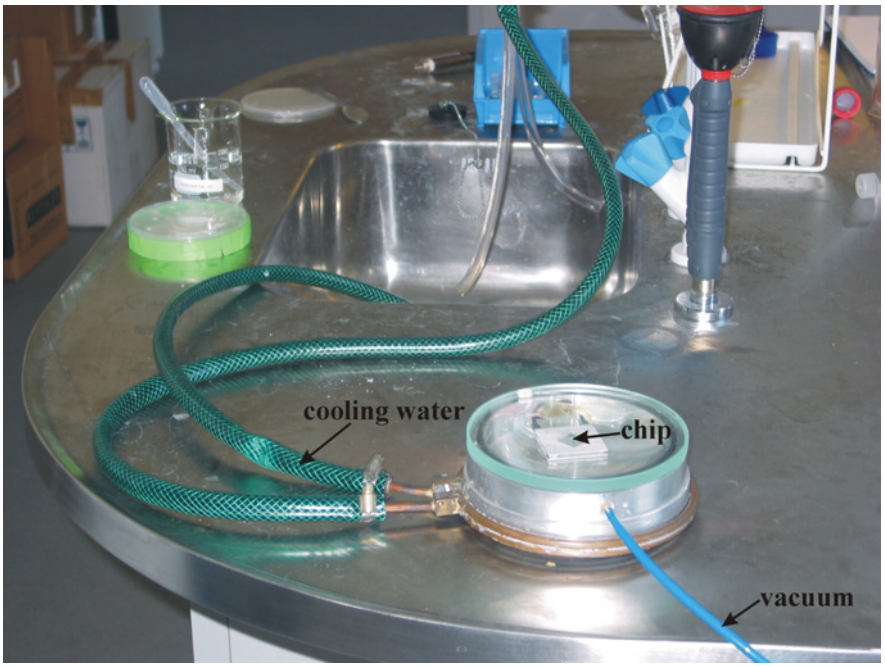

Figure 5.13: Image of the freeze drying setup where the chip is placed into a cooled vacuum chamber

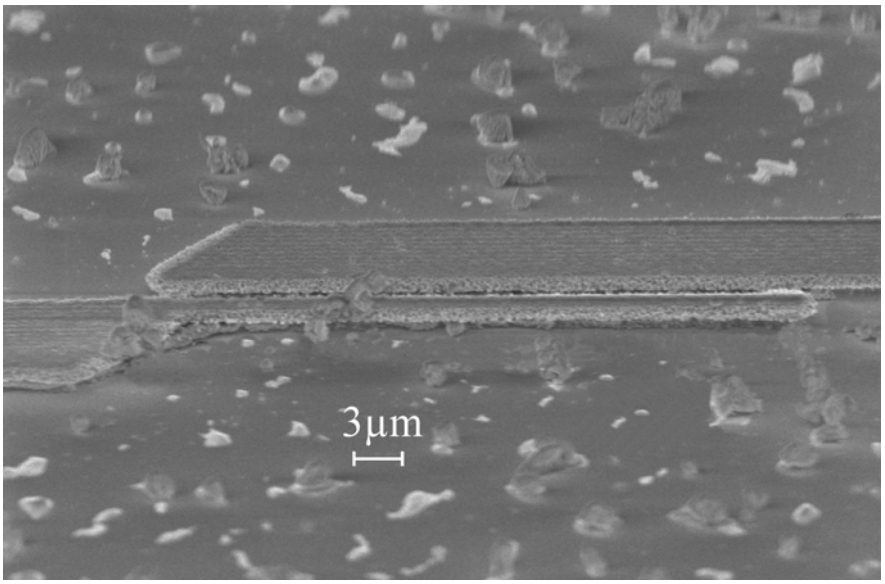

Figure 5.14: SEM image of a contaminated surface after freeze-drying.

5.4.2 Resist technique

The process sequence of the resist technique can also be seen in figure 5.15. First, the chip is rinsed in DI water just after underetching, figure 5.15b. Next, the pro-

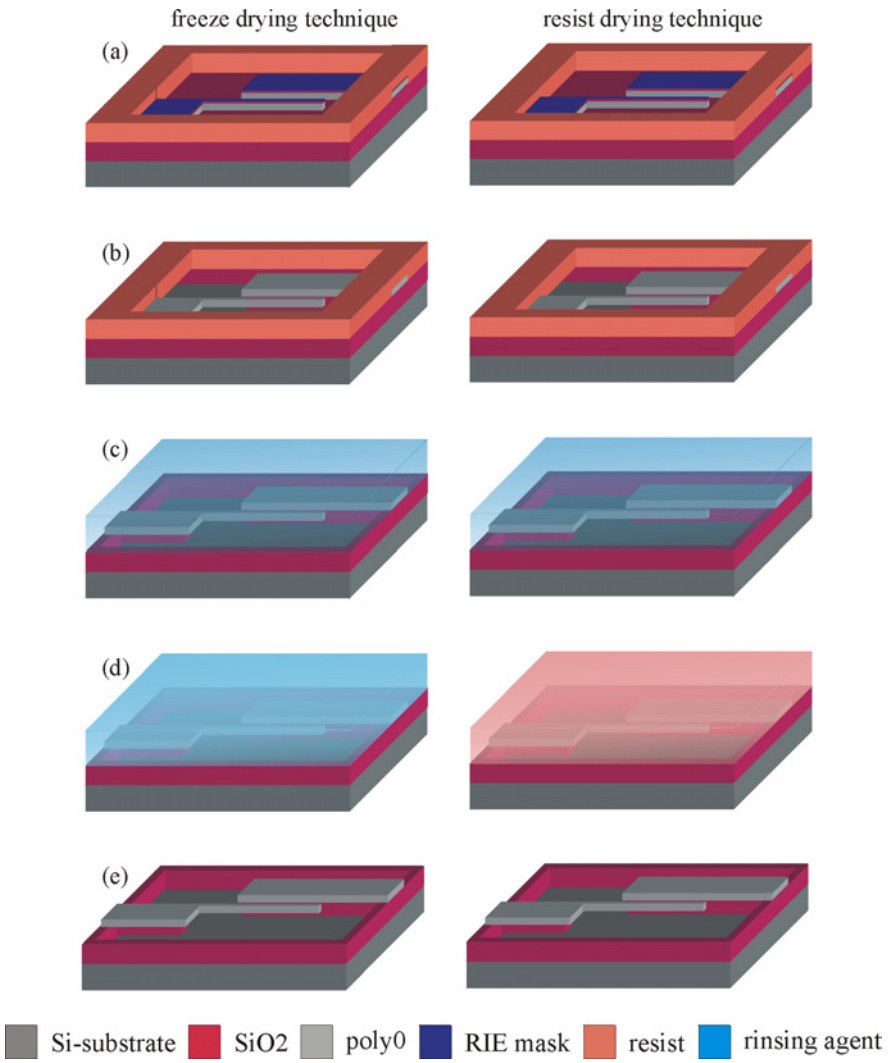

Figure 5.15: Process sequences of the freeze drying (left) and resist (right) dry release techniques. In both processes the cantilevers are rinsed several times with DI water (c). For the freeze-drying process the chip is immersed in tert-butanol(d) and then the chip is placed on a cooled plate in a vacuum chamber until the tert-butanol has evaporated (e). For the resist process the chip is coated with photoresist (d) and then soft baked and finally the resist is etched in an O_2 plasma (e).

tective resist layer is removed in acetone, figure 5.15c. The chip is then rinsed several times in acetone and the chip, in a small amount of acetone, is diluted with photoresist (the same type used for photolithography), figure 5.15d. The chip is spun so that an even resist coating of a thickness of 1-2μm is obtained. This is followed by soft-baking the chip with the resist coating at 90^0C for 1 minute. Finally, the resist is etched away in an O_2 plasma and the cantilevers are released, figure 5.15e. In figure 5.16a an optical image of the cantilever prior

to O_2 plasma etching shows the cantilevers encased in resist. At this step the cantilever can be seen not to be sticking to the substrate, with optical microscopy. A detailed process sequence can be seen in Appendix E.

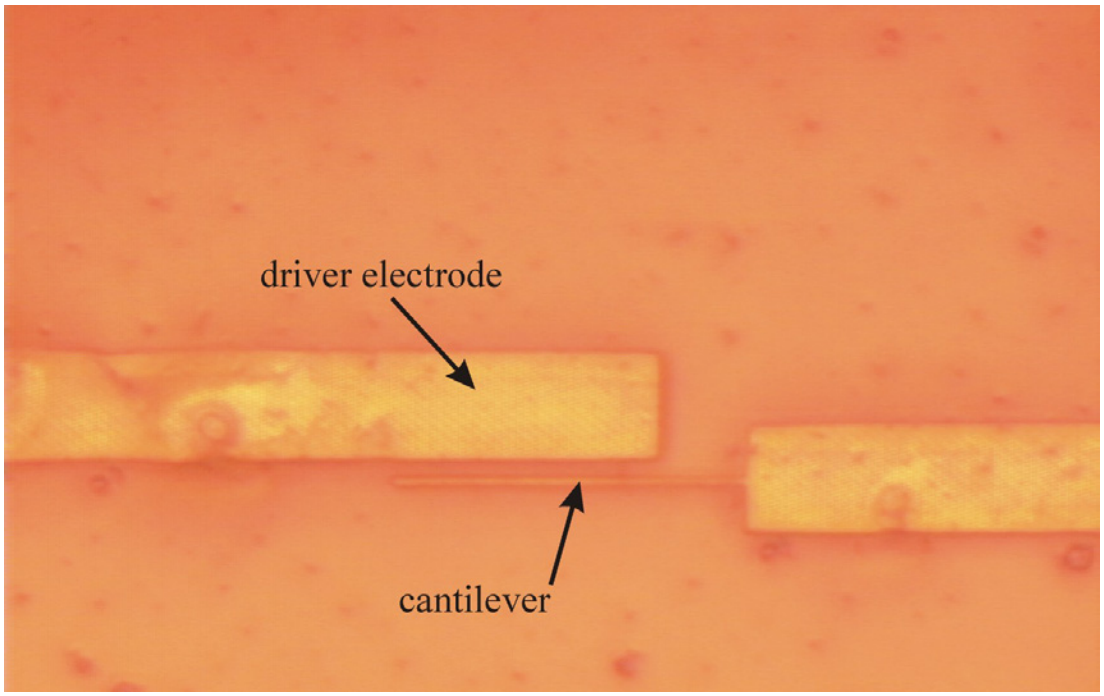

Figure 5.16: Optical image of resist encapsulated cantilever in the nanoarea

The advantages of this process is that (1) the reproducibility is much higher since there is no possibility of contamination during the release step, (2) the resist acts as a protection layer for the cantilevers, which can be removed just before use and (3) an additional anti-stiction coating process can be implemented just after the O_2 plasma dry release process in the same reaction chamber. This anti-stiction layer coating will be discussed in the next section.

5.5 Anti-stiction layers

By using dry release techniques it is possible to fabricate cantilevers, which are very long and narrow, that are not sticking to either the bottom substrate or the parallel electrode. But, it could also be advantageous that the cantilever does not stick to the substrate or to the parallel electrode after fabrication or during operation, which is called "in-use" stiction. In this case an anti-stiction layer should be used to passivate the cantilever so that is cannot stick to other surfaces. Several anti-stiction layer deposition techniques have been developed, since the

in-use stiction is a major problem in both NEMS and MEMS design . The two important types of anti-stiction layers are the FC coatings [107][108][109][110], in which a hydrophobic FC layer is deposited in a C_xF_{n+x} plasma and the deposition of a self assembled monolayer (SAM) [111], which has a hydrophobic teflon molecule attached to it. The advantage with the FC coating is that it can be performed directly after the O_2 plasma release step in the same facility. The implementation of anti-stiction layers in the cantilever fabrication is presently being pursued within the NANOMASS project.

5.6 Post-processing effects on CMOS

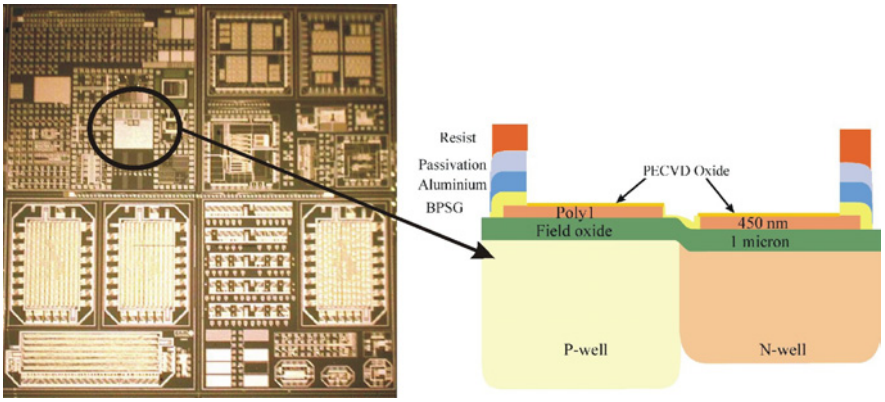

Figure 5.17: (left)An optical image of the test chip used to test the post processing influences on CMOS and (right)the cross section of the area used to fabricate cantilevers.

In order to characterize the post processing effects on the CMOS a test chip was used, which was characterized after each individual step of the post processing, see figure 5.17. This chip was taken from a standard CMOS characterization wafer, which is run in parallel to each CMOS run in order to test the CMOS parameters and thus make sure that the technology is standard. On the test chip an open area was found and a hole is opened in the passivation layer down to a poly1/SiO_2/Si sandwich layer as seen in figure 5.17. In this area the poly1/SiO_2/Si sandwich structure is coated with a 60nm thin PECVD oxide and then a 7nm thin Al layer. Cantilevers were then fabricated using laser lithography and the post processing sequence described above. Images of these cantilevers can be seen in figure 5.18. It was found that two processes damage the CMOS parameters, which are the metal evaporation deposition and SEM imaging/EBL lithography.

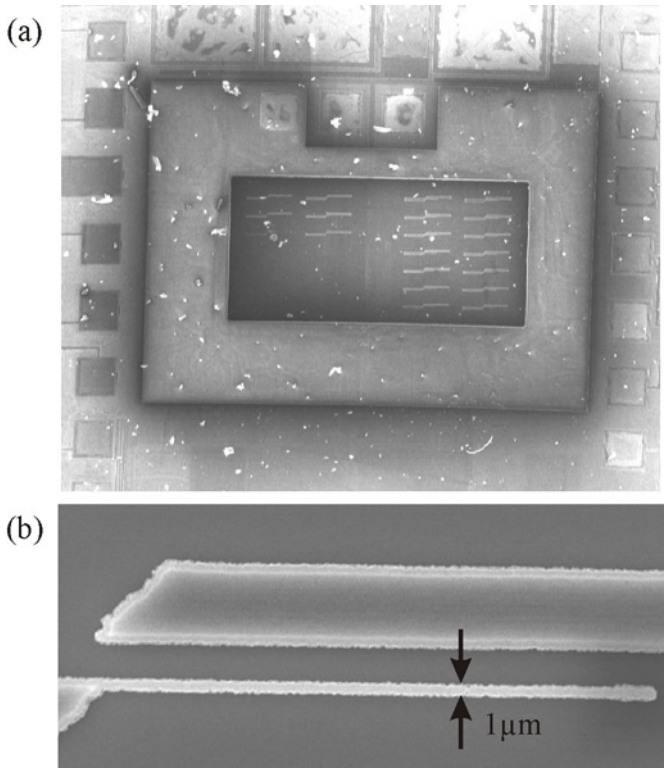

Figure 5.18: (a) SEM image of the entire process area with many cantilevers, one of which can be seen in (b).

5.6.1 Metal deposition effects

Upon metal deposition the threshold voltages of the PMOS and NMOS transistors shifted to a lower value, which is outside the acceptable technological value. The results of the NMOS threshold voltage is shown in figure 5.19. It is seen that the threshold voltage is measured before any post processing and then again after the metal deposition. The metal evaporation process is an E-beam evaporation, where the metal is heated by a focused electron beam. This process produces X-rays, which are harmful to the CMOS. The X-rays create electron/hole pairs and the electrons get trapped at the gate SiO_2 metal interface of the transistors, which accounts for the threshold voltage shifts [112]. This type of radiation damage is easily remedied by annealing out the trapped charge at 350^0C for 30minutes. This can be seen in figure 5.19, where the threshold voltages return to normal values.

5.6.2 SEM and EBL effects

Another source of CMOS damage is irradiation with high energy electrons from a SEM or during EBL. Actually, this effect was not discovered until working

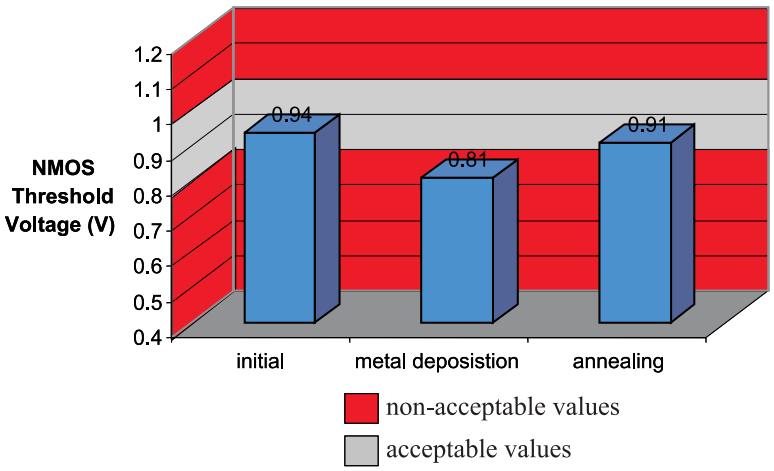

Figure 5.19: Bar graph showing the NMOS threshold voltage of the CMOS initially before metal deposition, after metal deposition and after annealing the CMOS at 350^0C for 30 minutes.

with the 2nd generation CMOS chips because EBL was not available until this time. It was discovered that the CMOS circuitry with the very nice EBL defined structures, which are shown in figure 5.10, are totally in-operable. In order to investigate the effects of electron radiation an on-line measurement of the BS circuit properties was performed. During SEM imaging, an investigation of the BS circuit's frequency response, show that at lower acceleration voltages, below 5keV, the CMOS is unaffected and neither the gain or bandwidth vary, even after several hours of radiation, see figure 5.20. But at 5keV the CMOS starts to degrade and after 5minutes of radiation the bandwidth (BW) is reduced from 1.3MHz to approximately 1.0MHz.

The CMOS circuitry has also been characterized before and after EBL, which uses a high acceleration voltage of 25keV. After exposing the nanoarea, with the PMMA resist, the circuitry is completely inoperable . Even after several hours of heat treatment the CMOS could not recover. This shows that e-beam radiation at such high energies is exerting structural damage to the transistors, which cannot be annealed out at 350^0C. At present these problems are being addressed within the NANOMASS project.

5.7 Summary

In this chapter the fabrication of the poly-Si based cantilever on CMOS circuitry is presented. First, the optimization of the poly0 layer was shown. The poly0 layer was increased in thickness from 350nm to 600nm, which will increase the static capacitance of the cantilever/electrode system and increase the vertical

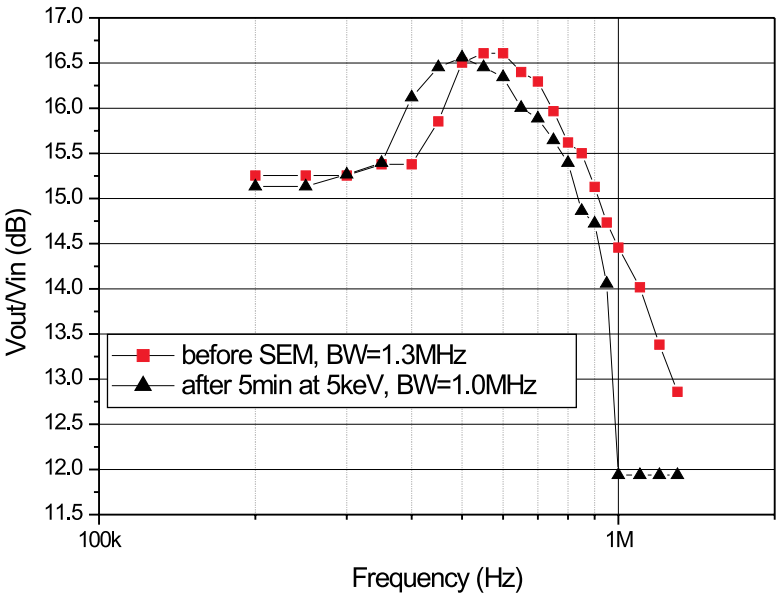

Figure 5.20: The frequency response for a BS circuit. Before SEM radiation the BW of the circuit is 1.3MHz and after 5minutes at 5keV radiation the BW drops to 1.0Mz).

stiffness of the cantilever, which will increase the mechanical stability of the cantilever. The surface roughness was also investigated and found that by decreasing the LPCVD deposition temperature to 580^0C, the surface roughness can be decreased to approximately 30nm p-p.

Then the general process sequence of fabricating the poly-Si cantilevers on the CMOS was presented. The mask definition of the cantilever was performed by laser, E-beam and AFM lithography. Both laser and E-beam have been successfully used to fabricate released structures, whereas AFM lithography could not be used due to the large poly0 surface roughness. The laser defined cantilever tend to been very porous with many pinholes and poorly defined side-walls, while the EBL defined cantilevers are pinhole free with very sharp defined side-walls. Furthermore, the cantilever widths achieved with laser lithography and EBL were down to 700nm and 300nm respectively.

One of the main challenges of the cantilever fabrication is stiction of the cantilevers with the bottom Si substrate during the release of the cantilever. Two dry release methods have been investigated namely freeze-drying and resist coating. It was found that resist coating gave the best reproducibility and also serves

as a temporary packaging of the chip.

Finally, processing effects on the CMOS circuitry have been investigated. It seems that the only post processing procedure that irreversibly damages the CMOS is the E-beam lithography. Solutions to this problem are currently being investigated.

Chapter 6

Non Integrated Cantilevers

In this chapter cantilevers that have not been integrated with CMOS circuitry are presented. As stated in the introduction, the final cantilever demonstrator will have a width of 100nm and thus new lithography methods and structural materials are being investigated. In this chapter the fabrication of AFM lithography defined Si cantilevers and UV lithography defined metal cantilevers will be presented. As mentioned in the introduction EBL and AFM lithography are competing technologies for the fabrication of the cantilever and it has been seen, in section 5.6.2 that EBL inflicts severe damage to the CMOS circuitry. On the other hand EBL has a higher throughput and reproducibility at this stage. Also, in this chapter, UV contact mask lithography is used to define metal cantilevers, which have a width down to 400nm, which proves that this technology is also a contender, since the throughput is much higher than for both EBL and AFM lithography.

6.1 AFM defined Si cantilevers

6.1.1 Process sequence

The process sequence for the fabrication of AFM defined cantilevers is seen in figure 6.1. The substrate consist of a Si on SiO_2 on Si structure as seen in figure 6.1a. The top structural layer can be poly-Si or single crystal Si if a silicon on insulator (SOI) substrate is used. A thin 7-10nm Al layer is deposited directly on the Si surface, figure 6.1b. A thin spacer SiO_2 layer can be added between the Si and Al layer, if laser lithography is needed. Then the AFM is used to locally oxidize the Al surface and the cantilever/electrode pattern is directly written, figure 6.1c. The development of the mask is the same as for the laser annealed mask, where the un-oxidized Al is etched away in a wet chemical etch, figure 6.1d. The structural layer is then patterned by RIE, figure 6.1e. Finally, the SiO_2 is etched and a dry release technique is performed in order to release the cantilever,

figure 6.1f.

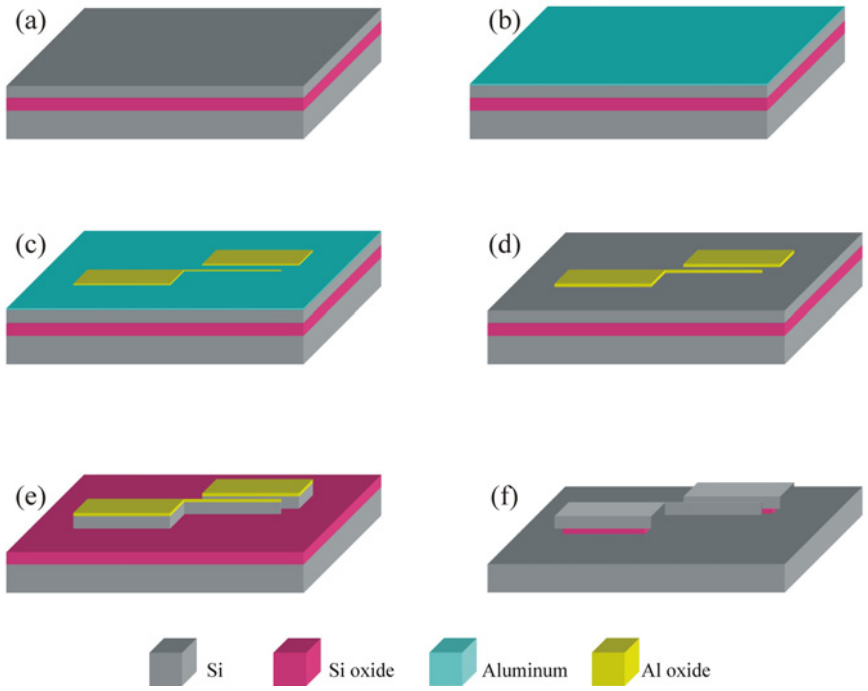

Figure 6.1: Process sequence of fabricating cantilevers with AFM. The fabrication starts with a $Si/SiO_2/Si$ substrate (a). First, a thin Al layer is deposited on the substrate (b). Then AFM lithography is used to oxidize locally the cantilever mask (c) and this mask is developed by wet etching the Al (d). The top Si layer is defined by RIE (d) and the structure is released by wet SiO_2 etching (f).

6.1.2 Local oxidation with AFM

AFM lithography is inherently a simple resistless and low cost technique for rapid prototyping. Previous works on AFM oxidation lithography on Al coated surfaces have mainly used contact mode AFM [90][113] for pattern generation. In contact mode tip wear is a critical problem because the electrostatic forces between the tip and sample are quite large, typically on the order of 100-1000nN for tip-sample voltages on the order of 10-20V. This increases the tip-sample interaction dramatically, because the spring constant of contact mode AFM probes is much lower than that of non-contact AFM probes. Furthermore, due to friction between the conducting tip and the Al, which has a thin insulating native oxide layer, electrostatic effects make it difficult to control the tip-sample distance and thus

the oxidation is non-reproducible. In order to remedy the problems encountered with static mode AFM, other AFM modes have been used [114][96][97][99][115].

Jumping mode AFM

Jumping mode AFM is performed by vibrating either the sample stage or the cantilever at a frequency below the resonant frequency of the cantilever. At each vibration the cantilever contacts the surface and a force curve is used to measure the height of the surface or the adhesion to the surface [116][117]. In figure 6.2 a typical cantilever displacement versus tip/sample distance curve is shown. The sample height is measured at point A, where the AFM tip makes first contact with the surface. The adhesion between the tip and sample can also be measured by the difference between point A and B, where B is the point where snap-off the tip snap-off from the surface.

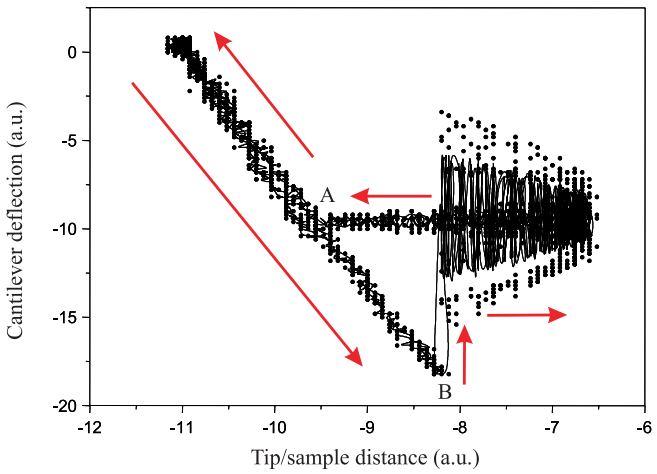

Figure 6.2: Cantilever displacement versus tip/sample distance curve, which illustrates jumping mode AFM. Point A denotes the first contact point and point B denotes the snap-off point.

Jumping mode AFM has the advantage of less tip wear during scanning and less friction between the tip and sample, thus electrostatic effects experienced in contact mode are avoided. Furthermore, jumping mode AFM has also been used for local oxidation of Al [114]. By measuring the adhesion forces, alignment of the AFM with different types of surfaces, that do not necessarily have a height contrast, can be performed. An example of this is seen in figure 6.3. The surface is a laser annealed Al pattern on an oxidized poly-Si surface, which has a large roughness, thus the height contrast between the laser annealed Al and the underlying SiO_2 is very low as seen in figure 6.3a. In figure 6.3b the adhesion mode image shows a better contrast, which is then increased by applying a volt-

age to the laser annealed Al, figure 6.3c. The increase in contrast is due to an added electrostatic force between the laser annealed Al and the tip, which are both conducting. In figure 6.3d the force curve of the cantilever at 0V and 20V is seen, which illustrates the increase in adhesion. Furthermore, the oxidized lines are clearly seen. The lines are darker than the laser annealed mask, which is a good indication that oxidation has occurred, since the adhesion forces should be reduced on Al-oxide.

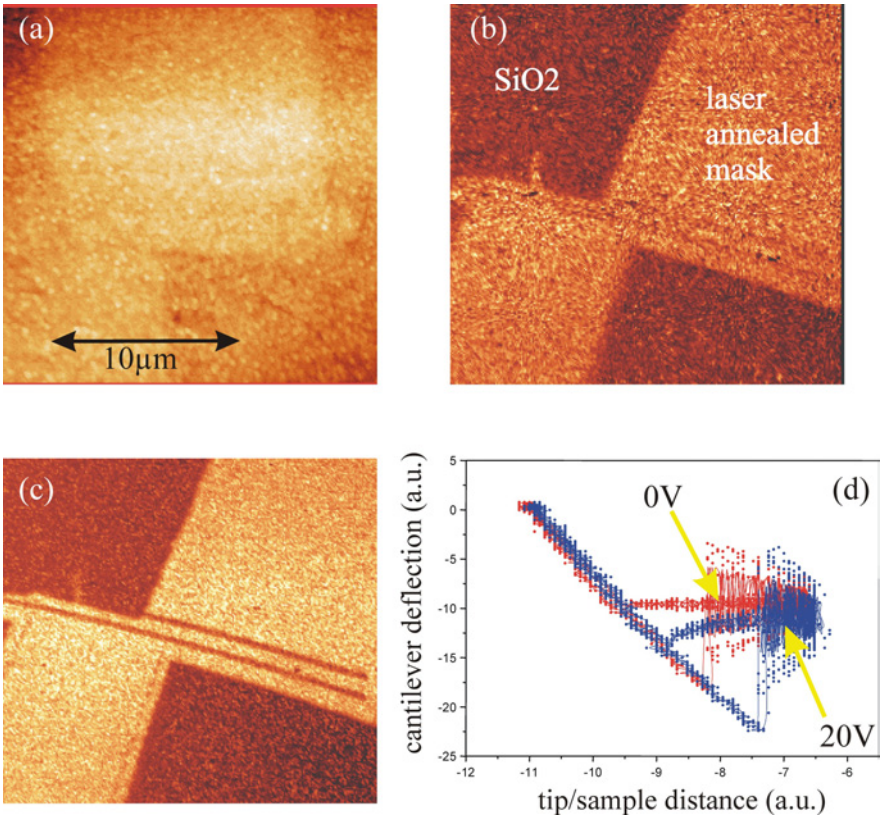

Figure 6.3: AFM images using (a) contact mode and (b) and (c) adhesion jumping mode AFM. The contrast is increased from (b) to (c) by applying 20V, which increases the electrostatic adhesion.

Non-contact mode AFM

It has also been seen that optimization of the AFM lithography technique, by using non-contact mode AFM (nc-AFM), can increase its reliability and reproducibility [96][97][99]. In nc-AFM mode, the tip-surface interactions are reduced even more than in jumping mode because there is no contact between the tip and surface, whereas in jumping mode there is contact at each pixel point. This further increases the tip lifetime and thus the reproducibility of the technique.

As with jumping mode, the problems experienced with contact mode are not present. Due to the low interaction forces between tip and sample, tip wear is minimized. Furthermore, since friction is eliminated, the tip-sample distance can be controlled very precisely.

In order to use AFM lithography for the fabrication of NEMS structures, it is necessary not only to be able to write features with sub-micron dimension, but also to connect larger contact pads. Therefore, it is advantageous to optimize the lithography for defining small as well as larger features in the same writing process. This can be obtained with nc-AFM lithography. In nc-AFM lithography the tip-sample distance can be controlled by monitoring the modulation in the oscillation amplitude of the AFM cantilever [118] [119]. Earlier non-contact AFM lithography experiments on Si have shown that a water bridge is formed between the conductive tip and sample and that the geometry of the water bridge influences the final oxide dimensions[96][97][99]. The formation of the water bridge is observed by monitoring the cantilever's oscillation amplitude after pulsing with a DC voltage between the tip and sample, while simultaneously disconnecting the feedback loop. After the voltage pulse the oscillation amplitude is lower than the feedback set point, due to the extra forces acting on the tip due to the formation of the water bridge.

The same behavior was observed on Al coated substrates. During writing the feature size of an oxidized line can be controlled by simply controlling the tip-sample distance and the applied DC voltage. By stretching the water bridge the feature size decreases. By decreasing the tip-sample distance, the water bridge covers a larger area on the Al surface, thus the feature size increases. In contact mode AFM lithography on Al the sudden application of high voltages invokes breakthrough of the thin natural Al-oxide and the surface is destroyed. This breakthrough phenomenon is not observed in non-contact mode AFM lithography. Thus higher voltages can be applied, which increases even further the obtainable feature sizes. In figure 6.4 a schematic drawing and two AFM images show how one can vary the feature size from almost 1μm (figure 6.4a) down to 100nm (figure 6.4b) by controlling the water bridge.

By optimizing the AFM writing, large areas can be written in a matter of minutes, when a tip/sample distance of approximately 3-5nm and a high DC voltage of 30V or more are chosen. The details of the pattern are written by optimizing the AFM lithography with a larger tip/sample distance of approximately 8-10nm and a DC voltage of 20V. The scan speed is usually kept constant at approximately 10μm/sec. Figure 6.5a shows an example of a device with two oxidized 2x3μm^2 areas and a very thin, 50nm wide, line extending from one of the 2x3μm^2 areas. The 50nm wide line is separated from the other 2x3μm^2 area by a 500nm gap. Figure 6.5b shows a profile of the Al-oxide pattern showing a

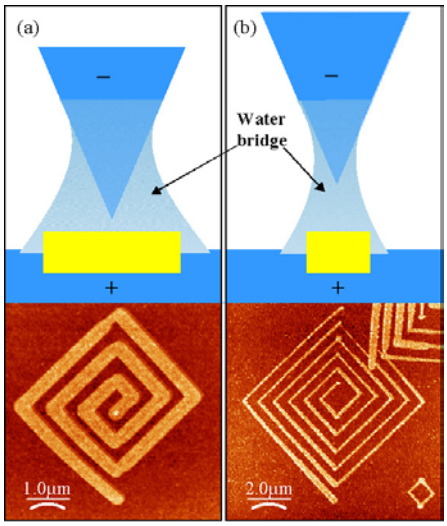

Figure 6.4: In (a) the tip-sample distance is small (3-5nm) resulting in a wide waterbridge cross section, whereas in (b) the tip-sample distance is increased (8-10nm), which decreases the waterbridge cross section

height of 3.5nm, which corresponds to an oxidation of the entire 7nm Al thickness.

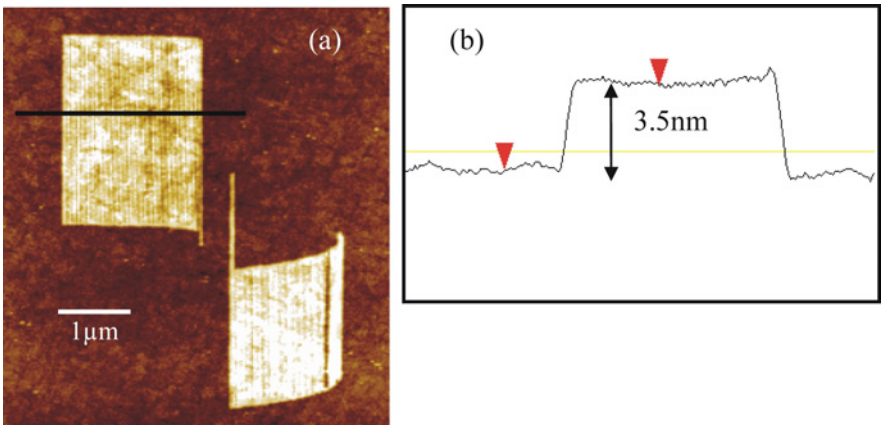

Figure 6.5: (a) Non-contact AFM image of the Al-oxide structure written by local oxidation just after the oxidation. (b) the height of the oxide is measured to 3.5nm, corresponding to approximately half the Al thickness.

In figure 6.6 two AFM images of approximately 10nm wide Al-oxide lines are shown, illustrating that by optimizing the lithography parameters very small feature sizes can be reproducibly obtained. Due to tip convolution the actual width of the oxidized lines could be smaller than 10nm, but this cannot be seen due to the finite tip sharpness of the AFM tip. It can also be seen in the images

that the width of the oxide lines vary by approximately 3nm, which is due to the small sample roughness, which varies the tip/sample distance slightly. Also seen on the right image of figure 6.6, some high protrusions appear. These protrusions are due to momentary halts in the scanning while oxidizing the lines, caused by software errors.

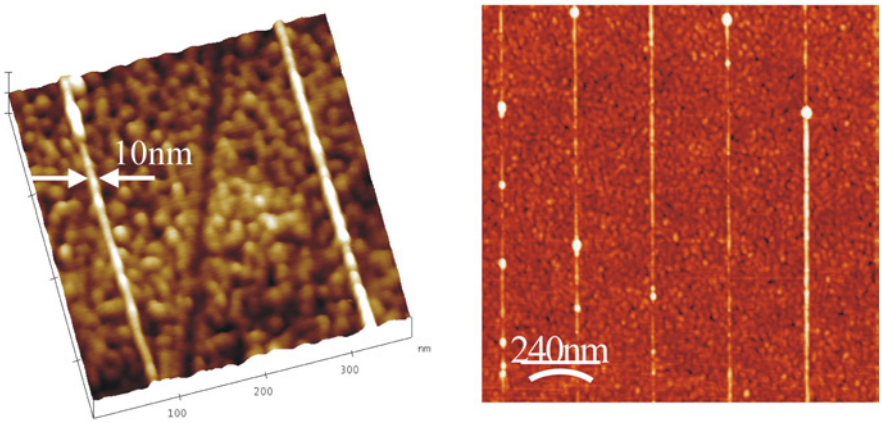

Figure 6.6: Non-contact images of 10nm wide Al-oxide lines, which have been achieved by optimizing the writing parameters.

6.1.3 Fabrication results

Jumping mode AFM results

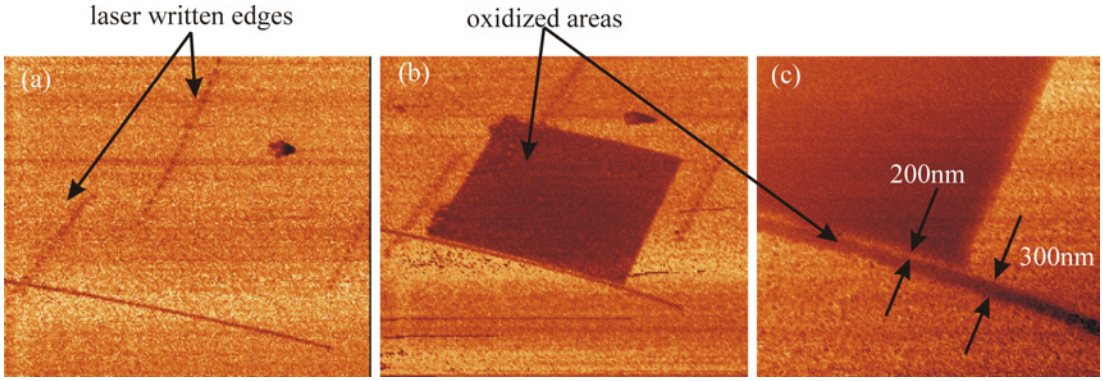

Figure 6.7: (a) adhesion mode image of the laser annealed Al before etching the Al, where the dark dots correspond to the edges of the laser written area. AFM images after the cantilever (a) and the driver (b) are defined. In (c) a close-up of the cantilever/electrode pattern is seen.

The first attempt at fabricating structures were with jumping mode AFM and were performed on a Al/SiO_2/poly-Si/SiO_2/Si substrate with layer thicknesses of, 7nm, 100nm, 2μm, 4.5μm and 525μm respectively. Due to the slow writing speed of the AFM lithography electrodes were first written with laser lithography. Without development of the pattern the sample was transferred to the AFM setup and the AFM was aligned to the laser annealed Al by using the adhesion force mode, where the edges of the laser annealed mask can be seen due to a local Al evaporation during laser writing, see figure 6.7a. Then the cantilever and driver are defined with the AFM. The patterns are easily seen as the dark areas in the adhesion mode images, figure 6.7a and b. Figure 6.7c shows a close-up of the cantilever/electrode Al-oxide mask. The cantilever is approximately 300nm wide and the gap is approximatively 200nm wide. After this the laser-annealed/AFM-oxidized mask is developed by wet chemical etching of the unexposed Al and the resulting structure is transferred by RIE to the poly-Si layer. Finally, the device is released in BHF and dried in N_2 gas. A SEM image of the final structure is seen in figure 6.8. It can be clearly seen where the laser and AFM defined masks have protected and where the two overlap, by the surface roughness of the poly-Si. Unfortunately this cantilever broke, due to underetching of the poly-Si structural layer during the RIE.

The drawback of jumping mode lithography is the inability to obtain reproducible low line-widths. Since there is full contact between the tip and sample at each pixel point, the minimum line-width is very dependent upon the AFM tip radius and shape. Furthermore, since there is a wear of the tip, the tip quality deteriorates over time, thus even the best line-widths only last for a finite amount of time.

Nc-AFM results

In order to increase control of the line-width a SOI (SOI-TEC with buried oxide) substrate was used for the nc-AFM lithography experiments. The SOI substrate has a very low surface roughness of approximately 3-5nm p-p compared to approximately 30nm p-p for the poly-Si. The thicknesses of the top Si layer and the buried SiO_2 are 350nm and 450nm respectively. As before, in order to access the small AFM defined electrodes, larger wiring and contact pads were defined by laser lithography. This time the AFM structures are defined first then the laser defined wires and pads are written afterwards. As seen in figure 6.9a the AFM oxidized areas are clearly seen with an optical microscope and thus the laser is easily aligned to the AFM written areas. Figure 6.9b shows an optical image of the laser and AFM structure after Al wet etching, illustrating that the alignment of the laser onto the Al-oxide mask is possible. Figure 6.10 shows SEM images of the structure after RIE. Figure 6.10a shows the whole device with 50x100μm^2 bonding pads, 100μm long wires and the finer AFM defined structures. In figure

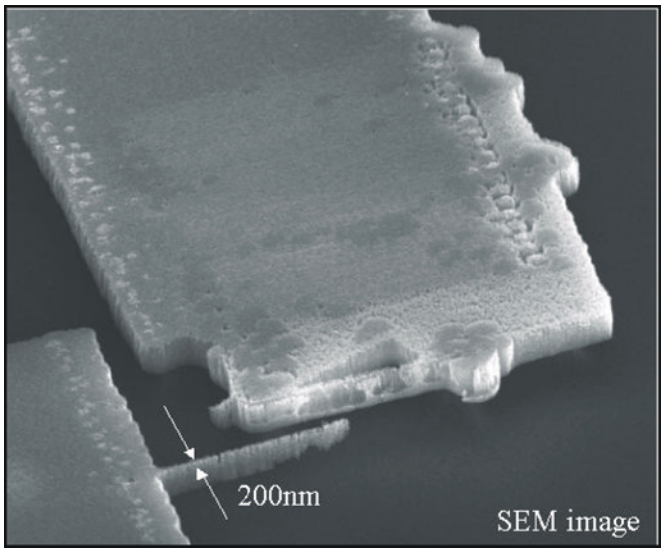

Figure 6.8: SEM image of the poly-Si cantilever, which has been patterned by jumping mode AFM lithography. The width of the cantilever is 200nm and the gap is approximately 500nm.

6.10c the Al-oxide mask is seen to overhang the slightly underetched Si structure. In figures 6.10b and d close-ups, showing the laser-AFM interface are shown.

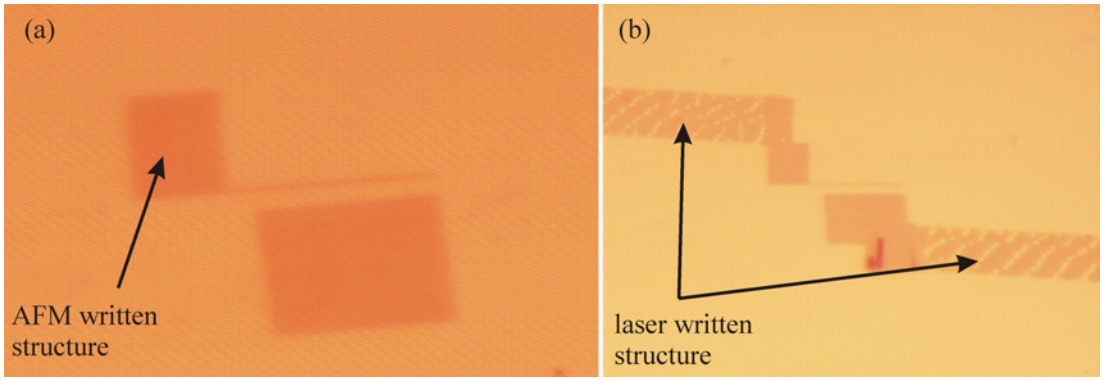

Figure 6.9: Optical images of (a) the AFM written structure just after AFM oxidation and (b) the same AFM written structure plus the laser written wires after Al etching.

In figure 6.11 SEM images after underetching are shown. The dimensions of the cantilever are 150nm, 350nm and 10μm for the width, height and length respectively. After underetching the resist dry release method was used, as described in section 5.4.2 . As can be seen in the images, the tip of the cantilever is touching the substrate, which probably occurred after releasing the cantilever since only

the end of the cantilever is sticking. Attempts of unsticking the cantilever failed, thus no mechanical characterization of this cantilever was possible.

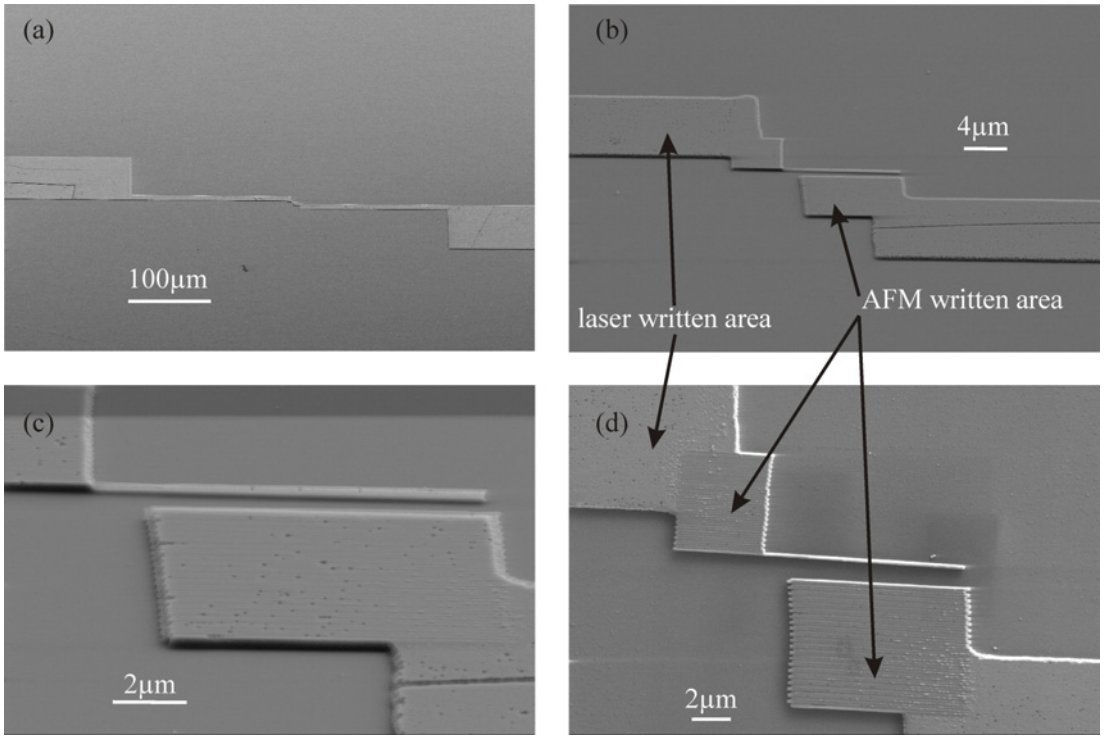

Figure 6.10: SEM images of (a) the whole laser and AFM defined device after RIE etching, (b)-(d) close up images of the AFM defined area. Note that in (d) the Al-oxide mask is clearly seen compared to the laser mask.

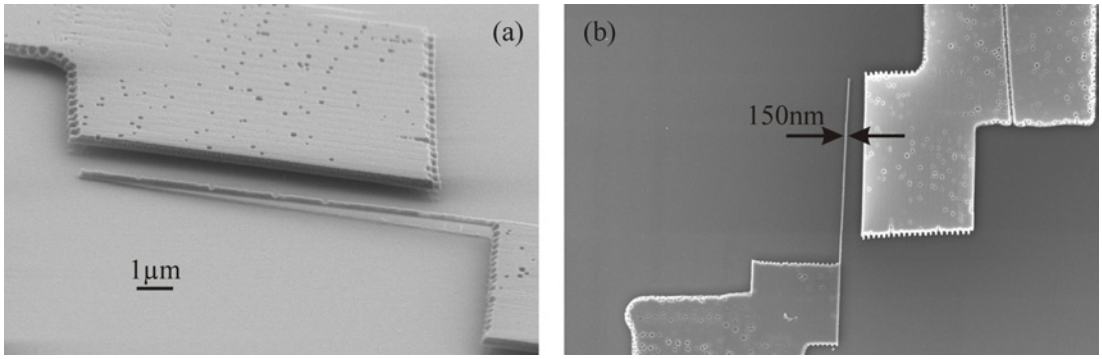

Figure 6.11: SEM images of the AFM/laser defined device after underetching. The tilted view (a) shows that the cantilever is sticking to the substrate at the end of the cantilever and in the top view (b) it was measured that the width of the cantilever is 150nm.

6.2 Metal cantilevers

Another approach to fabricate small cantilevers is to use a structural material other than Si. So far, the ideal properties of the structural layer of the cantilever have been defined as (1) good electrical conductivity, (2) good elastic properties and (3) a low density. So, by comparing the theoretical mass sensitivity for cantilevers with the same dimensions using equation 2.1-9, for different cantilever materials, it is seen that Si yields the best sensitivity. In table 6.1 the theoretical mass sensitivity for several materials are compared. The spring constant, resonant frequency and minimal detectable mass are calculated using equations 2.1-2, 2.1-7 and 2.1-9 respectively and the cantilevers are 500nm wide, 1μm high and 30μm long. As expected single crystal-Si and poly-Si have the best mass sensitivity, but Al has a minimum detectable mass change that is only twice as large as that for single crystal-Si.

material	E (GPa)	ρ (g/cm^3)	k (N/m)	f (kHz)	$\frac{\Delta m}{\Delta f}(g/Hz)\cdot 10^{-16}$
Si	180	2.33	0.414	787	0.178
poly-Si	160	2.33	0.370	744	0.188
Al	74	2.70	0.171	470	0.345
Ti	110	4.51	0.255	443	0.611
Cr	140	7.19	0.370	423	1.019
Ni	200	8.9	0.463	435	1.255
Au	80	19.3	0.185	183	6.388

Table 6.1: The calculated spring constant, resonant frequency and minimum detectable mass for different cantilever material, with the same dimensions of 500nm, 1μm and 30μm for the width, height and length respectively

By looking at the device as a whole, the cantilever must be excited into resonance in order to detect the vibration. This means that making the cantilever very short, which would increase the mass resolution, is not a viable design. In table 6.2 the minimum detectable mass change is calculated again, but this time, the spring constant of each cantilever is kept constant along with the width and height, and the length is adjusted. By isolating the length in equation 2.1-2 and inserting into equation 2.1-5, it is seen that the resonant frequency can be increased by decreasing both the Young's modulus and the density of the cantilever material.

$$f = \frac{C_n}{4\sqrt{3}\pi}\frac{k^{2/3}}{\rho^{1/2}E^{2/3}t^{2/3}w^{5/6}} \tag{6.2-1}$$

By looking at table 6.2 it is seen that Al has the best mass resolution followed by poly-Si and then single crystal Si. This is because Al has both a low density and low Young's modulus compared to the other cantilever materials. In conclusion, the choice cantilever material is one with a low density and low Young's modu-

lus, since the frequency can be increased by simply decreasing the length of the cantilever. Among these materials Al is the best choice.

material	E (GPa)	ρ (g/cm^3)	l (μm)	f (kHz)	$\frac{\Delta m}{\Delta f}(g/Hz) \cdot 10^{-16}$
Al	74	2.70	16.67	1523	0.591
poly-Si	160	2.33	21.54	1442	0.696
Si	180	2.33	22.37	1415	0.736
Ti	110	4.51	19.01	1103	1.555
Cr	140	7.19	20.61	839	3.531
Ni	200	8.9	23.21	711	5.811
Au	80	19.3	17.10	562	11.740

Table 6.2: The calculated length, resonant frequency and minimum detectable mass for different cantilever materials. The cantilevers have a spring constant of 1N/m, a width of 500nm and a height of 1μm.

6.2.1 Fabrication process

As stated in section 1.4 of the introduction, the first phase of WP3 is to fabricate a metal cantilever that has a width below 500nm without CMOS. In order to realize this contact mask UV lithography was chosen because 500nm feature sizes should be obtainable according to equation 3.1-1 if the wavelength and resist thickness are optimized. In order to achieve this, the structures on the contact mask must be well defined and with the feature sizes that are desired. For this purpose the UV mask was fabricated using EBL, where line-widths down to 300nm were defined on the mask.

In figure 6.12 the fabrication process of Al cantilevers is shown, which is based on a lift-off technique. The process starts by defining a resist mold structure on a Si substrate using UV lithography, figure 6.12b. Then, Al is deposited using an evaporation technique, figure 6.12c. This is followed by lifting off the Al deposited on the resist, figure 6.12d. Finally, the metal structure is released by dry etching the underlying Si, figure 6.12e. In order to be able to break individual chips from the wafer, a second thick resist is spun and defined on the front side. This thick resist acts as a protection mask for deep reactive ion etching (DRIE), which can etch vertical groves through the wafer, but in this case only 100-200μm is required, so that the individual chips can be separated from each other.

There are several advantages of this fabrication process. First, it is a batch process, where a whole wafer of devices can be patterned at one time. Second, the release step is a dry etching step, thus stiction is not an issue. Finally, all these processing steps are CMOS compatible, thus the process sequence can be transferred to CMOS circuitry.

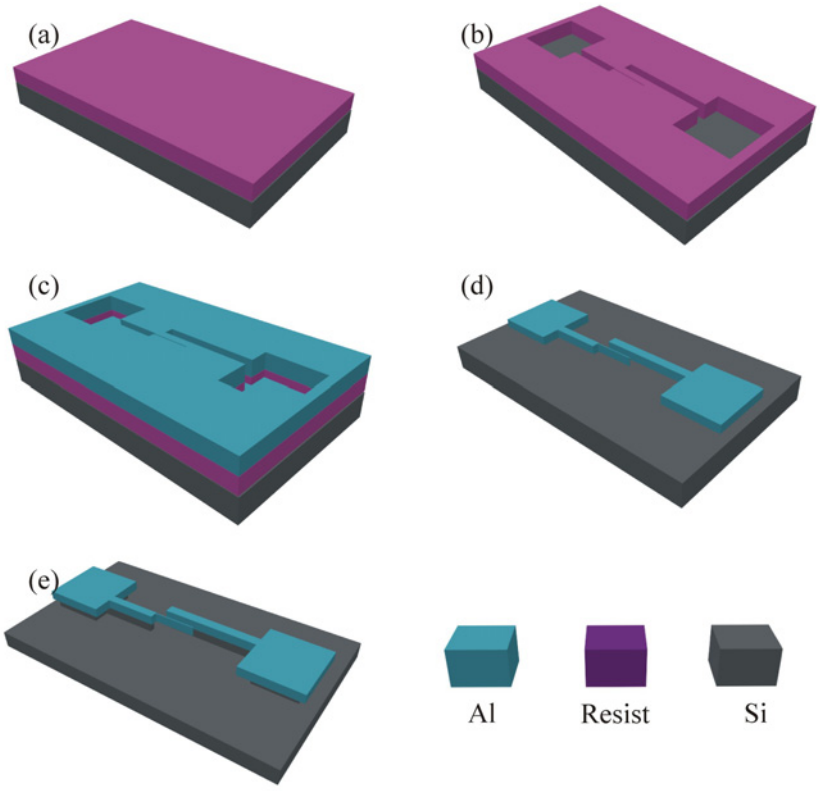

Figure 6.12: Process sequence of fabrication of Al cantilevers using UV lithography. The process starts by spinning a 600nm thick resist on a Si substrate (a). Then the resist is pattered by a negative lithography setup in (b). Al is then deposited on the substrate (c)and lift-off of the resist layer (d) defines the Al structures. Finally, in (e), the Al structures are underetched by isotropic RIE.

UV lithography

The most critical step of this process is the definition of the resist mold. The ideal mold is one that has a high aspect ratio and a very narrow width, so that the cantilever can have a good aspect ratio and still be able to be used for lift-off. On the other hand the line-width is dependant on the resist thickness, thus a thin resist thickness is desirable. As a first attempt of solving this, a two layer resist system has been attempted. First, a commercially bought LOR (lift-off resist) is spun onto the substrate at a thickness of 0.5-1μm and subsequently baked. Then, a thin AZ5214E resist is spun at a thickness of approximately 600nm. In order to achieve sub-micron lithography the AZ5314E is used in a negative process [120], which is said to have higher resolution due to reduced proximity effects. Due to lack of time and reproducibility problems with this resist no fabrication results where obtained. Further details about LOR resist can be found elsewhere [121].

The reverse process with AZ5214 resist is as follows: In AZ5214E a catalyst is formed upon exposure, which promotes cross-linking during any later heat-treatment. After a post annealing, the whole wafer is exposed (so called "flood" exposure) and the unexposed areas from the first exposure are made soluble to the developed, whereas the exposed area do not become soluble since this resist contains no more photoactive compound (PAC).

Mask design

An individual chip layout is seen in figure 6.13a and b where one and two electrode devices have been designed. Several chips have been designed with different gap sizes and cantilever widths. The gap size ranges from 500nm up to 1000nm and the width ranges from 300nm up to 1000nm. Furthermore, each chip has 32 and 21 devices, for the 1 and 2 electrode design respectively, where the length of the cantilever is varied on the individual chips according to the width and gap of the cantilever.

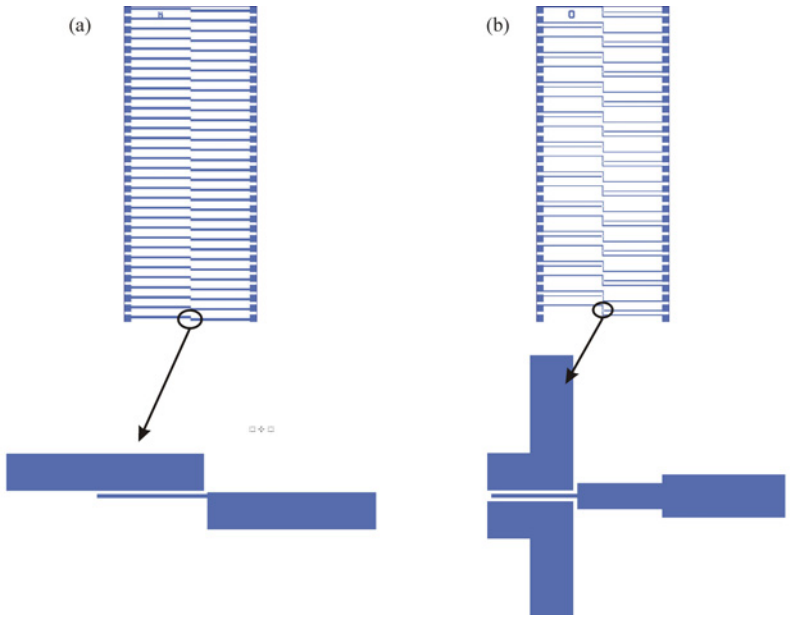

Figure 6.13: Metal mask for the (a) one electrode chips and (b) the two electrode chips.

6.2.2 1st generation metal cantilevers

In the 1st generation the LOR resist layer is not included, but only the AZ5214E is used. This is because it was thought that the thin resist process should be proven before complicating the process with extra resist layers. In figure 6.14a

and b optical images of the resist mold and the Al structure after deposition of 100nm Al and lift-off are shown. In figure 6.15 SEM images of the Al structures are seen both before (a) and after, (b)-(c), isotropic RIE of the underlying Si. It is seen that the smallest width achieved was approximately 400nm, which is below the 500nm goal. Furthermore, the structure of the cantilevers have well defined edges.

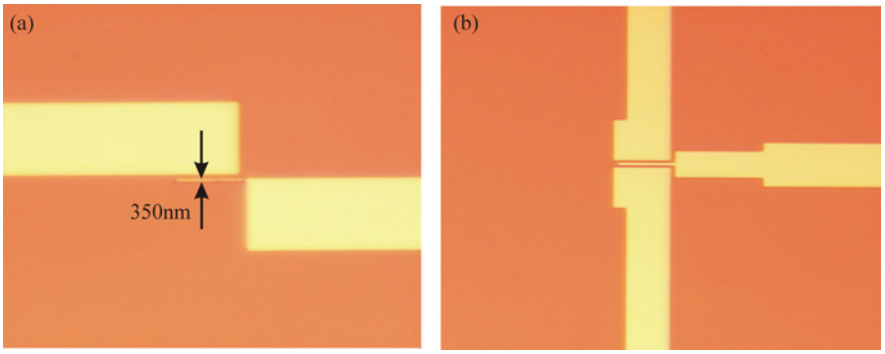

Figure 6.14: Optical images of the 100nm thick Al structure just after lift-off, showing the (a) one electrode and (b) two electrode design.

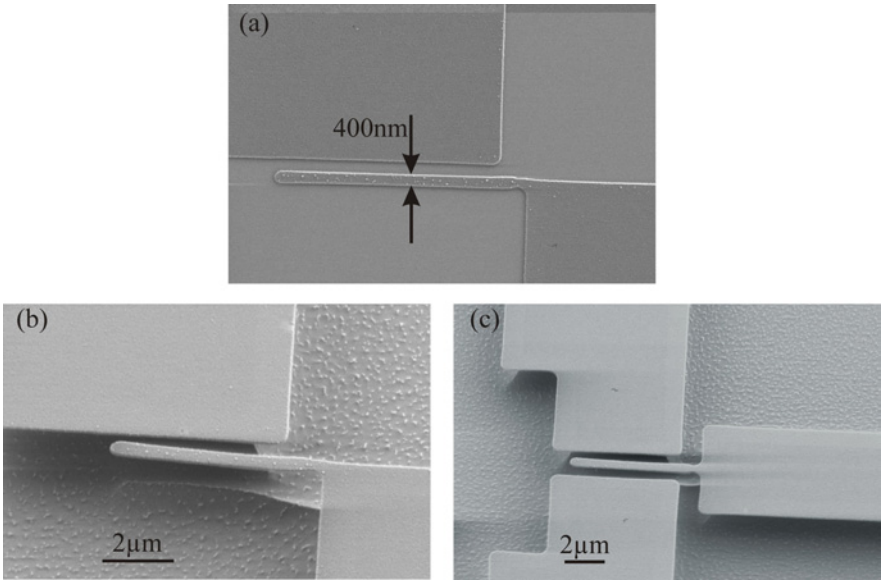

Figure 6.15: SEM images of the Al structure (a) before underetching and (b)-(c) after underetching.

6.2.3 Future generation metal cantilevers

In order to increase the height of the Al cantilevers several techniques can be used. The first, which has been mentioned, is the use of an extra resist layer like LOR. Another method is to use a resist/metal/resist layer. The idea is that the top resist layer is thin and is used for the UV lithography process, as described above. Then, the top resist is used to selectively etch the metal. The metal acts as a etch mask for the lower thicker resist level in an O_2 plasma etch, which should define vertical side walls. Finally, the metal is removed and the resist mold can be used to fabricate the metal cantilevers. This technique, along with the LOR technique, are currently being investigated in the NANOMASS project.

6.2.4 CMOS integration

As stated in section 5.3 contact mask UV lithography was not attempted because of the large separation of the mask and nanoarea surface, due to the passivation layer. This separation cannot be avoided with contact mask lithography. In order to use UV lithography on CMOS either projection lithography or a light coupled mask (LCM) could be used [122][123]. Since most CMOS fabs use projection lithography, this could be a straight forward way of defining cantilever. In LCM mask UV lithography the contact mask is structured so that protrusions on the mask surface have contact with the surface. In this way in the protrusions could fit into the nanoarea and contact between the mask and surface can obtained. By using LCM feature sizes down to 100nm have been obtained on flat surface [124].

6.3 Summary

In this chapter cantilevers that are not integrated with CMOS have been presented. The objective of these cantilevers is to demonstrate the feasibility of fabricating cantilevers with widths down to 100nm, and to demonstrate the feasibility of fabricating cantilevers with other materials other than Si.

It was found that AFM lithography has the ability to achieve line-widths below 100nm, down to 10nm, which is difficult with other lithography methods such as EBL. Furthermore, the fabrication of a 150nm wide cantilever has been demonstrated on an SOI substrate, which is the first step of achieving the NANOMASS main goal. It was shown that nc-AFM lithography is a highly flexible technique, which has a high reproducibility. Furthermore, the speed can been increased by varying the tip-sample distance, thus increasing the throughput of the technique. Further investigation and optimization of this point are currently being pursued.

The mass sensitivity of a cantilever based mass sensor was shown to be larger for Al than for Si because the overall mass of the sensor is less for a cantilever with the same spring constant. It was also demonstrated that cantilever widths down to 400nm can be realized with contact mask lithography. This offers a high throughput technique, which has the potential to define sub-micrometer wide cantilevers. The cantilevers that have been fabricated were only 100nm high, which could have the potential of being vertically vibrating mass sensors. In the next chapter it will be shown that vertical electrostatic excitation of these structures is possible even with a lateral driver electrode.

Chapter 7

Characterization

In this chapter three types of cantilevers are characterized.

1. Poly-Si cantilevers not integrated with CMOS
2. Poly-Si cantilevers integrated with CMOS
3. Al cantilevers not integrated with CMOS

In order to characterize the devices three characterization techniques have been used besides the electrical capacitive readout.

7.1 Non-electrical characterization methods

In this section the different types of non-electrical characterization techniques will be presented. Since the electrical characterization is the main challenge, other characterization techniques were used to evaluate the cantilever's performance. These techniques can be used to compare with the model performance and to help design the CMOS integrated device. The three different methods used have been visual, SEM and AFM characterization.

7.1.1 Visual characterization

The schematic of the visual characterization setup can be seen in figure 7.1. The setup comprises of a microscope, a CCD camera and a probe station. The chip is accessed either with single probes, a probecard or by wire bonding the chip to a chip holder. The device can then be monitored with the optical microscope while the cantilever is statically bended or put into resonance. Furthermore, this setup can be used for the characterization of the CMOS integrated devices, so that the lateral vibration can be monitored with the microscope at the same time as the electrical characterization is being performed. The accuracy of the measurements is around 200nm by using special software to measure the single pixels in the CCD image.

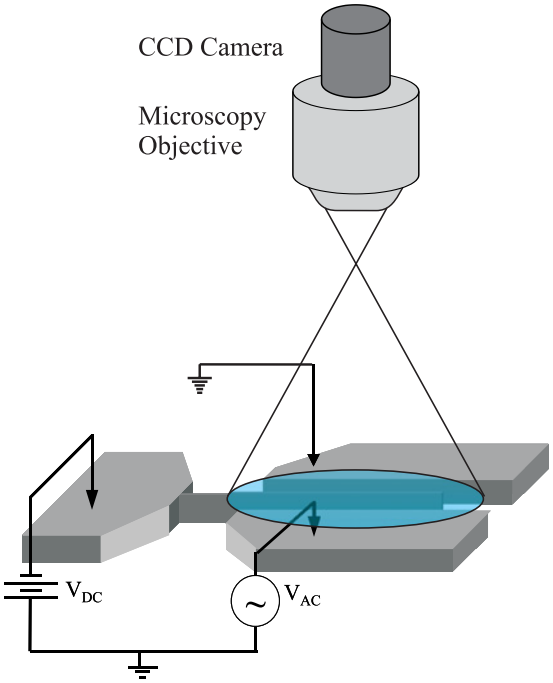

Figure 7.1: Schematic drawing of the visual characterization setup used to characterize cantilevers in air. An optical microscope is used to monitor the cantilever while applying voltages.

7.1.2 SEM characterization

In order to characterize the performance of the cantilever in vacuum and still monitor the bending and vibration of the cantilever, the device is placed in a SEM. The schematic of this setup is seen in figure 7.2. In order to get electrical contact to the device, electrical leads were installed on the front door of the SEM. The chip is wire bonded to a ceramic chipcarrier, which is then placed on the SEM stage with a specially made holder, figure 7.3. Due to the increased imaging resolution of the SEM compared to optical microscopy, the cantilever displacement can be measured with an accuracy of approximately 10nm. Finally, the bending of the cantilever has can be measured directly by focussing the E-beam on the cantilever and monitoring the secondary electron detector signal [125][126][127].

7.1.3 AFM characterization

In order to have a high accuracy characterization of the cantilever in air, AFM imaging of the device can also be used. The AFM characterization setup can be seen in figure 7.4. The cantilever device is wire bonded to a chipcarrier and placed on the stage of the AFM. The microscope used was a Nanoscope IV,

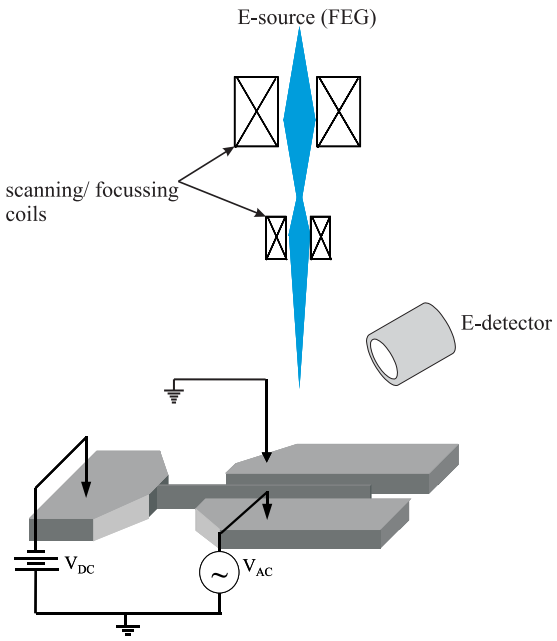

Figure 7.2: Schematic drawing of the SEM characterization setup used to characterize cantilevers in vacuum. The sensor chip is placed in a SEM with electrical leads to the outside so that actuation of the cantilever is possible.

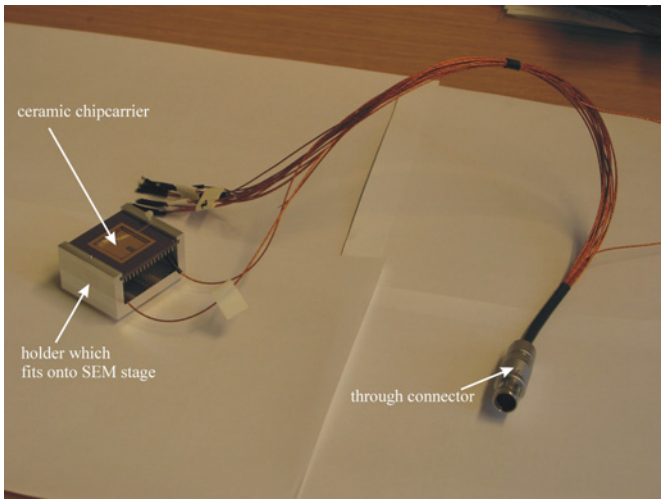

Figure 7.3: Image of the ceramic chipcarrier, holder and cables, which are used inside the SEM

which is configured so that the AFM tip is scanning over the surface. In order to minimize the forces exerted on the cantilever by the AFM tip, non-contact mode was used. To measure the bending in real-time the slow-scan of the AFM is switched off, so that the AFM is only scanning one line across the cantilever.

Then the cantilever's displacement is measured by monitoring the line-scan. The resolution of measuring the displacement of the cantilever is approximately 5nm. The AFM setup can also be used to exert forces on the cantilever, which can be used to characterize the force sensitivity of the sensor. Finally, the AFM can be used to un-stick the cantilever from the bottom substrate or from the parallel electrode, by using the AFM tip to push the cantilever with a controlled force.

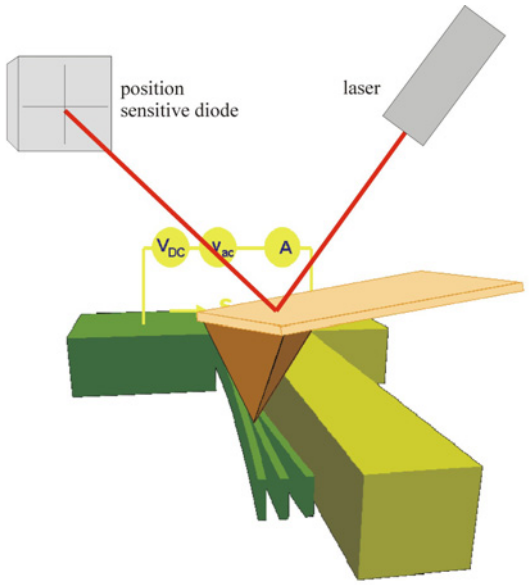

Figure 7.4: Schematic drawing of the AFM characterization setup used to characterize cantilevers in air. The AFM is used to image a constant line across the cantilever, which is used to measure the deflection amplitude.

7.2 Characterization of poly-Si cantilevers

The non-electrical characterization methods have been used to characterize non-CMOS integrated devices in order to compare the performance with the SPICE and SUGAR model. The cantilevers which have been characterized have been prepared using laser lithography on Al coated SiO_2/poly-Si/SiO_2/Si substrate with layer thickness 100nm/1.8μm/4.5μm/525μm respectively. The fabrication of the cantilevers is similar of that seen in figure 6.1 but the RIE etch mask is defined with laser lithography. A full description of the process sequence is described elsewhere [81][100]. SEM images of the final poly-Si cantilevers are shown in figure 7.5. These cantilevers have two electrodes so that one and two electrode measurements can be performed. In tables 7.1, 7.2 and 7.3, a list of the cantilevers that have been characterized can be seen along with the main findings

of each cantilever. The approximate width, height and length are 1μm, 1.8μm and 40μm respectively.

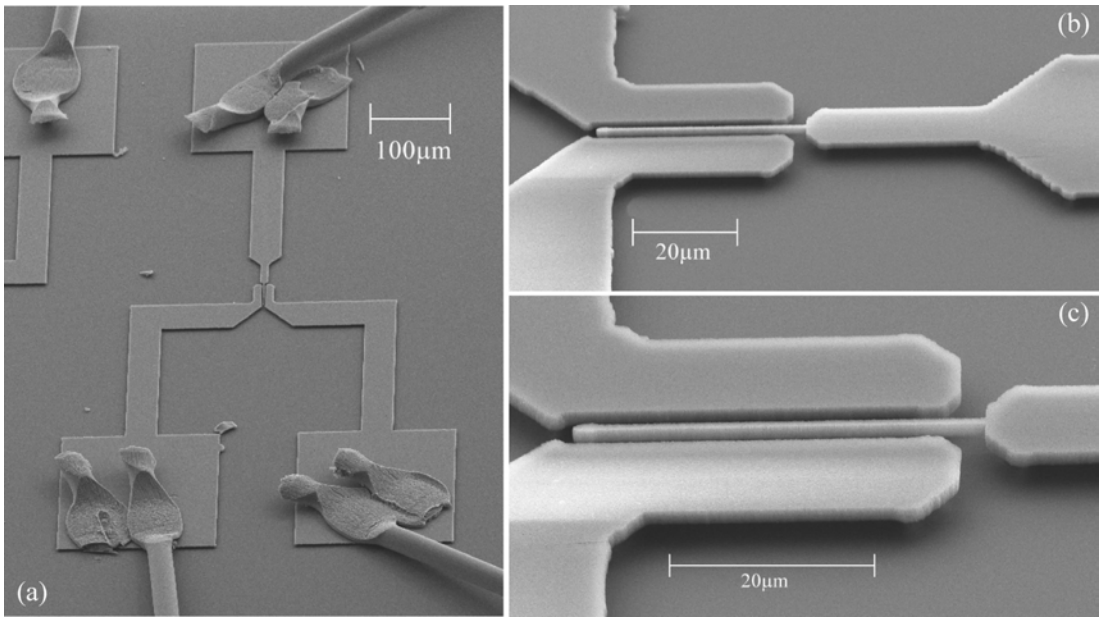

Figure 7.5: SEM images of poly-Si cantilevers defined by laser lithography. In (a) the entire device is shown and (b) and (c) close-up images of the device are shown. The cantilever is fully underetched while the electrodes are anchored to the substrate. The dimensions of this cantilever are 700nm, 1.8μm and 40μm for the width, height and length respectively.

The interesting aspects of the model that need to be treated here are (1) the acoustic damping effects on the cantilever and (2) the fringe factor. In addition to the acoustic damping, which occurs when operating the cantilever in air, the air molecules will either increase the effective mass of the cantilever or increase the effective spring constant of the cantilever due to air squeeze effects between the cantilever and parallel electrode [128][129]. By characterization of the cantilever in air, the effective mass can be determined and thus the type of damping can be determined. The fringe factor α can be determined by measuring the static response of the cantilever.

The measurements can be split into the static and the dynamic characterization. The static characterization consists of measuring the static bending of the cantilever at the apex as a function of an applied DC voltage. With this characterization the fringe factor α can be calculated using the SUGAR model. The dynamic characterization consists of two types of measurements; the frequency response and the resonant frequency versus the sum of the applied voltages squared. The

cantilever's frequency response is used to determine the Q-factor of the cantilever. The resonant frequency versus the sum of the applied voltages squared is used to determine f_0, which is the resonant frequency without any applied voltages, by making a linear fit and extrapolating the frequency at 0V. Then this value is used to calculate the effective density of the cantilever, where a Young's modulus of 160GPa is assumed. Finally, the SPICE model can be compared to the measurements, by using the α value and effective density.

7.2.1 Air measurements

Measurements in air have been performed by the visual characterization setup and the AFM characterization setup. In order to compare the measurements to the models, both static and dynamic frequency response measurements have been performed.

Static measurements

The first static characterization was performed with the visual characterization setup. Figure 7.6a an optical image of the cantilever shown. By counting the pixel points in the image a rough estimate of static bending at different applied voltages can be deduced. Figure 7.6b shows the static bending as a function of the applied DC voltage on one of the parallel electrodes, while the other electrode is grounded. The SUGAR simulations are plotted along with the data points where a fringe factor of 3.1, 3.73 and 4.1 are used to compare with the data points. Since the accuracy of the static bending measurement is low, the uncertainty of the actual fringe factor is approximately ± 0.5.

In order to perform a more accurate measurement the AFM characterization setup has used on a different cantilever device, device 2. In figure 7.7a an AFM image resulting from a line measurement is seen. The image is taken by first switching off the slow scan so that the same line is being repeatedly scanned. Then, a DC voltage is applied and subsequently set to zero, each time increasing the applied voltage. The displacement of the cantilever is then measured by measuring the distance of an artifact in the image at zero volts and at the applied voltage. In figure 7.7b the static bending as a function of the applied DC voltage is shown. The SUGAR simulation is also included using a fringe factor of 5.16, which fits the AFM data almost perfectly. Another SUGAR simulation is included showing the DC response of the cantilever at α=0. In this simulation the static bending is predicted to be 42nm, which is almost 4 times as small as the measured value. This confirms that fringing fields have a large contribution to the total capacitance in the system, where in this case the real capacitance is 6 times that of the parallel plate approximation. This seems like a very high value compared to the parallel plate approximation, which could be explained by two

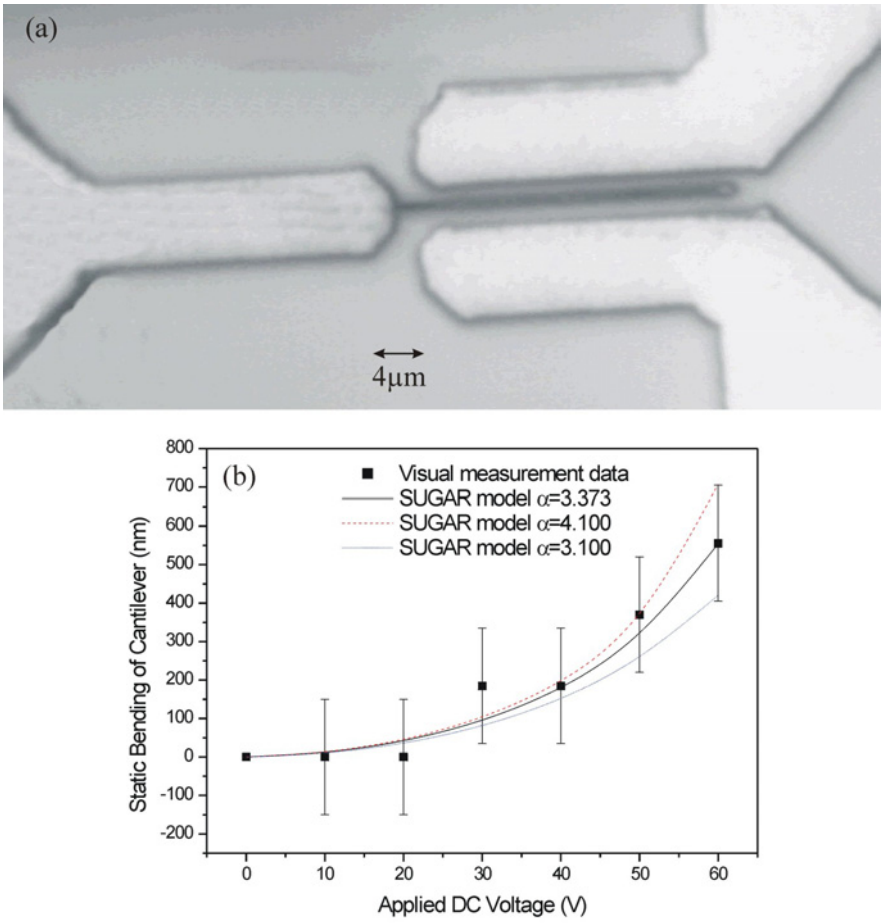

Figure 7.6: (a) Optical image of the cantilever taken with the visual characterization setup and (b) the static bending measurement data and three SUGAR simulations, with fringe factor 3.1, 3.73 and 4.1.

things, (1) a thinner cantilever than expected or (2) a lower Young's modulus than expected.

Dynamic measurements

In figure 7.8 the frequency response measured by the visual setup is shown for device 1. By fitting the data with a Lorentzian function the Q-factor is measured to be approximately 55. In order to be able to compare the SPICE model the fringe factor α, found by the static measurements was used. A value of α=3.73 was used. In figure 7.9 the resonant frequency of the cantilever as a function of the sum of the applied voltages squared is seen. By making a linear fit f_0 is calculated to 671192Hz. By using fixing the Young's modulus to 160GPa, which

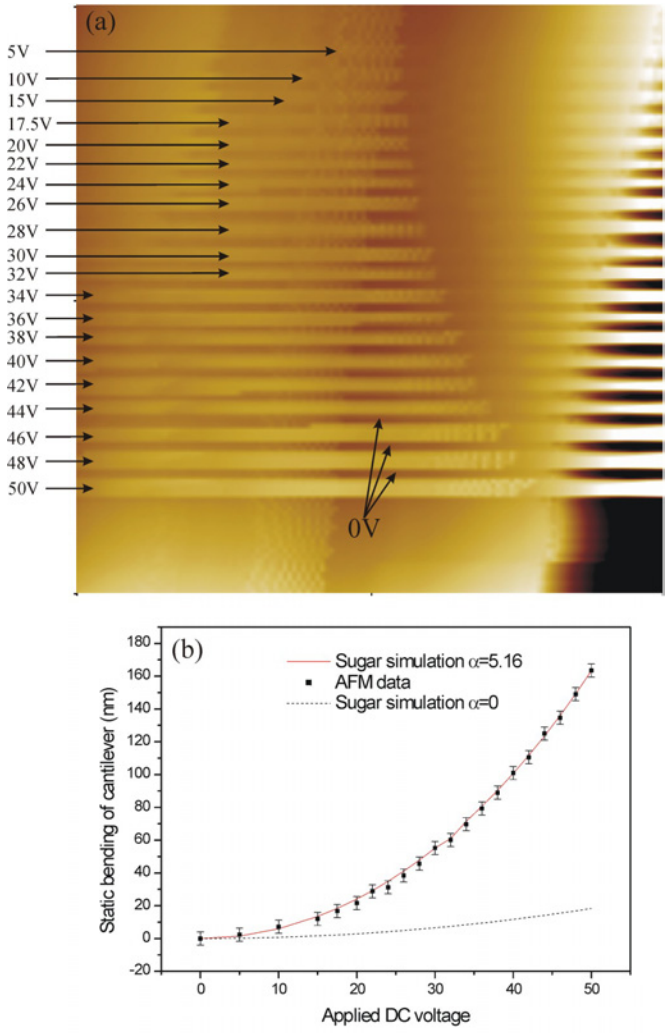

Figure 7.7: (a) AFM image of the cantilever, which is used to measure static bending of the cantilever at different applied DC voltages and (b) the static bending data together with two SUGAR simulations with α=0 and α=5.16.

is a typical value of poly-Si, the effective density of the sensor was calculated to 3.27g/cm^3. The SPICE simulation of the device is also seen in figure 7.9, which seems to fit very accurately with the visual data.

Summary

In table 7.1 the main finings of the characterization of the poly-Si cantilevers in air are found. The two fringe factor measurements of approximately 3.73 and 5.16 for device 1 and 2 respectively were found. The gap size of device 2 is over a

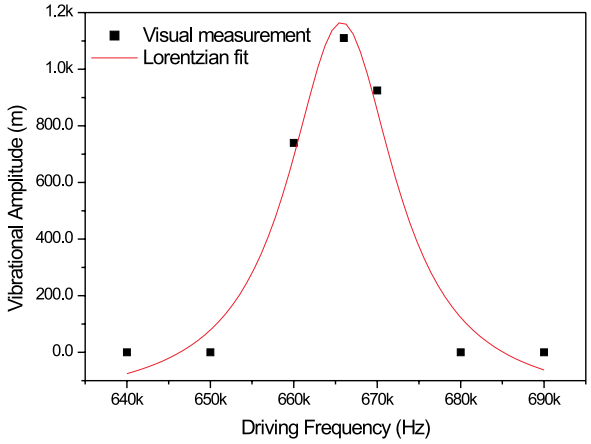

Figure 7.8: Frequency response of device 1 measured with the visual setup together with a Lorentzian fit. The Q-factor is measured to approximately 55.

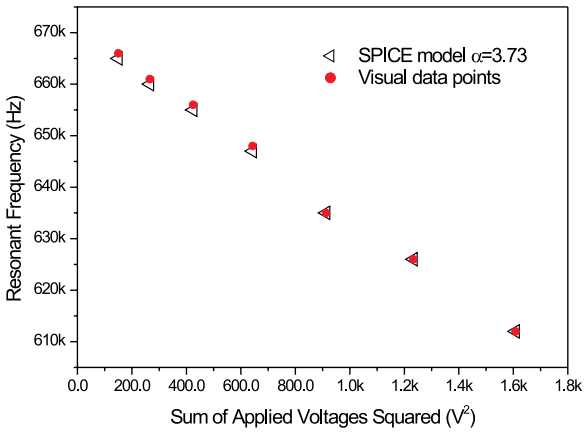

Figure 7.9: The resonant frequency of the cantilever as a function of the sum of the applied voltages squared for device 1 measured by the visual setup along with a SPICE simulation using α=3.73.

500nm larger than device 1 and the width is also larger, which could explain the larger value of fringe factor. Furthermore, the values correspond to a total capacitance increase of roughly 4 and 5 times for device 1 and 2 respectively. Again, this can be explained by an overestimated Young's modulus and cantilever width.

device	setup	w	h	l	gap	E	α	Q	f_0	ρ_{eff}
device 1	Visual	911nm	1.8μm	39.20μm	1.87μm	160GPa	3.73	55	671.9kHz	3.27g/cm^3
device 2	AFM	980nm	1.8μm	40.00μm	2.5μm	160GPa	5.16	-	-	-
device 3	Visual	1μm	1.8μm	39.56μm	2.03μm	160GPa	-	-	645.6kHz	4.12g/cm^3
device 4	Visual	981nm	1.8μm	39.73μm	1.94μm	160GPa	-	-	658.3kHz	3.72g/cm^3

Table 7.1: The α, Q, f_0 and ρ_{eff} findings for five cantilevers measured by the visual setup and the AFM setup.

The other finding of these results is that the effective density of the cantilever is larger than the normal density of Si, which is 2.33g/cm^3. This denotes that the damping mechanism is not squeeze film damping where the air molecules can move freely between the cantilever and parallel electrode.

7.2.2 Vacuum measurements

All the vacuum measurements have been performed with the SEM setup. By imaging the cantilever, the static bending and dynamic vibrational amplitude of the cantilever are measured.

Static measurements

In figure 7.10a a SEM image of the cantilever and two parallel electrodes are seen from above. By zooming in the static displacement of the cantilever can be measured at different DC voltages. In figure 7.10b and c the close-up images show the apex of the cantilever where a potential of 0V and 130V respectively are applied between the top electrode and the cantilever. In figure 7.10d the whole device, including bond pads, is seen. When a high DC voltage is applied, the positively charged top electrode becomes dark compared to the negatively charged cantilever and bottom electrode, see figure 7.10c. This is because the secondary electrons are being reduced in the positively charged electrode and vice-versa for the cantilever. In figure 7.11 the measured DC response of the cantilever is presented. SUGAR simulations with α values of 0.5 and 1.5 are compared. It seems that the SUGAR model fits very poorly to the SEM data. A possible explanation could be charging effects due to the electron radiation. In figure 7.10c the bright area around the cantilever apex is due to charging of the system. It was seen that while performing the measurements the behavior of the cantilever would change, just by changing the electron scan speed or magnification.

Dynamic measurements

In figure 7.12 two SEM images of a cantilever, which is excited at its 1st and 2nd mode are shown. The frequencies of the first and second mode are 315kHz and 1.8MHz respectively. These images show the details of the cantilever bending,

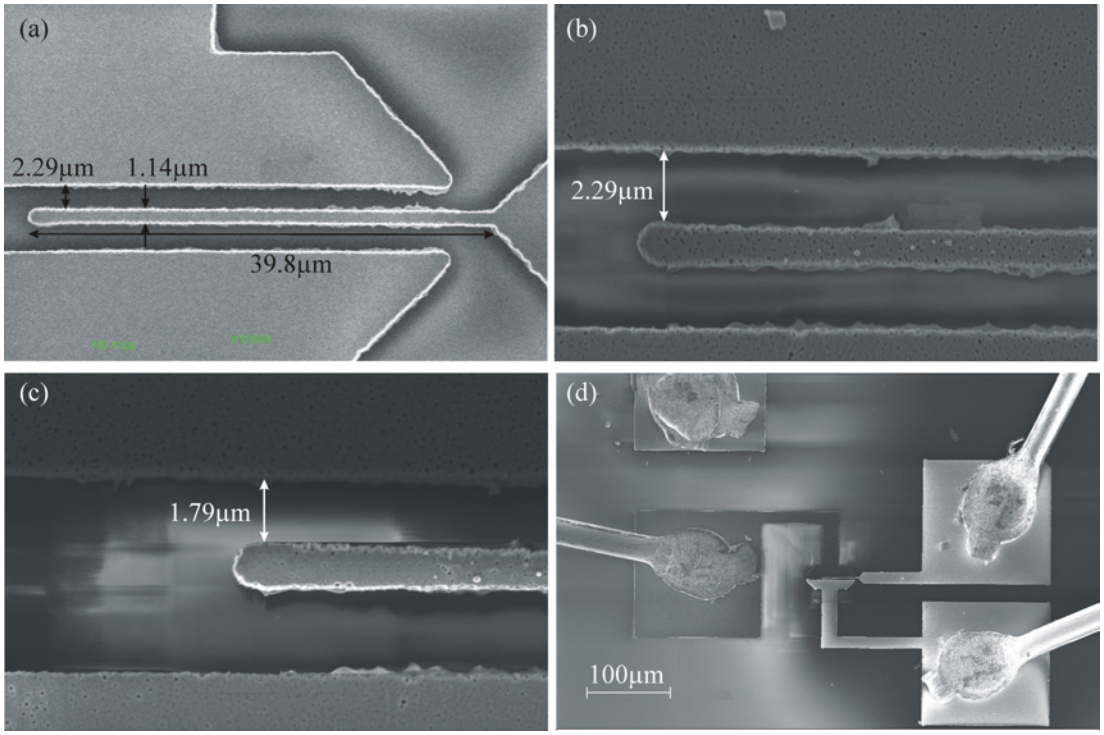

Figure 7.10: (a) SEM image of the cantilever and two parallel electrodes of device 5. Close-up images of the cantilever at (b) 0V and (c) 135V and (d) the whole device at V=130V, showing the dark and light regions corresponding to the positively and negatively charged areas.

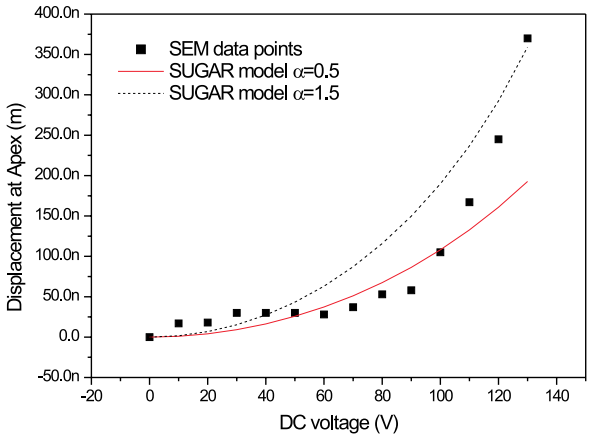

Figure 7.11: The static bending as a function of the applied DC voltage together with SUGAR simulations with α=0.5 and 1.5. on device 5

which are impossible to observe on such small devices with an optical microscope. In air the 2nd mode of vibration has not been possible to excite because the Q-factor in air is much lower than in vacuum. This is because the main contributor of damping in air is acoustic and in vacuum acoustic damping in eliminated.

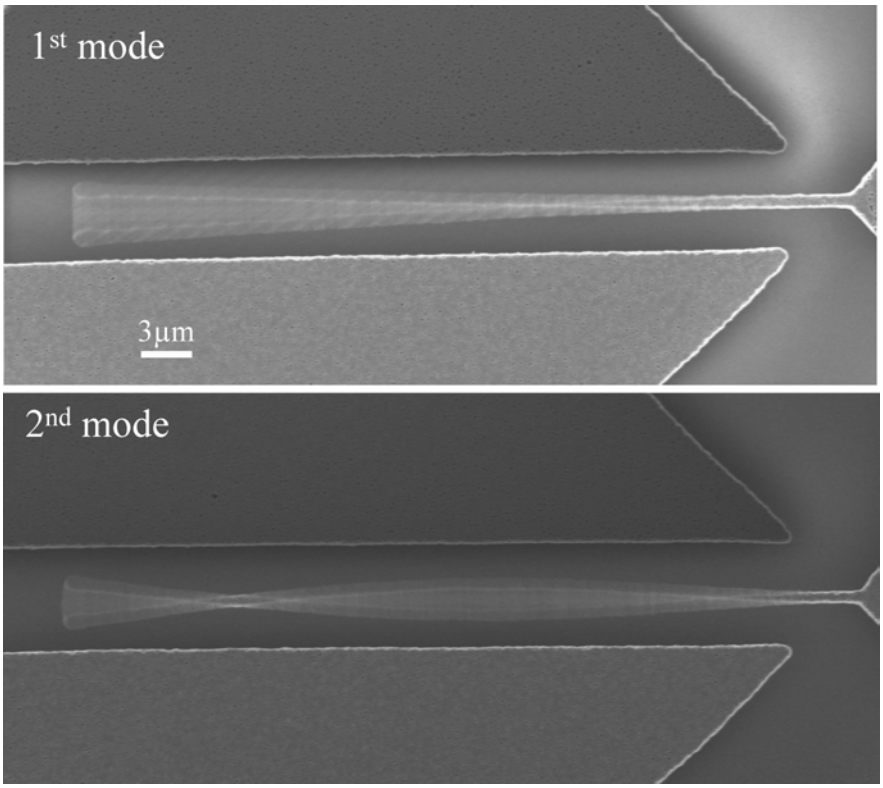

Figure 7.12: Two SEM images of a cantilever showing the first and second vibrational modes. In the top image the cantilever is driven with a frequency of 315kHz and in the bottom image it is driven with a frequency of 1.8MHz.

In figure 7.13 the dynamic response of the cantilever as a function of the AC driving frequency is seen. The Gaussian fit to the curve reveals that the Q-factor is approximately 15000. This is approximately 270 times higher than in air. As seen in equation 2.2-36 the acoustic Q-factor contribution is zero, so the energy losses in the system are due to structural defects and imbalances in the structure. Compared to other cantilever based devices in vacuum this value is in good agreement, where Q-factors up to 20000 were reported for single-crystal cantilevers [130][131][132]. This signifies that the structural and mechanical properties of these poly-Si devices are good.

As with the air measurements the resonant frequency versus the sum of the applied voltage squared has been measured, in order to calculate the effective

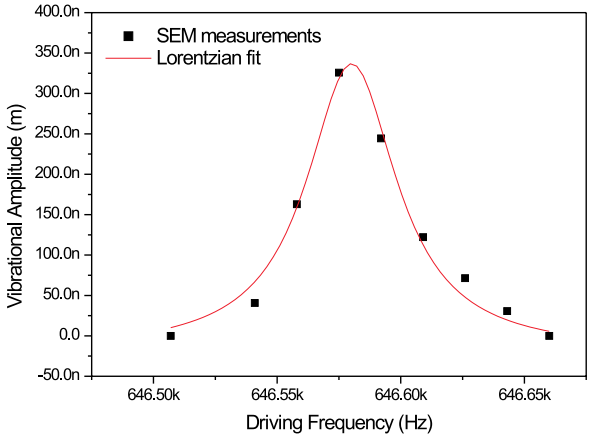

Figure 7.13: The frequency response of device 6 in vacuum measured by the SEM along with a Lorentzian fit. The applied voltages in this measurement were Vac=100mV and Vdc=0.

density of the cantilever in vacuum. In figure 7.14 the resonant frequency versus the sum of the applied voltages squared is seen. In the same graph SPICE simulations with α values of 1.5, found by the static measurements and 5.1 are shown. It is seen that the fringe factor found by the static measurements does not fit this data. Instead, a higher fringe factor of 5.1 fits the measurements much better. Furthermore, this value fits better with the air measurements found in table 7.1, which makes sense since the fringe factor should not depend on whether the device is operated in vacuum or air.

Summary

The main findings of the vacuum characterization of the poly-Si cantilevers are shown in table 7.2. With the static measurements the fringe factor was seen to be lower than the air measurements and didn't fit well with the SUGAR model. On the other hand, the dynamic measurements revealed that a higher fringe factor fit the dynamic measurement data. This could be explained by charging effects, which can alter the behavior of the cantilever. Unfortunately, no other static measurements were performed to compare.

Another aspect of these findings is that the effective density of the cantilever increased compared to the air measurements. This can again be explained by extra external forces acting on the cantilever, due to electrostatic charging.

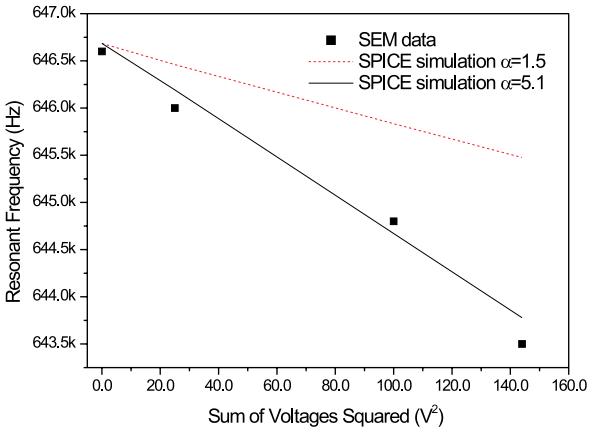

Figure 7.14: The resonant frequency as a function of the sum of the applied voltages squared, comparing the SEM measurements and two SPICE simulations with α=1.5 and 5.1 on device 6.

device	setup	w	h	l	gap	E	α	Q	f_0	ρ_{eff}
device 5	SEM	1.14μm	1.8μm	39.8μm	2.3μm	160GPa	0.5-1.5	-	-	-
device 6	SEM	1μm	1.8μm	39.5μm	2.0μm	160GPa	5.1	15000	647kHz	4.11g/cm^3

Table 7.2: The α, Q, f_0 and m_{eff} findings for two cantilevers measured by the SEM setup.

7.2.3 Air versus vacuum measurements

In table 7.3 f_0 for several devices, measured both in and out of vacuum, are listed. The the effective density of the cantilevers is calculated from f_0 and by assuming the Young's modulus is 160GPa. The air measurements were performed with the visual setup and the vacuum measurements were performed with the SEM setup. Six different cantilevers were measured and the first conclusion is that the effective mass of each cantilever is very different from each other. The second conclusion is that the effective density decreases in vacuum compared to air, which is to be expected due to the added acoustic mass. For all the devices the decrease in effective density is approximately 1%. By approximating the acoustic mass as the mass in a volume comparable to the volume filling the gap between the cantilever and parallel electrodes, a value of approximately 1pg of air molecules is found. This roughly matches the drop of 1% in the resonant frequency.
The variation in the calculated effective densities could be due to two several factors. (1) The Al based mask tends to have pinholes, which are transferred to the cantilever during dry etching. The pinhole density is very dependent on the laser power and focus of the laser, which is different for each device.

device	w	h	l	E	$f_0 air$	$f_0 vac$	$\rho_{eff} air$	$\rho_{eff} vac$
device 7	1.004μm	1.8μm	39.56μm	160GPa	645.6kHz	646.6kHz	4.121g/cm^3	4.109g/cm^3
device 8	0.981μm	1.8μm	39.73μm	160GPa	658.3kHz	659.8kHz	3.720g/cm^3	3.703g/cm^3
device 9	0.967μm	1.8μm	39.62μm	160GPa	564.7kHz	566.2kHz	4.967g/cm^3	4.941g/cm^3
device 10	1.156μm	1.8μm	39.55μm	160GPa	639.7kHz	642.9kHz	5.571g/cm^3	5.516g/cm^3
device 11	1.061μm	1.8μm	40.00μm	160GPa	662.0kHz	666.4kHz	4.188g/cm^3	4.133g/cm^3
device 12	1.165μm	1.8μm	39.27μm	160GPa	689.1kHz	692.2kHz	5.016g/cm^3	4.971g/cm^3

Table 7.3: The measured $f_0 air$ and $f_0 vac$ and the calculated $\rho_{eff} air$ and $\rho_{eff} vac$ using the measured f_0 and E=160GPa.

This porous surface of the poly-Si could decrease the Young's modulus. (2) The vacuum measurements were performed before the air measurements and while imaging with the SEM, carbon deposition, due to electron beam induced deposition, occurs. (3) The Cantilever's spring constant is dependent on the width cubed, equation 2.1-3 and the resonant frequency is linearly dependent on the width, equation 2.1-7. This means that small deviations in the measurement of the width could lead to large changes in the stiffness and resonant frequency of the cantilever.

7.3 CMOS integrated cantilevers

Due to stiction problems the fabrication and characterization of the CMOS integrated cantilevers have been a challenge. The characterization of the cantilevers has been performed with the visual setup where the motion of the cantilever has been observed at the same time as electrical measurements are performed.

7.3.1 Visual measurements

In figure 7.15 some optical images of a double cantilever device in the nanoarea are shown. In figure 7.15a the nanoarea of the double cantilever device is seen and in figure 7.15b a close-up of the cantilevers are seen. These images show that the cantilever is vibrating at the end. Electrical measurements on this device was not possible due to faulty CMOS circuitry, but it proves that excitation of the cantilevers is possible.

7.3.2 Electrical measurements

Static measurements

In order to measure the parasitic capacitance of the system, static characterization of the cantilever and amplification circuit, as seen in figure 7.16, was performed. In figure 7.16a a simple diagram showing the cantilever and circuit

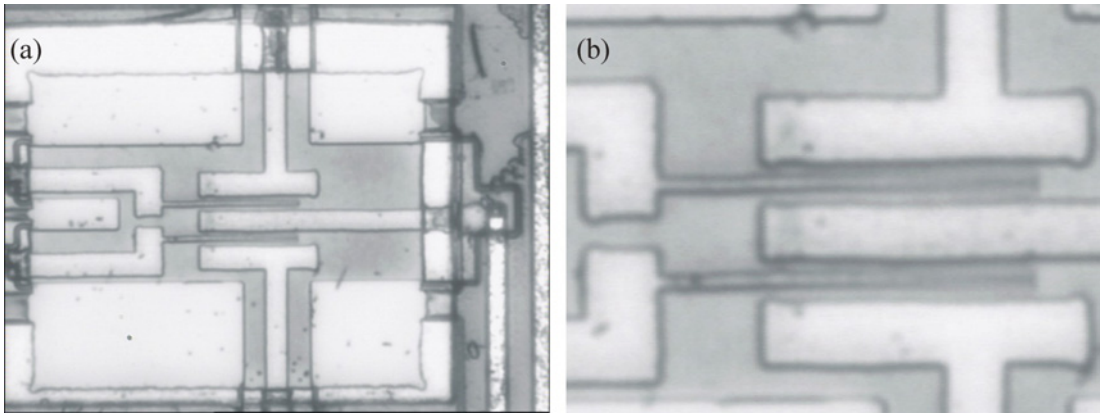

Figure 7.15: In (a) the double cantilever nanoarea is shown and in (b) a close-up of the two cantilevers are seen vibrating and the end. Electrical characterization was not performed due to faulty CMOS.

is shown and in figure 7.16b the equivalent diagram is shown showing the capacitances in the system. The cantilever's capacitance is denoted by C_{can} and the parasitic capacitance is denoted as C_{pa}. By using this simple electrical model, the gate voltage V_g can be determined as a function of the input voltage V_{in}, C_{can} and C_{pa}:

$$V_g = \frac{C_{can}}{C_{can} + C_{pa}} \cdot V_{in} - 2.5\frac{C_{pa}}{C_{pa} + C_{can}} \tag{7.3-1}$$

The parasitic capacitance contains the cantilever-substrate capacitance and the circuit input capacitance. By placing a STM tip on the cantilever anchor, V_g was accessed. In figure 7.17 V_{out} as a function of both V_g and V_{in} has been measured. In the linear regions of these curves, the circuit transistors are polarized and the circuit has a finite DC gain. By measuring the slopes in the linear regions (shown as the linear fits on figure 7.17 a and b) together with an estimated value of C_{can} based on the cantilever geometry, the parasitic capacitance was calculated to 1.32fF. This value is very low, suggesting that the electrical readout should be obtainable using the chosen amplification scheme.

Dynamic measurements

Electrical measurements on one device has been obtained. The measurement was performed on a BS circuit with a cantilever and comb capacitor fabricated on the nanoarea. An image of this type of device can be seen in figure 5.6. Due to the small amplitudes of vibration, which is under 200nm for these measurements, no optical images of the vibration where possible. In table 7.4 the dimensions of the

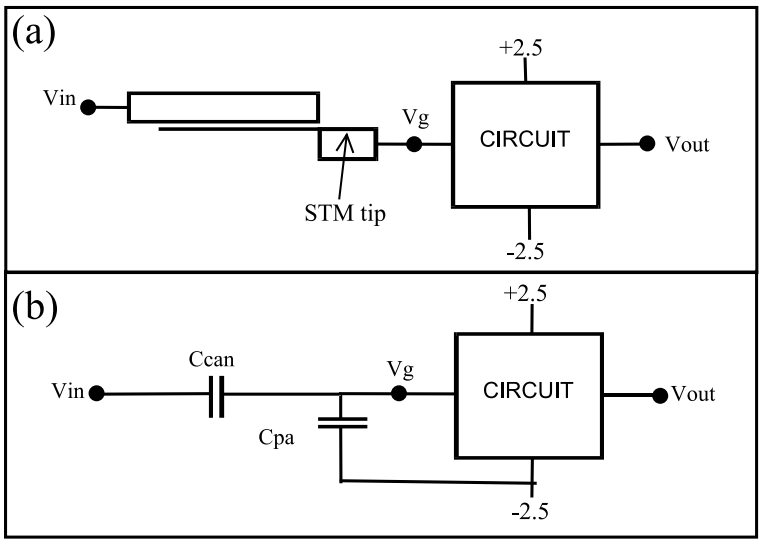

Figure 7.16: In (a) a simple diagram on the whole device is seen denoting where the STM tip accesses the gate voltage V_g and (b) is the equivalent diagram showing the cantilever and parasitic capacitances.

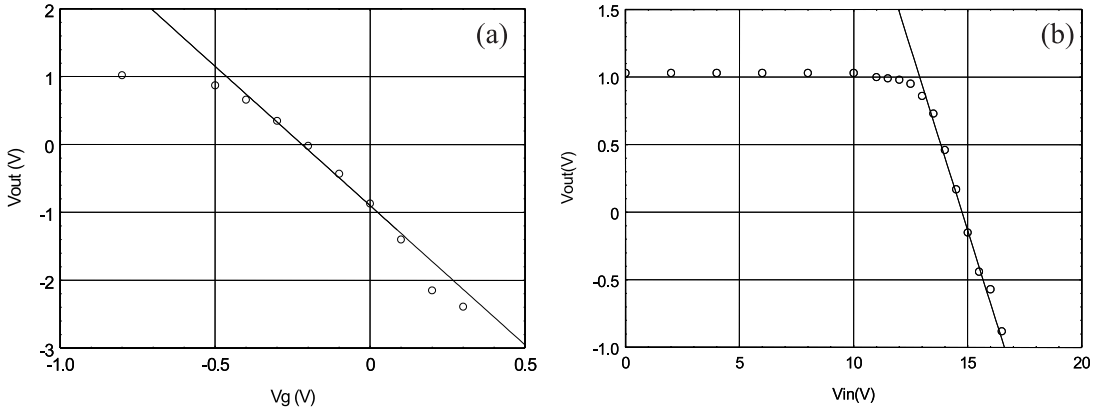

Figure 7.17: The output voltage of the CMOS circuitry as a function of (a) the gate voltage V_g and (b) the input voltage V_{in}.

cantilever and measurements can be seen.

In figure 7.18 the readout circuitry's voltage output is shown as a function of the AC voltage frequency. This cantilever has a width, height and length of 1μm, 0.6μm and 40μm respectively. The two curves correspond to two excitation voltages. The dashed curve has an excitation voltage of 18VDC + 7VppAC and the solid curve corresponds to an excitation voltage of 20VDC + 7VppAC. It is seen that the higher excitation voltage increases the amplitude of the output

signal and reduces the resonant frequency from 655kHz to 645kHz. The reason for this is that the extra DC voltage increases the electrostatic forces acting on the cantilever, which increases the vibrational amplitude and decreases the resonant frequency. The quality factor (Q) of the cantilever was measured to be approximately 43 by fitting a Lorentzian curve to the data points.

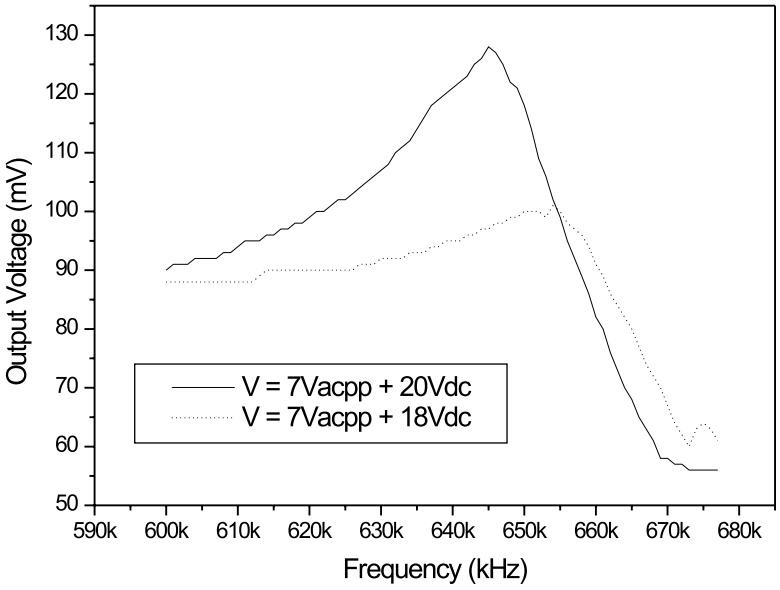

Figure 7.18: The output voltage of the readout circuitry for two applied voltages to a laser defined cantilever.

By taking the two measurements and plotting the resonant frequency versus the sum of the applied voltage squared f_0 can be calculated. The SPICE model with α=6.5 has been used to model the cantilever. In figure 7.19 the resonant frequency versus the sum of the applied voltage squared is seen for the two measurements along with the SPICE model.

The SPICE model can also be used to simulate the actual signal of the cantilever, which can then be compared to the electrical output of the device. In figure 7.20 the electrical signal and the SPICE simulation for the two frequency responses along with the corresponding SPICE simulation are seen. The parameters for the SPICE model are f_0=693kHz, α=6.5, Q=30 and C_{pa}=10fF. In figure 7.20a the measurement with V_{in}=18VDC+7VACpp is shown. The simulation predicts the peak very well, but a low frequency the model deviates slightly. In figure 7.20b the measurement with V_{in}=20VDC+7VACpp is shown. In this simulation

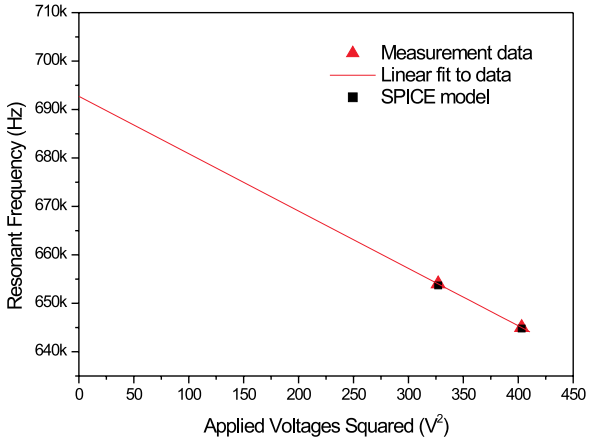

Figure 7.19: The resonant frequency versus the sum of the applied voltage squared for the two electrical measurements showing the resonant frequency at 0V to be approximately 692kHz.

the SPICE model models very precisely the shape of the output signal. Due to the saturation of the BS circuit the output could not go below 55mV. This means that the anti-peak is not seen, which makes it difficult to match a parasitic capacitance. Thus the value of 10fF is just an estimation, and perhaps not the actual value.

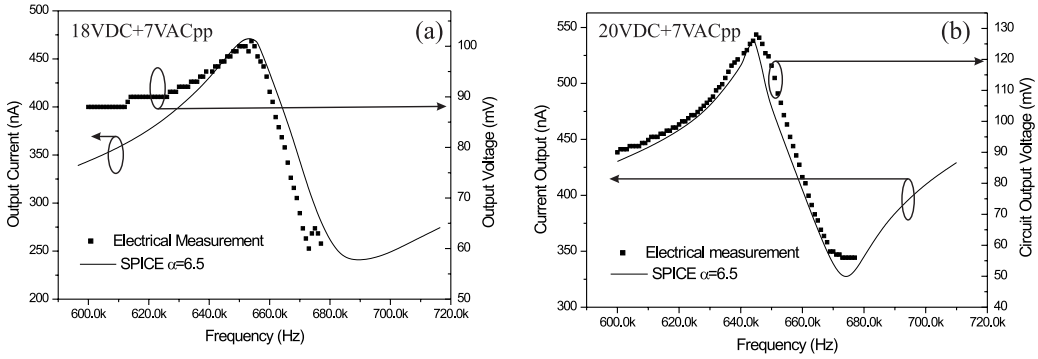

Figure 7.20: The electrical measurement and SPICE simulations for the device. The parameters for the SPICE model are f_0=693kHz, α=6.5, Q=30 and C_{pa}=10fF.

7.3.3 Electrical characterization summary

In table 7.4 the main findings of the electrical characterization is seen. The Q-factor was measured to be approximately 43 when measuring directly from the circuit output data, but a lower value of 30 was used for the final SPICE simulations in figure 7.20. These values are slightly lower than the poly-Si cantilevers without CMOS, which can be explained by the a higher damping because the gap between the cantilever and bottom substrate is smaller. Furthermore, SEM images of the CMOS integrated cantilever reveal that the cantilever are very porous compared to the poly-Si cantilever without CMOS, which could also lower the Q-factor. Since no DC measurements have been performed, the fringe factor was calculated by simulating the resonant frequencies until the model predicted the correct values, which it did when α=6.5. This value is higher than the values found with the poly-Si cantilevers. This can be explained by the fact that the CMOS cantilever is 600nm high compared to 1.8μm high non-CMOS cantilevers and that the CMOS cantilevers have a higher roughness, which could decrease effective Young's modulus of the cantilever. By comparing the SPICE model with the measurements a good agrement of the peak is seen. The effective density of the cantilever is calculated to 2.4g/cm^3, which is lower than the non-CMOS poly-Si cantilevers in and out of vacuum. It is also very close to the text-book value of 2.33g/cm^3 for single crystal Si.

device	setup	w	h	l	gap	E	α	Q	f_0	ρ_{eff}	C_{par}
device 13	CMOS	0.84μm	0.6μm	40.0μm	1.8μm	160GPa	6.4	30	693kHz	2.4g/cm^3	10fF

Table 7.4: The α, Q, f_0 and m_{eff} findings for one cantilever measured with the CMOS circuitry.

7.4 Metal cantilevers

7.4.1 Dynamic measurements

As described in the previous chapter, aluminum cantilevers have been fabricated. The main goal with these cantilevers was to make an approximately 1μm high and 500nm wide structure. However, so far only thin structures with a thickness of approximately 100nm have been fabricated. Non-the-less, these types of cantilevers can also be excited vertically into resonance by applying an AC voltage between the driver and cantilever due to the field asymmetry induced by the Si substrate. In figure 7.21 two SEM images at different AC driving frequencies are shown, showing the vertical vibration of the cantilever when at resonance at f_{ac}=1435kHz.

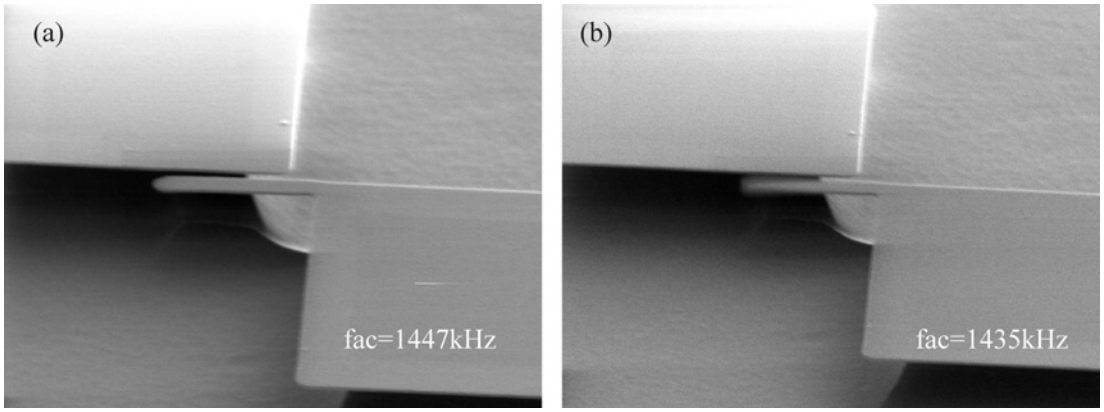

Figure 7.21: Two SEM images of a metal cantilever being excited with an AC frequency of (a) 1447kHz and (b) 1435kHz.

By examining the images the approximate vibrational amplitude versus the driving frequency can be measured, even though the cantilever is imaged at an angle. Thus the frequency response of the cantilever can be measured as shown in figure 7.22. The Q-factor is found from the fitted Lorentzian to be approximately 183. This value is much lower than the values found from the poly-Si cantilevers in vacuum, which was approximately 15000. Since there is no acoustic damping, only structural defects and imbalances in the cantilever have to be considered, see equation 2.2-36. By looking in figure 7.21, it is seen that the support of the Al cantilever is underetched by approximately 1.4μm. This means that the clamping of the cantilever is very poor and energy of the system is lost through the clamping.

The width and length of the cantilever have been measured with the SEM to 660nm and 5.2μm respectively. The theoretical vertical resonant frequency of this cantilever is approximately 3MHz, which is much higher than the resonant frequency measured here. The main explanation could be that the cantilever has been excited at the half frequency, which fits the numbers. The AC voltage used to excite the resonance was 9Vpp, which is very high and also supports the theory of exciting at half frequency.

In order to improve the clamping of the Al cantilever the process sequence could be altered slightly. In the last underetching step, see figure 6.12, an isotropic etch is used. Instead of this an anisotropic etch can be used to etch down into the substrate, then the isotropic etch can be used to underetch the Al cantilever. In this way there is still a large distance between the cantilever and the substrate and at the same time the underetching of the cantilever support is minimized to approximately half the width of the cantilever.

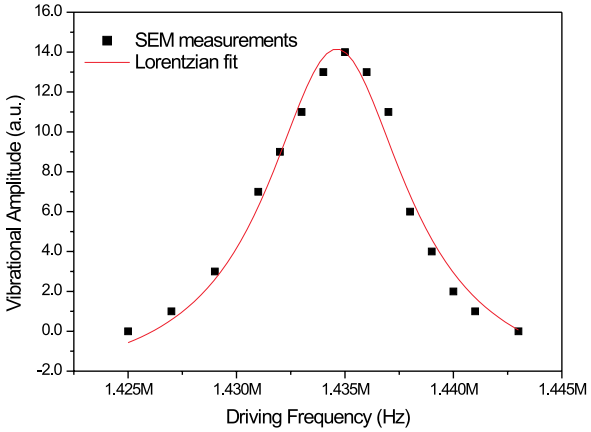

Figure 7.22: The Frequency response of the metal cantilever seen in figure 7.21. By using the Lorentzian fit the Q-factor is measured to approximately 183.

Another attempt of characterizing the Al cantilevers was performed, this time by using the secondary electron signal from the electron detector of the SEM. For this experiment a gain/phase analyzer was used to as the AC voltage source and to measure simultaneously the electron detector signal. During the measurements the electron beam is put into spot mode and the spot is placed at the end of the cantilever, see figure 7.24a. In this first attempt, the E-beam is perpendicular to the device surface and not tilted at an angle. In figure 7.23 the frequency response of the same cantilever as seen above is shown. In this measurement the AC voltage was 1V and the DC voltage is approximately 10V. By looking at the figure it seems that the when scanning the frequency spectrum the output signal jumps to a value and then slowly goes back to the original level. This corresponds to a non-linear behavior of the cantilever, probably due to a large vibrational amplitude. Furthermore, the frequency of the cantilever is found to be approximately 2.8MHz, which is exactly double the frequency found in the first experiment.

7.4.2 Mass measurement

During measuring of the cantilever it was noticed that the resonant frequency of the cantilever was steadily dropping with time. Then after turning off the spot mode and imaging the cantilever again it was found that an approximately 200nm mass had been deposited onto the end of the cantilever, where the E-beam had been focussed, see figure 7.24b. This mass is caused by electron induced deposi-

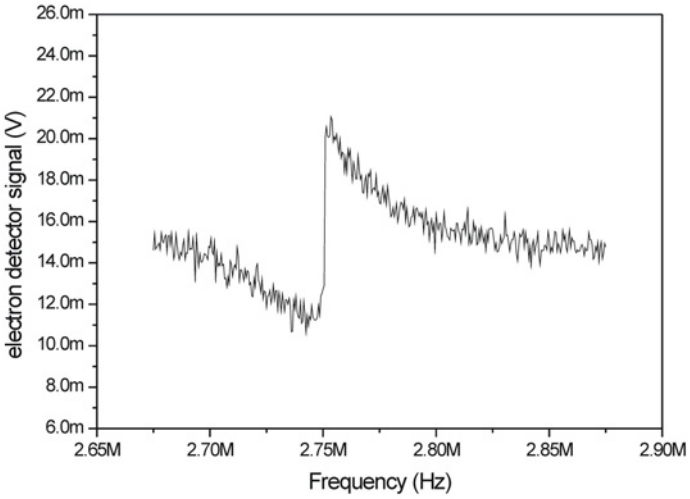

Figure 7.23: The frequency response of the same cantilever mentioned above, using the electron detector as readout. The resonant frequency in this curve is measured to 2.751MHz.

tion (EBID), where carbon based impurities in the vacuum chamber are broken down by the electrons and deposited onto the surface [133][134]. A frequency shift of 6.5kHz was measured and a rough estimation of the carbon deposit was calculated to 14fg. This leads to a mass sensitivity of approximately 10^{-18}g/Hz, which is in good agreement with equation 2.1-9.

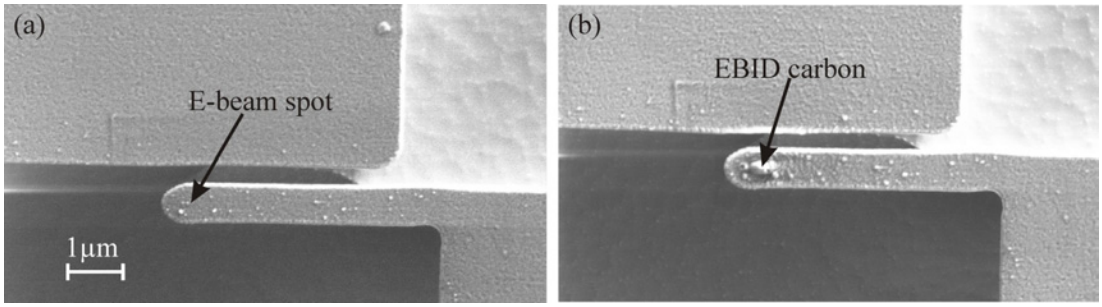

Figure 7.24: In (a) the Al cantilever is seen from above before carbon deposition and in (b) a approximately 200nm wide carbon deposition is seen on the end of the cantilever.

7.5 Summary

In this chapter the characterization of poly-Si and Al cantilevers without CMOS circuitry and CMOS integrated poly-Si cantilever have been presented.

Through the characterization of the poly-Si cantilevers, the fringe factor varied between 3.73 up to 6.5 for the performed experiments. Furthermore, the effective density of the almost all the poly-Si cantilevers are larger than the theoretical value. These trends can be explained by a lower Young's modulus, than the 160GPa used for the calculations, or a lower width of the cantilever. It was also seen that the CMOS cantilever had the highest fringe factor, which can be accounted for by the fact that the CMOS cantilever, see figure 5.6f, was more porous than the non-CMOS poly-Si cantilevers, see figure 7.5, thus having an even lower Young's modulus.

The Q-factor in air and vacuum was found to be approximately 50 and 15000 respectively, which is explained to large acoustic damping of the cantilever in air. Furthermore, it has been shown that the SPICE model can be used to successfully model both the mechanical and electrical behavior of the cantilever based mass sensor device.

It was shown that the ultra-thin Al cantilevers can be vertically excited into resonance with a lateral electrode and that due to poor clamping of the cantilever, the Q-factor is quite low (183) compared to the laterally vibrating poly-Si cantilevers. By focussing the electron beam at the apex of the cantilever and monitoring the electron detector signal, the frequency response of the cantilever was measured. Furthermore, EBID carbon was deposited due to the focused electron beam and the first mass measurements were performed. The mass sensitivity of the Al cantilever was measured to be 10^{-18}g/Hz.

Chapter 8

Conclusions

The main objective of the Ph.D. project described in this thesis is the fabrication and characterization of a cantilever based resonant mass sensor. The main outstanding qualities of this sensor are that it should have both a high spatial and mass resolution and that the sensor should be flexible, so that a range of possible applications can be addressed.

In the introduction the resonant or dynamic mode sensor was introduced and compared to a static mode sensor. Resonant based sensors have the main advantage that by monitoring the cantilever's resonant frequency and Q-factor, more information about what is happening to the cantilever can be deduced. From the dynamic behavior of the cantilever surface stress on the cantilever, mass deposition/absorption on the cantilever and even the environment surrounding of the cantilever can be measured. In contrast static mode measurements can only measure surface stress.

The design of the mass sensor is based on a nanometer scale cantilever, which is electrostatically actuated and which has a capacitive readout. In order to achieve this sensor the NANOMASS project was born, where the world of microelectronics meets the world of nanotechnology. By integrating the mass sensor with CMOS microelectronic circuitry, the mass sensor has the potential to be faster, cheaper, more sensitive and more compact than any other sensor of its kind. This thesis presents the journey of the development of this mass sensor from design to the first working demonstrator.

In order to facilitate the design and to predict the final performance of the mass sensor, a complete model of the electrical and mechanical properties of the capacitive based mass sensor was developed. This model consisted of a SPICE model and a 2D finite element model. Through a large signal treatment of the cantilever based capacitive system, and integrating this into SPICE, a model was formed that can simulate both the electrical and mechanical behavior of the device in

both the linear and the non-linear regimes. The weak point of this model is that the cantilever bending is approximated by a stiff plate displacement, which lead to the use of the 2D FE model, which is used to calibrate the SPICE model.

With the SPICE model it was shown that with the capacitive readout of the device it is crucial that the parasitic capacitances are reduced as much as possible. This lead to CMOS integration. Furthermore, it was seen that the two electrode configuration does not enhance the capacitive signal even though it is possible to apply higher DC to AC voltage ratios compared to the one electrode configuration.

It was decided that the first approach of integrating the mechanical device with CMOS was to use the lower poly0 layer of the CMOS and perform post-CMOS surface micromachining. This approach was chosen because of its simplicity, so that the principle of integration could be proven. The circuit design consisted of two types of circuits, which are the BS and AC amplifiers. The BS amplifier is based on a simple source follower and buffer amplifier, whereas the AC amplifier is based on a operational amplifier current to voltage converter. The challenge is to design amplifiers that have a high enough band-width and at the same time a high gain. For the poly-Si cantilevers fabricated in this thesis, the resonant frequency can be as high as 1.5MHz, which puts strick demands on the circuitry. With the 2.4μm CMOS technology that was used for the circuitry, a bandwidth and gain of 1.7MHz and 16dB was obtained for the BS circuit and 150kHz and 32dB for the AC circuits.

In chapter 5 the integration of the cantilevers was presented. The mask definition of the cantilever was performed by three nanolithography techniques, namely laser, E-beam and AFM lithography. Released cantilevers where achieved with laser and E-beam lithography, but due to high surface roughness, AFM lithography was not successful. Widths down to 700nm were achieved with laser lithography and widths down to 300nm were achieved with EBL. The main challenge of the cantilever processing was stiction of the cantilever to the bottom electrode upon releasing it. Two dry release techniques where investigated, a tert-butanol freeze-drying technique and a resist coating technique. It was found that the resist coating technique had the most reproducible and advantageous qualities.

An investigation of the post-processing effects on the CMOS revealed that e-beam evaporation and EBL caused damage to the CMOS. With e-beam evaporation X-ray radiation causes electron/hole where the holes get trapped in the gate oxide. It was found that this damage can be annealed out at 350^0C. Electron radiation from an electron source was also seen to damage CMOS. Below 5keV no damage or degradation was observed, but at higher acceleration voltages the CMOS becomes degraded, but can be repaired by annealing, and at high acceleration

voltage, 25keV, the CMOS is damaged irreparably. This is a major problem because EBL uses high acceleration voltage, >20keV, in order to minimize proximity effects.

In parallel with the integration of poly-Si cantilevers with CMOS, single crystal Si and Al cantilevers were also fabricated without CMOS. The objective with these demonstrators was to investigate new lithography techniques and structural materials for the cantilever that can be used for fabricating the 100nm wide device, which is the goal of the NANOMASS project. It was demonstrated that with AFM lithography, a 150nm wide cantilever can be fabricated, which proves AFM lithography to by a real contender of EBL, especially since EBL caused severe damage to the CMOS circuitry. It was also demonstrated that 400nm wide Al cantilevers can be fabricated with contact mask UV lithography. Furthermore, the Al cantilevers were only 100nm high, thus could be used at vertically vibrating cantilevers.

Finally, the characterization of poly-Si and Al cantilevers was performed. In order to characterize the cantilevers in air a visual and AFM setup were used. To characterize the cantilevers in vacuum a SEM setup was used. For the poly-Si cantilevers the fringe factor was found to be between 3.73 and 6.5 for the CMOS integrated and the non-CMOS integrated cantilevers. The effective densities of the poly-Si cantilever were also much higher than expected. These anomalies can be explained by a using a too large width or Young's modulus of the cantilever. However, measurements of the same cantilever in and out of vacuum gave predictable results with several different cantilevers, with respect to a drop in the resonant frequency of 1% due to the added acoustic mass in air. The SPICE model was used to compare with the measurements with rather good agreement. Electrical characterization was also performed on one cantilever. The SPICE model is very accurate at predicting the output signal. The Q-factor in air and vacuum was seen to be approximately 50 and 15000 respectively, which suggests that the acoustic damping is very dominant at atmospheric pressure.

With the SEM characterization setup it was seen that the Al cantilevers can be vertically vibrated by driving the cantilever with a lateral electrode. The Q-factor was found to be low, 183, which is probably due to poor clamping of the structure. Furthermore, by monitoring the electron detector signal readout of the cantilever was also possible and these measurements lead to the first mass detection of EBID carbon on the apex of the cantilever. The mass sensitivity was measured to be 10^{-18}g/Hz.

The main findings are that a model has been developed which can successfully predict both the systems electrical and mechanical behavior of a cantilever based mass sensor. This model was been used to facilitate the design of a CMOS inte-

grated cantilever based mass sensor. The fabrication of CMOS integrated poly-Si cantilever have been realized and the first electrical readout has been successful, proving that integration is possible. Furthermore, the fabrication of 150nm wide single crystal and 100nm high Al cantilevers have been demonstrated, paving the way to the next generation of even smaller, more sensitive mass sensor devices.

The next step is to further investigate the actual performance of the mass sensor system. This will be done both in vacuum and in air. In vacuum metal evaporation and latex sphere deposition will be attempted. If latex sphere can be attached to the cantilever at different places on the cantilever, the mass sensitivity of local deposition on the cantilever can be investigated. In air the mass sensor will be used as a gas and bio/chemical sensor. For the gas measurements only the resonant frequency and Q-factor will be monitored, but for bio/chemical applications, the cantilever needs to be functionalized. The preparations for these measurements are currently being pursued within the NANOMASS project.

Bibliography

[1] S. Middelhoek. Quo vadis silicon sensors? *Sensors and Actuators A (Physical)*, A41(1-3):1–8, 1994.

[2] R. Berger, Ch. Gerber, H.P. Lang, and J.K. Gimzewski. Micromechanics: A toolbox for femtoscale science: Towards a laboratory on a tip. *Microelectronic Engineering*, 35(1-4):373–379, 1997.

[3] A. Boisen, J. Thaysen, H. Jensenius, and O. Hansen. Environmental sensors based on micromachined cantilevers with integrated read-out. *Ultramicroscopy*, 82(1-4):11–16, 2000.

[4] B.H. Kim, F.E. Prins, D.P. Kern, S. Raible, and U. Weimar. Multicomponent analysis and prediction with a cantilever array based gas sensor. *Sensors and Actuators B (Chemical)*, B78(1-3):12–18, 2001.

[5] D. Lange, C. Hagleitner, O. Brand, and H. Baltes. Cmos resonant beam gas sensing system with on-chip self excitation. *Micro Electro Mechanical Systems, 2001. MEMS 2001. The 14th IEEE International Conference on*, pages 547–552, 2001.

[6] A. Hammiche, L. Bozec, M. Conroy, H.M. Pollock, G. Mills, J.M.R. Weaver, D.M. Price, M. Reading, D.J. Hourston, and M. Song. Highly localized thermal, mechanical, and spectroscopic characterization of polymers using miniaturized thermal probes. *Journal of Vacuum Science and Technology B: Microelectronics and Nanometer Structures*, 18(3):1322–1332, 2000.

[7] T. Lalinsky, E. Burian, M. Drzik, S. Hascik, Z. Mozolova, and J. Kuzmik. Thermal actuation of a gaas cantilever beam. *Journal of Micromechanics and Microengineering*, 10:293–298, 2000.

[8] K.B. Brown, W. Allegretto, F.E. Vermuelen, R.P.W. Lawson, and A.M. Robinson. Cantilever-in-cantilever micromachined pressure sensors fabricated in cmos technology. *Electrical and Computer Engineering, 1999 IEEE Canadian Conference on*, 3:1686–1691 vol.3, 1999.

[9] M. Zaborowski, P. Grabiec, T. Gotszalk, E. Romanowska, and I.W. Rangelow. A temperature microsensor for biological investigations. *Microelectronic Engineering*, 57-58:787–792, 2001.

[10] D.R. Baselt, G.U. Lee, K.M. Hansen, L.A. Chrisey, and R.L. Colton. A high-sensitivity micromachined biosensor. *Proceedings of the IEEE*, 85(4):672–680, 1997.

[11] T. Sulchek, R. Hsieh, S.C. Minne, C.F. Quate, and S.R. Manalis. Interdigital cantilever as a biological sensor. *Nanotechnology, 2001. IEEE-NANO 2001. Proceedings of the 2001 1st IEEE Conference on*, pages 562–566, 2001.

[12] P. A. Arutyunov and A. L. Tolstikhina. Atomic force microscopy as a universal means of measuring physical quantities in the mesoscopic length range. *Measurement Techniques*, 45(7):714–721, 2002.

[13] Masami Kageshima, Hisato Ogiso, Shizuka Nakano, Mark A. Lantz, and Hiroshi Tokumoto. Atomic force microscopy cantilevers for sensitive lateral force detection. *Japanese Journal of Applied Physics, Part 1: Regular Papers and Short Notes and Review Papers*, 38(6):3958–3961, 1999.

[14] G. Binning, C. Gerber, E. Stoll, T.R. Albrecht, and C.F. Quate. Atomic resolution with atomic force microscope. *Surface Science*, 189-190:1–6, 1987.

[15] D. Sarid. *Scanning force microscopy*. Oxford University Press.

[16] R. Wiesendanger. *Scanning Probe Microscopy and Spectroscopy*. Cambridge University Press, 1994.

[17] S.J. O'Shea, M.E. Welland, T.A. Brunt, A.R. Ramadan, and T. Rayment. Atomic force microscopy stress sensors for studies in liquids. *Journal of Vacuum Science and Technology B (Microelectronics and Nanometer Structures)*, 14(2):1383–5, 1996.

[18] H. Jensenius, J. Thaysen, P.A. Rasmussen, L.H. Veje, O. Hansen, and A. Boisen. A microcantilever-based alcohol vapor sensor-application and response model. *Applied Physics Letters*, 76(18):2615–2617, 2000.

[19] M.K. Baller, H.P. Lang, J. Fritz, Ch. Gerber, J.K. Gimzewski, U. Drechsler, H. Rothuizen, M. Desphont, P. Vettiger, F.M. Battiston, J.P. Ramseyer, P. Fornaro, E. Meyer, and H.-J. Guntherodt. A cantilever array-based artificial nose. *Ultramicroscopy*, 2000.

[20] J. Fritz, M.K. Baller, H.P. Lang, H. Rothuizen, P. Vettiger, E. Meyer, H.-J. Guntherodt, Ch. Gerber, and J.K. Gimzewski. Translating biomolecular recognittion into nanomechanics. *Science*, 288(5464):316–318, 2000.

[21] G. Wu, H. Ji, K. Hansen, T. Thundat, R. Datar, R. Cote, M.F. Hagan, A.K. Chakraborty, and A. Majumdar. Biological sciences - biophysics - origin of nanomechanical cantilever motion generated from biomolecular interactions. *Proceedings of the National Academy of Sciences of the USA*, 98(4):1560–1564, 2001.

[22] J. Thaysen, R. Marie, and A. Boisen. Cantilever-based bio-chemical sensor integrated in a microliquid handling system. *Technical Digest of MEMS 2001*, (Cat.No.01CH37090):401–404, 2001.

[23] J.E. Sader. Surface stress induced deflections of cantilever plates with applications to the atomic force microscope: Rectangular plates. *Journal of Applied Physics*, 89(5):2911–2921, 2001.

[24] H. Baltes, A. Koll, and D. Lange. The cmos mems nose-fact or fiction? *ISIE '97. Proceedings of the IEEE International Symposium on Industrial Electronics*, vol.1(Cat.No.97TH8280):SS152–157, 1997.

[25] C. Hagleitner, A. Hierlemann, D. Lange, A. Kummer, N. Kerness, O. Brand, and H. Baltes. Smart single-chip gas sensor microsystem. *Nature*, 414:293–296, 2001.

[26] Y.T. Yang, K.L Ekinci, X.M.H. Huang, L.M. Schiavone, and M.L. Roukes. Monocrystalline silicon carbide nanoelectromechanical systems. *Applied Physics Letters*, 78(2):162–164, 2001.

[27] A.N. Cleland and M.L. Roukes. Fabrication of high frequency nanometer scale mechanical resonators from bulk si crystals. *Applied Physics Letters*, 69(28):2653–2655, 1996.

[28] M.L. Roukes. Nanoelectromechanical systems. *TRANSDUCERS '01. EUROSENSORS XV. 11th International Conference on Solid-State Sensors and Actuators. Digest of Technical Papers*, pages 658–61 vol.1, 2001.

[29] H.P. Lang, R. Berger, J.K. Gimzewski, P. Fornaro, and E. Meyer. An artificial nose based on a micromechanical cantilever array. *Analytica Chimica Acta*, 393(1-3):59–65, 1999.

[30] H.P. Lang, R. Berger, F. Battiston, J.-P. Ramseyer, E. Meyer, C. Andreoli, J. Brugger, P. Vettiger, M. Despont, T. Mezzacasa, L. Scandella, H.-J. Guntherodt, C. Gerber, and J.K. Gimzewski. A chemical sensor based on a micromechanical cantilever array for the identification of gases and vapors. *Applied Physics A Materials Science*, 66(7):S61–S64, 1998.

[31] T. Thundat, G.Y. Chen, R.J. Warmack, D.P. Allison, and E.A. Wachter. Vapor detection using resonating microcantilevers. *Analytical Chemistry*, 67(3):519–521, 1995.

[32] T. Thundat, E.A. Wachter, S.L. Sharp, and R.J. Warmack. Detection of mercury vapor using resonating microcantilevers. *Applied Physics Letters*, 66(13):1695–7, 1995.

[33] J. Yang, T. Ono, and M. Esashi. Mechanical behavior of ultrathin microcantilever. *Sensors and Actuators*, 82:102–107, 2000.

[34] T. Ono, X. Li, H. Miyashita, and M. Esashi. Mass sensing of absorbed molecules in sub-picogram sample with ultrathin silicon resonator. *Review of Scientific Instruments*, 74(3):1240–1243, 2003.

[35] Z.L. Wang and P. Poncharal W.A. de Heer. Measuring physical and mechanical properties of individual carbon nanotubes by in situ tem. *Journal of Physics and Chemistry of Solids*, 61:1025–1030, 2000.

[36] J.W.M. Chon, Paul Mulvaney, and J.E. Sader. Experimental validation of theoretical models for the frequency response of atomic force microscopy cantilever beams immersed in fluids. *Journal of Applied Physics*, 87(8):3978–3988, 2000.

[37] J.E. Sader. Frequency response of cantilever beams immersed in viscous fluids with applications to the atomic force microscope. *Journal of Applied Physics*, 84(1):64–76, 1998.

[38] Rachel McKendry, Jiayun Zhang, Youri Arntz, Torsten Strunz, Martin Hegner, Hans Peter Lang, Marko K Baller, Ulrich Certa, Ernst Meyer, Hans-Joachim Guntherodt, and Christoph Gerber. Biological sciences - biophysics - multiple label-free biodetection and quantitative dna-binding assays on a nanomechanical cantilever array. *Proceedings of the National Academy of Sciences of the USA*, 99(15):9783–9788, 2002.

[39] K.M. Hansen, H.-F. Ji, G. Wu, R. Datar, R. Cote, A. Majumdar, and T. Thundat. Cantilever-based optical deflection assay for discrimination of dna single-nucleotide mismatches. *Analytical Chemistry A*, 73(7):1567–1571, 2001.

[40] B. Ilic, D. Czaplewski, M. Zalalutdinov, H.G. Craighead, P. Neuzil, C. Campagnolo, and C. Batt. Single cell detection with micromechanical oscillators. *Journal of Vacuum Science and Technology B: Microelectronics and Nanometer Structures*, 19(6):2825–2828, 2001.

[41] N. Blanc, J. Brugger, and N.F. de Rooij. Scannin force microscopy in the dynamic mode using microfabricated capacitive sensors. *Journal of Vacuum Science and Technology B*, 14(2):901–905, 1996.

[42] I.-S. Chen, J.F. Roeder, D.-J. Kim, J.-P. Maria, and A.I. Kingon. Metalorganic chemical vapor deposition pb(zr,ti)o3 and selected lower electrode structures as a pathway to integrated piezoelectric microelectromechanical systems. *Journal of Vacuum Science and Technology B*, 19(5):1833–1840, 2001.

[43] A.N. Cleland, M. Pophristic, and I. Ferguson. Single-crystal aluminum nitride nanomechanical resonators. *Applied Physics Letters*, 79(13):2070–2072, 2001.

[44] J. Gaspar, V. Chu, N. Louro, R. Cabeca, and J.P. Conde. Thermal actuation of thin film microelectromechanical structures. *Journal of Non-Crystalline Solids*, 299-302(Part 2):1224–1228, 2002.

[45] Jacques Jonsmann. *Technology Development for Topology Optimised Thermal Microactuators*. PhD thesis, Mikroelektronik Centret, 2000.

[46] D.S. Greywall, B. Yurke, P.A. Busch, A.N. Pargellis, and R.L. Willett. Evading amplifier noise in nonlinear oscillators. *Physical Review Letters*, 72(19):2992–5, 1994.

[47] D.S. Greywall, B. Yurke, P.A. Busch, and S.C. Arney. Low-temperature anomalies in the dissipation of small mechanical resonators. *Europhysics Letters*, 34(1):37–42, 1996.

[48] H.J. Cho and C.H. Ahn. A novel bi-directional magnetic microactuator using electroplated permanent magnet arrays with vertical anisotropy. *Micro Electro Mechanical Systems, 2000. MEMS 2000. The Thirteenth Annual International Conference on*, pages 686–691, 2000.

[49] B. Yu, W. Allegretto, and A.M. Robinson. Dynamic response of a magnetically actuated micromachined cantilever with a permalloy electroplated film. *Electrical and Computer Engineering, 1999 IEEE Canadian Conference on*, 3:1643–1647 vol.3, 1999.

[50] T. Goddenhenrich, H. Lemke, U. Hartmann, and C. Heiden. Force microscope with capacitive displacement detection. *Journal of Vacuum Science and Technology A (Vacuum, Surfaces, and Films)*, 8(1):383–7, 1990.

[51] G. Neubauer, S.R. Cohen, G.M. McClelland, D. Horne, and C.M. Mate. Force microscopy with a bidirectional capacitance sensor. *Review of Scientific Instruments*, 61(9):2296–308, 1990.

[52] M. Madou. *Fundamentals of microfabrication*. CRC Press LLC, 1997.

[53] S.M. Sze. *Semiconductor devices, Physics and Technology*. Bell Telephone Laboratories, Inc., 1985.

[54] J. Thaysen, A. Boisen, O. Hansen, and S. Bouwstra. Atomic force microscopy probe with piezoresistive read-out and highly symmetrical wheatstone bridge arrangement. *Sensors and Actuators*, 83:47–53, 2000.

[55] P. Rasmussen, J. Thaysen, S. Bouwstra, and A. Boisen. Modular design of afm probe with sputtered silicon tip. *Sensors and Actuators A*, 92:96–101, 2001.

[56] Y. Su, A.G.R. Evans, A. Brunnschweiler, and G. Ensell. Characterization of a highly sensitive ultra-thin piezoresistive silicon cantilever probe and its applications in gas flow velocity sensing. *Journal of Micromechanics and Microengineering*, 12:780–785, 2002.

[57] Y. Su, A.G.R. Evans, and A. Brunnschweiler. Micromachined silicon cantilever paddles with piezoresistive readout for flow sensing. *Journal of Micromechanics and Microengineering*, 6:69–72, 1996.

[58] J. Thaysen, A.D. Yalcinkaya, R.K. Vestergaard, S. Jensen, M.W. Mortensen, P.Vettiger, and A. Menon. Su-8 based piezoresistive mechanical sensors. *Technical Digest of MEMS 2002*, (CatNo.0780371852):320–323, 2002.

[59] R.P. Ried, H.J. Mamin, B.D. Terris, Long-Sheng Fan, and D. Rugar. 6-mhz 2-n/m piezoresistive atomic-force microscope cantilevers with incisive tips. *Journal of Microelectromechanical Systems*, 6(4):294–302, 1997.

[60] L. Ristic. *Sensor technology and devices*. Artech House, Boston, 1994.

[61] J.T. Ravnkilde. *Metallic microdevices for monolithic integrated microsystems*. PhD thesis, Mikroelektrnik Centret, April 1991.

[62] S.C. Jacobsen, M.G. Mladejovsky, C.C. Davis, J.E. Wood, and R.F. Wyatt. Advanced intelligent mechanical sensors (aims). *Solid-State Sensors and Actuators, 1991. Digest of Technical Papers, TRANSDUCERS '91., 1991 International Conference on*, pages 969–973, 1991.

[63] M.M.O. Lee. Merged technology on mems. *Electron Devices Meeting, 1997. Proceedings., 1997 IEEE Hong Kong*, pages 128–135, 1997.

[64] R.D. Jaggi, A. Franco-Obregon, P. Studerus, and K. Ensslin. Detailed analysis of forces influencing lateral resolution for q-control and tapping mode. *Applied Physics Letters*, 79(1):135–7, 2001.

[65] T. Sulchek, R. Hsieh, J.D. Adams, G.G. Yaralioglu, S.C. Minne, C.F. Quate, J.P. Cleveland, A. Atalar, and D.M. Adderton. High-speed tapping mode imaging with active q control for atomic force microscopy. *Applied Physics Letters*, 76(11):1473–5, 2000.

[66] J.H. Smith, S. Montague, J.J. Sniegowski, J.R. Murray, and P.J. McWhorter. Embedded micromechanical devices for the monolithic integration of mems with cmos. *Electron Devices Meeting, 1995., International*, pages 609–612, 1995.

[67] A.V. Chavan and K.D. Wise. A monolithic fully-integrated vacuum-sealed cmos pressure sensor. *IEEE Transactions of electron devices*, 49(1):164–169, 2002.

[68] C. Hierold. Intelligent cmos sensors. *Micro Electro Mechanical Systems, 2000. MEMS 2000. The Thirteenth Annual International Conference on*, pages 1–6, 2000.

[69] S. Chang, M. Chia, P. Castillo-Borelley, W. Higdon, Q. Jiang, J. Johnson, L. Obedier, M. Putty, Q. Shi, D. Sparks, and S. Zarabadi. An electroformed cmos integrated angular rate sensor. *Sensors and Actuators A*, 66:138–143, 1998.

[70] D.R. Sparks, X. Huang, W. Higdon, and J.D. Johnson. Angular rate sensor and acceleromater combined on the same micromachined cmos chip. *Microsystem Technologies*, 4:139–142, 1998.

[71] D. Lange, C. Hagleitner, O. Brand, and H. Baltes. Cmos resonant beam gas sensor with integrated preamplifier. *Transducers '99 Technical Digest*, pages 1020–1023, 1999.

[72] T. Akiyama, U. Staufer, N.F. de Rooij, D. Lange, C. Hagleitner, O. Brand, H. Baltes, A. Tonin, and H.R. Hidber. Integrated atomic force microscopy array probe with metal-oxide-semiconductor field effect transistor stress sensor, thermal bimorph actuator and on-chip complementary metal-oxide semiconductor electronics. *Journal of Vacuum Science and Technology B*, 18(6):2669–2675, 2000.

[73] D. Lange, T. Akiyama, C. Hagleitner, A. Tonin, H.R. Hidber, P. Niedermann, U. Staufer, N.F. de Rooij, O. Brand, and H. Baltes. Parallel scanning afm with on-chip circuitry in cmos technology. *Technical Digest of MEMS 1999*, pages 447–452, 1999.

[74] U. Drodofsky, M. Drewsen, T. Pfau, S. Nowack, and J. Mlynek. Atom lithography using light forces. *Microelectronic Engineering*, 30(1-4):383–386, 1996.

[75] A.S. Bell, B. Brezger, U. Drodofsky, S. Nowak, T. Pfau, J. Stuhler, Th. Schulze, and J. Mlynek. Nano-lithography with atoms. *Surface Science*, 433-435:40–47, 1999.

[76] M. Henini. Molecular beam epitaxy: From research to manufacturing. *Thin Solid Films*, 306(2):331–337, 1997.

[77] V.M. Mecea, J.O. Carlsson, P. Heszler, and M. Bartan. Development and testing of a high temperature quartz crystal microbalance. *Vacuum*, 46(7):691–694, 1995.

[78] V.M. Mecea, J.O. Carlsson, and R.V. Bucur. Extensions of the quartz-crystal-microbalance technique. *Sensors and Actuators A: Physical*, 53(1-3):371–378, 1996.

[79] N. Taniguchi. *Nanotechnology - Integrated processing systems for ultra-precision and ultra-fine products*. Oxford Science Publications, 1996.

[80] A. Wolde. *Nanotechnology*. Stichting Toeomstbeeld der Techniek, Den Haag, 1998.

[81] Z.J. Davis. Fabrication and characterization of nano-resonator devices. Master's thesis, Technical University of Denmark, 1999.

[82] Clark T.-C. Nguyen and Roger T. Howe. Integrated cmos micromechanical resonator high-q oscillator. *IEEE Journal of Solid-State Circuits*, 34(4):440–455, 1999.

[83] W.C. Tang, T.-C.H. Nguyen, M.W. Judy, and R.T. Howe. Electrostatic-comb drive of lateral polysilicon resonators. *Sensors and Actuators A (Physical)*, A21(1-3):328–31, 1990.

[84] U. Durig, H.R. Steinauer, and N. Blanc. Dynamic force microscopy by means of the phase-controlled oscillator method. *Journal of Applied Physics*, 82(8):3641–51, 1997.

[85] G. Stemme. Resonant silicon sensors. *J. Micromech. Microeng.*, 1:113–125, 1991.

[86] D.W. Carr, S. Evoy, L. Sekaric, H.G. Craighead, and J.M. Parpia. Measurement of mechanical resonance and losses in nanometer scale silicon wires. *Applied Physics Letters*, 75(7):920–2, 1999.

[87] Yie He, James Marchetti, and Carlos Gallegos. General contact and hysteresis analysis of multi-dielectric mems devices under thermal and electrostatic actuation. *Micro-Electro-Mechanical Systems (MEMS) and American Society of Mechanical Engineers, Dynamic Systems and Control Division (Publication) DSC*, 66:323–328, 1998.

[88] O. Hansen, J.T. Ravnkilde, U. Quaade, K. Stokbro, and F. Grey. Field-induced deformation as a mechanism for scanning tunneling microscopy based nanofabrication. *Physical Review Letters*, 81(25):5572–5, 1998.

[89] N. Taniguchi. *Nanotechnology, Integrated processing systems for ultra-precision and ultra-fine products*. Oxford University Press, 1996.

[90] A. Boisen, A.K. Birkelund, O. Hansen, and F. Grey. Fabrication of submicron suspended structures by laser and atomic force microscopy lithography on aluminum combined with reactive ion etching. *Journal of Vacuum Science and Technology B (Microelectronics and Nanometer Structures)*, 16(6):2977–81, 1998.

[91] K. Birkelund. *Nanolithography on Hydrogen-Passivated Silicon*. PhD thesis, Mikroelektronik Centret, 1997.

[92] H. Dirac. *Laser micromachining of silicon*. PhD thesis, MIC, 1997.

[93] M. Mullenborn, M. Heschel, U.D. Larsen, H. Dirac, and S. Bouwstra. Laser direct etching of silicon on oxide for rapid prototyping. *Journal of Micromechanics and Microengineering*, 6:49–51, 1996.

[94] M. Sitti and H. Hashimoto. Controlled pushing of nanoparticles: Modeling and experiments. *IEEE/ASME Transactions on mechatronics*, 5(2):199–211, 2000.

[95] Roe-Hoan Yoon and Subramanian Vivek. Effects of short-chain alcohols and pyridine on the hydration forces between silica surfaces. *Journal of Colloid and Interface Science*, 204(1):179–186, 1998.

[96] R. Garca, M. Calleja, and F. Perez-Murano. Local oxidation of silicon surfaces by dynamic force microscopy: nanofabrication and water bridge formation. *Applied Physics Letters*, 72(18), 1998.

[97] R. Garca, M. Calleja, and H. Rohrer. Patterning of silicon surfaces with noncontact atomic force microscopy: Field-induced formation of nanometer-size water bridges. *Journal of Applied Physics*, 86(4), 1999.

[98] K. Morimoto, Francesc Perez-Murano, and J.A. Dagata. Density variations in scanned probe oxidation. *Applied Surface Science*, 158(3-4):205–216, 2000.

[99] M. Calleja and R. Garca. Nano-oxidation of silicon surfaces by noncontact atomic-force microscopy: Size dependence on voltage and pulse duration. *Applied Physics Letters*, 76(23):3427–3429, 2000.

[100] Z.J. Davis, G. Abadal, O. Kuhn, O. Hansen, F. Grey, and A. Boisen. Fabrication and characterization of nanoresonating devices for mass detection. *Journal of Vacuum Science and Technology B: Microelectronics and Nanometer Structures*, 18(2):612–616, 2000.

[101] J. Bienstman, H.A.C. Tilmans, E.J.E.A. Peeters, M. Steyaert, and R. Puers. An oscillator circuit for electrostatically driven silicon-based one-port resonators. *Sensors and Actuators A: Physical*, 52(1-3):179–186, 1996.

[102] U. Durig, H.R. Steinauer, and N. Blanc. Dynamic force microscopy by means of the phase-controlled oscillator method. *Journal of Applied Physics*, 82(8):3641–51, 1997.

[103] B. Heidari, A. Bogdanov, M. Keil, and L. Montelius. Imprint lithography for mass production. *Microprocesses and Nanotechnology Conference, 2001 International*, pages 94–95, 2001.

[104] J. Buhler, F.-P. Steiner, and H. Baltes. Silicon dioxide sacrificial layer etching in surface micromachining. *Journal of Micromechanics and Microengineering*, 7(1):R1–R13, 1997.

[105] N. Takeshima, K.J. Gabriel, M. Ozaki, J. Takahashi, H. Horiguchi, and H. Fujita. Electrostatic parallelogram actuators. *Solid-State Sensors and Actuators, 1991. Digest of Technical Papers, TRANSDUCERS '91., 1991 International Conference on*, pages 63–66, 1991.

[106] D. Kobayashi, C.-J. Kim, and H. Fujita. Photoresist-assisted release of movable microstructures. *Japanese Journal of Applied Physics, Part 2 (Letters)*, 32(11A):L1642–4, 1993.

[107] B.K. Smith, J.J. Sniegowski, G. La Vigne, and C. Brown. Thin teflon-like films for eliminating adhesion in released polysilicon microstructures. *Sensors and Actuators A: Physical*, 70(1-2):159–163, 1998.

[108] H.V. Jansen, J.G.E. Gardeniers, J. Elders, H.A.C. Tilmans, and M. Elwenspoek. Applications of fluorocarbon polymers in micromechanics and micromachining. *Sensors and Actuators, A: Physical*, 41(1):136–140, 1994.

[109] Yoshinori Matsumoto and Makoto Ishida. The property of plasma-polymerized fluorocarbon film in relation to ch_4 c_4f_8 ratio and substrate temperature. *Sensors and Actuators A: Physical*, 83(1-3):179–185, 2000.

[110] P.F. Man, B.P. Gogoi, and C.H. Mastrangelo. Elimination of post-release adhesion in microstructures using conformal fluorocarbon coatings. *Microelectromechanical Systems, Journal of*, 6(1):25–34, 1997.

[111] R.L. Alley, G.J. Cuan, R.T. Howe, and K. Komvopoulos. The effect of release-etch processing on surface microstructure stiction. *Solid-State Sensor and Actuator Workshop, 1992. 5th Technical Digest., IEEE*, pages 202–207, 1992.

[112] D.A. Neamen. *Semiconductor Physics and Devices - basic principles*. McGraw-Hill Companies, 1997.

[113] G. Abadal, A. Boisen, Z.J. Davis, O. Hansen, and F. Grey. Device physics - combined laser and atomic force microscope lithography on aluminum: Mask fabrication for nanoelectromechanical systems. *Applied Physics Letters*, 74(21):3206–3208, 1999.

[114] G. Abadal, Z.J. Davis, A. Boisen, F. Prez-Murano, N. Barniol, and X. Borris. Combining laser and jumping mode afm lithography on aluminum for the fabrication of nanoelectromechanical devices. *Probe Microscopy*, 2(2):121–128, 2001.

[115] Z.J. Davis, G. Abadal, O. Hansen, X. Boris, N. Barniol, F. Prez-Murano, and A. Boisen. Afm lithography of aluminum for fabrication of nanomechanical systems. *Accpeted to Ultramicroscopy*, 2003.

[116] P.J. de Pablo andJ. Colchero, J. Gmez-Herrero, and A.M. Bar. Jumping mode scanning force microscopy. *Applied Physics Letters*, 73(22):3300–3302, 1998.

[117] F. Moreno-Herrero, P.J. de Pablo, R. Fernndez-Snchez, J. Cochero, J. Gmez-Herrero, and A.M. Bro. Scanning force microscopy jumping and tapping modes in liquids. *Applied Physics Letters*, 81(14):2620–2622, 2002.

[118] R. Garcia and A. San Paulo. Attractive and repulsive tip-sample interaction regimes in tapping-mode atomic force microscopy. *Physical Review B (Condensed Matter)*, 60(7):4961–7, 1999.

[119] Ricardo Garcia and Alvaro San Paulo. Dynamics of a vibrating tip near or in intermittent contact with a surface. *Physical Review - Section B - Condensed Matter*, 61(20):R13381, 2000.

[120] E.W. Balch, S.E. Weaver, and R.J. Saia. Characterization of a submicron image reversal process. *Proceedings of the SPIE - The International Society for Optical Engineering*, 922:387–394, 1988.

[121] http://www.microchem.com/products/lor.htm.

[122] Heinz Schmid, Hans Biebuyck, Bruno Michel, and Olivier J.F. Martin. Light-coupling masks for lensless, sub-wavelength optical lithography. *Applied Physics Letters*, 72(19):2379–2381, 1998.

[123] O.J.F. Martin. Breaking the diffraction limit with plasmon optics: 20nm optical lithography using 600nm illumination wavelength. *Proceeding of Micro- and Nanoengineering International Conference*, pages 98–99, 2002.

[124] H. Schmid, H. Biebuyck, B. Michel, O.J.F. Martin, and N.P. Piller. Light-coupling masks: An alternative, lensless approach to high-resolution optical contact lithography. *Journal of Vacuum Science and Technology B (Microelectronics and Nanometer Structures)*, 16(6):3422–5, 1998.

[125] E. Buks and M.L. Roukes. Stiction, adhesion energy, and the casimir effect in micromechanical systems. *Physical Review B (Condensed Matter)*, 63(3):033402/1–4, 2001.

[126] E Buks and M L Roukes. 60 condensed matter: Structural, mechanical and thermal properties - metastability and the casimir effect in micromechanical systems. *Europhysics Letters*, 54(2):220–226, 2001.

[127] E. Buks and M.L. Roukes. Electrically tunable collective response in a coupled micromechanical array. *Microelectromechanical Systems, Journal of*, 11(6):802–807, 2002.

[128] T. Corman, P. Enoksson, and G. Stemme. Gas damping of electrostatically excited resonators. *Sensors and Actuators A: Physical*, 61(1-3):249–255, 1997.

[129] Eung-Sam Kim, Young-Ho Cho, and Moon-Uhn Kim. Effect of holes and edges on the squeeze film damping of perforated micromechanical structures. *Micro Electro Mechanical Systems, 1999. MEMS '99. Twelfth IEEE International Conference on*, pages 296–301, 1999.

[130] Wang Yaqiang, Jin Zhonghe, Wang Yuelin, and Ding Chun. Thermally excited micromechanical vacuum resonator. *Solid-State and Integrated Circuit Technology, 1998. Proceedings. 1998 5th International Conference on*, pages 950–952, 1998.

[131] J. Yang, T. Ono, and M. Esashi. Investigating surface stress: Surface loss in ultrathin single-crystal silicon cantilevers. *Journal of Vacuum Science and Technology B: Microelectronics and Nanometer Structures*, 19(2):551–556, 2001.

[132] D. Saya, K. Fukushima, H. Toshiyoshi, G. Hashiguchi, H. Fujita, and H. Kawakatsu. Fabrication of array of single-crystal si multi probe cantilevers with several microns size for parallel operation of atomic force microscope. *Micro Electro Mechanical Systems, 2001. MEMS 2001. The 14th IEEE International Conference on*, pages 131–134, 2001.

[133] Kirsten Ingolf Schiffmann. Investigation of fabrication parameters for the electron-beam-induced deposition of contamination tips used in atomic force microscopy. *Nanotechnology*, 4(3):163–169, 1993.

[134] P. Boggild, T.M. Hansen, C. Tanasa, and F. Grey. Fabrication and actuation of customized nanotweezers with a 25 nm gap. *Nanotechnology*, 12(3):331–335, 2001.

Appendix A

List of publication

1. G. Abadal, A. Boisen, Z.J. Davis, O. Hansen and F. Grey, "Combined laser and atomic force microscope lithography on aluminum: Mask fabrication for nanoelectromechanical systems", Appl. phys. Lett., 74(21), pp. 3206-3208 (1999).

2. Z.J. Davis, G. Abadal, O. Kuhn, O. Hansen, F. Grey and A. Boisen, "Fabrication and characterization of nano-resonating devices for mass detection", J. Vac. Sci. Technol. B, 18(2), pp. 612-616 (2000).

3. G. Abadal, Z.J. Davis, A. Boisen, F. Prez-Murano, N. Barniol and X. Borris, "Combining Laser and Jumping Mode AFM Lithography on Aluminum for the Fabrication of Nanoelectromechanical Devices", Probe Microscopy 2(2), pp. 121-128 (2001).

4. G. Abadal, Z.J. Davis, B. Helbo, X. Borris, R. Ruiz, A. Boisen, F. Campabadal, J. Esteve, E. Figueras, F. Prez-Murano and N. Barniol, "Electromechanical model of a resonating nano-cantilever-based sensor for high-resolution and high-sensitivity mass detection", Nanotechnology 12, pp. 100-104 (2001).

5. X. Borris, G. Abadal, D. Jimenez, F. Prez-Murano, N. Barniol, Z.J. Davis, and A. Boisen, "Light propagation studies on laser modified waveguides using scanning near-field optical microscopy", IEEE Photonics Technology Letters 13(8), pp. 809-811 (2001).

6. G. Abadal. Z.J. Davis, O. Hansen, X. Borris, A. Boisen, N. Barniol, and F. Prez-Murano, "AFM characteriation of a resonating nanocantilever", Accepted in Ultramicroscopy (2003).

7. Z.J. Davis, G. Abadal. O. Hansen, N. Barniol, F. Prez-Murano and A. Boisen, "AFM lithography of aluminum for fabrication of nanomechanical systems", Accepted in Ultramicroscopy (2003).

8. Z.J. Davis, G. Abadal, B. Helbo, O. Hansen, F. Campabadal, F. Prez-Murano, J. Esteve, E. Figueras, R. Ruiz, N. Barniol, A. Boisen, "Monolithic integration of mass sensing nano-cantileves with CMOS circuitry", Accepted in Sensors and Actuators (2003).

9. A. Boisen, G. Abadal, Z.J. Davis, O. Hansen and F. Grey, "Laser and AFM lithography on aluminum: a toolbox for fabrication of nanoelectromechanical structures", Proceedings of STM99, pp. 337-338, (Seoul 1999).

10. Z.J. Davis, G. Abadal, B. Helbo, O. Hansen, F. Grey and A. Boisen, "Nanocantilever devices for mass detection - fabrication and characterization", Proceedings of the 1st euspen topical conference on fabrication and metrology in nanotechnology, pp. 81-89 (Copenhagen 2000).

11. G. Abadal, Z.J. Davis, B. Helbo, R. Ruiz, F. Prez-Murano, F. Campabadal, J. Esteve, E. Figueras, A. Boisen and N. Barniol, "Nanomechanical devices for mass detection realized by laser and atomic force microscopy lithography and compatible with CMOS technology", Proceedings of Eurosensors XIV, pp. 487-490 (Copenhagen 2000).

12. G. Abadal, N. Barniol, A. Boisen, F. Campabadal, Z.J. Davis, J. Esteve, E. Figueras, B. Helbo, F. Perez-Murano and R. Ruiz, "Nanocantilever integrated with CMOS circuitry for high sensitivity mass detection", Proceedings of Ibersensor 2000 (Buenos Aires 2000).

13. Z.J. Davis, G. Abadal, B. Helbo, O. Hansen, F. Campabadal, F. Prez-Murano, J. Esteve, E. Figueras, R. Ruiz, N. Barniol, A. Boisen, "High mass and spatial resolution mass sensor based on resonating nano-cantilevers integrated with CMOS circuitry", Proceedings of Transducers 01, pp. 72-75 (Munich 2001).

14. Z.J. Davis, G. Abadal, B. Helbo, O. Hansen, F. Campabadal, F. Prez-Murano, J. Esteve, E. Figueras, R. Ruiz, N. Barniol, A. Boisen, "High mass and spatial resolution mass sensor based on resonating nano-cantilevers integrated with CMOS circuitry", Proceedings of STM '01, pp. 47 (Vancover 2001).

15. N. Barniol, G. Abadal, X. Borris, F. Prez-Murano, J. Verd, M. Villarroya, Z.J. Davis, A. Boisen, F. Campabadal, E. Figueras, J. Esteve, J. Monserrat, S.G. Nilsson, I. Maximov, E-L. Sarwe, L. Montelius, "A mass sensor with atto-gram sensitivity using resonating nanocantilevers", NANO-7, pp. (Malm 2002).

16. F. Prez-Murano, Z.J. Davis, G. Abadal, O. Hansen, X. Borris, A. Boisen and N. Barniol, "AFM characterization of a resonating nanocantilever", NANO-7, pp. (Malm 2002).

17. F. Prez-Murano, Z.J. Davis, J. Monserrat, G. Abadal, X. Borris, J. Verd, O. Hansen, A. Boisen, N. Barniol, "Nanopatterning by AFM nano-oxidation of thin aluminum layers as a tool for prototypin of nanoelectromechanical systems", Proceeding of MNE 2002, pp. 272-273 (Lugano 2002).

Appendix B

SUGAR program

Main SUGAR program:

```
%%%%%%%%%%%%%%%%%%%%%%%%%%%%%%%%%%%%%%%%%%%%%%%%%%%%%%%%%%%%%%%%
%                                                                 %
%                    CANTILEVER- DRIVER STRUCTURE                 %
%
%%%%%%%%%%%%%%%%%%%%%%%%%%%%%%%%%%%%%%%%%%%%%%%%%%%%%%%%%%%%%%%%
clear all; clc;
path=('c:\zach\matlab');
model='nanomass.net';
global alphak
alphak=1; %fringe factor
% GEOMETRICAL PARAMETERS
% Modify for each structure
g=0e-6;
ladd=0e-6;
lcant=39.8e-6;
wcant=1.14e-6;
dgap=2.36e-6;
dadd=0e-6;
h=1.8e-6;
%Voltage applied
V=130; %Volts
%%%%%%%%%%%%%%%%%%%%%%%%%%%%%%%%%%%%%%%%%%%%%%%%%%%%%%%%%%%%%%%%
%%%%%%%%%%%%%%%%%%%%%%%%%%%%%%%%%%%%%%%%%%%%%%%%%%%%%%%%%%%%%%%%
param.g=g; param.ladd=ladd; param.lcant=lcant;  param.wcant=wcant;
param.dgap=dgap; param.dadd=dadd; param.h=h;
%%%%%%%%%%%%%%%%%%%%%%%%%%%%%%%%%%%%%%%%%%%%%%%%%%%%%%%%%%%%%%%%
%%%%%%%%%%%%%%%%%%%%%%%%%%%%%%%%%%%%%%%%%%%%%%%%%%%%%%%%%%%%%%%%
% STEP 1. DYSPLAYING THE STRUCTURE- EQUILIBRIUM-
figure(1);
param.V=0;
net=cho_load(model,param);
cho_display(net);
title('System Cantilever-Driver');
xlabel('Horizontal dimension [m]');
ylabel('Vertical dimension [m]');
%%%%%%%%%%%%%%%%%%%%%%%%%%%%%%%%%%%%%%%%%%%%%%%%%%%%%%%%%%%%%%%%
%%%%%%%%%%%%%%%%%%%%%%%%%%%%%%%%%%%%%%%%%%%%%%%%%%%%%%%%%%%%%%%%
% STEP 2. DYSPLAYING THE DEFLECTED STRUCTURE
figure(2);
param.V=V;
net=cho_load(model,param);
dq=[];K=[];f=[];
[dq]=cho_dc(net,dq);
cho_display(net,dq);
%%%%%%%%%%%%%%%%%%%%%%%%%%%%%%%%%%%%%%%%%%%%%%%%%%%%%%%%%%%%%%%%
if ladd==0
    displacement = cho_dq_view(dq,net,'c','y')
else
    displacement = cho_dq_view(dq,net,'s','y')
end
%%%%%%%%%%%%%%%%%%%%%%%%%%%%%%%%%%%%%%%%%%%%%%%%%%%%%%%%%%%%%%%%%
title('System Cantilever-Driver');
xlabel('Horizontal dimension [m]');
ylabel('Vertical dimension [m]');
%%%%%%%%%%%%%%%%%%%%%%%%%%%%%%%%%%%%%%%%%%%%%%%%%%%%%%%%%%%%%%%%
```

netist file containing material information:

```
process poly = [
    Poisson = 0.3              % Poisson's Ratio = 0.3
    thermcond = 2.33       % Thermal conductivity Si = 2.33e-6/C
    viscosity = 1.78e-5      % Viscosity (of air) = 1,78e-5
    %viscosity = 0            % Viscosity of vacum
    fluid = 2e-5                 %  Between the device and the substr  ↙
ate.
    %fluid = 0               %  Between the device and the substrate.

    density = 2.33e3        %Material density = 2.33e3 kg/m^3
    Youngsmodulus = 1.6e11  %Young's modulus = 1.65e11 N/m^2

    permittivity = 8.854e-12    %permittivity: C^2/(uN.um^2)=(C.s)^2/  ↙
kg.um^3;

    sheetresistance = 20    %Poly-Si sheet resistance [ohm/square]
    stress = 0
    straingradient=0
    thermalexpansion=0
    ambienttemperature=300
]

process p1 : poly = [
    h = 0.6e-6          %Layer height of mcnc poly1 = 0.6e-6 meters
]

process p2 : poly = [
    h = 1.5e-6          %Layer height of mcnc poly2 = 1.5e-6 meters
]

process p3 : poly = [
    h = 0.6e-6          %Layer height of mcnc poly2 = 0.6e-6 meters
]

process d2 : poly = [
    fluid = 0.75e-6     %Fluid layer thickness p1:p2 = 0.75e-6 meters  ↙
.
]
```

netist file containing device information:

```
uses material.net
uses stdlib.net

param V=0
param lcant=40u
param wcant=1u
param lanc=10u
param wanc=10u
param dgap=1u
param wdrv=10u
param g=0u
param ladd=0u
param dadd=0u
param h=2u

Vsrc          * [a e] [V=V]
eground   * [e] []

anchor       p1 [l]             [l=-lanc w=wanc h=h  oz=3*pi/2 ]
beam2de   p1 [a l]          [l=lanc/2 w=wcant R=100 h=h]
anchor       p1 [a]             [l=lanc w=wcant h=h]
anchor     p1 [l]             [l=lanc/2 w=wcant h=h]
beam2de   p1 [l b]          [l=lanc/2 w=wcant R=100 h=h]

if (g==0) [
    gap2de     p1 [b c d e]   [l=lcant-ladd w1=wcant w2=wdrv oz=0 gap  ↙
=dgap  h=h R1=100 R2=100]
]
else [
    beam2de p1 [b f]          [l=g w=wcant h=h R=100]
    gap2de     p1 [f c d e]   [l=lcant-g-ladd w1=wcant w2=wdrv oz=0 g  ↙
ap=dgap h=h  R1=100 R2=100]
]
anchor      p1 [d]           [l=lcant-g-ladd w=wdrv h=h]

if (ladd!=0)[
    beam2de p1 [c s]          [l=ladd w=wcant h=h R=100]
]

if (dadd!=0)[
   beam2de p1 [e t]         [l=dadd w=wdrv h=h R=100]
   anchor     p1 [e]              [l=dadd w=wdrv h=h]
]
```

Appendix C

CMOS post processing sequence using laser lithography

1. **Al deposistion**: 7nm of Al is deposited onto the CMOS chip using e-beam evaporation at 5Åper second.
2. **Laser writing**: The cantilever/electrode pattern is directly written at an incident power of between 10-20mW.
3. **Al etch**: The unexposed Al is etched in 80% H_3PO_4 between 2-6 minutes.
4. **Poly0 etch**: The poly0 layer in the nanoarea is anisotropically etched for 7minutes. Recipe zd_aniso: 32 sccm SF_6, 8 sccm O_2, Pressure=80mTorr and Power=35W.
5. **HMDS**: The chip is baked in vacuum and HMDS treated for 30min.
6. **Resist spinning**: Resist is spun onto the chip at 1500rpm for 30sec. resulting in a 2.5μ thick resist coating.
7. **Resist baking**: The resist is baked at 110^0C for 2minutes.
8. **UV lithography**: Mask 1, The chip is exposed for 60sec. and developed for 60sec. Holes are opened over the nanoarea.
9. **BHF underetching**: The 1μ sacrificial oxide is etched in BHF for 15minutes at an etch rate of 75nm per minute.
10. **Dry release**: See Appendix D and E
11. **CMOS annealing**: The chip is annealed for 20min at 350^0C.

Appendix D

Freeze-drying process sequence

1. **DI water rinse**: The chip placed and rinsed in DI water 3-5 times without drying the chip at any point.
2. **Resist removal**: The chip is placed in acetone for 10 minutes to remove the protection resist. The chip is then rinsed 3-5 times in acetone without drying the chip.
3. **Propanol rinse**: The chips is rinsed in propanol 3-5 times without drying the chip.
4. **Tert-butanol**: The chip is immersed in liquid tert-butanol that has been heated to 30^0C.
5. **Freezing**: The chip is then placed on a cooling plate and the terr-butanol freezes.
6. **Evaporation**: The chip is placed in vacuum with a cooling plate and the solid tert-butanol slowly evaporates for about 1hour.

Appendix E

Resist-release process sequence

1. **DI water rinse**: The chip placed and rinsed in DI water 3-5 times without drying the chip at any point.
2. **Resist removal**: The chip is placed in acetone for 10 minutes to remove the protection resist. The chip is then rinsed 3-5 times in acetone without drying the chip.
3. **Resist rinse**: The chip in a slight amount of acetone is diluted with resist.
4. **Resist spin**: The chip is spun at 3000rpm for 30sec. to evenly distribute the resist on the chip.
5. **Resist etch**: The resist is removed in the RIE. Recipe PR_STRIP: 99sccm O_2, 20sccm N_2, pressure=300mTorr and power= 60W. Etch rate 430nm/minute.

Appendix F

Al cantilever process sequence

1. **Resist spin**: The chip is spun at 6000rpm for 30seconds to evenly distribute the resist on the chip at a thickness of 600nm.
2. **Resist bake**: The chip is baked at 90^0C for 30 seconds.
3. **Exposure1, metalmask1**: Expose resist for approximately 3 seconds.
4. **Post exposure bake**: Post bake wafer at 120^0C for 120seconds.
5. **Flood exposure**: Expose wafer for 30seconds without any mask.
6. **Development**: Develop resist with a NaOH solution for 75 seconds.
7. **Al deposition**: Deposition of Al metal at a thickness of 100nm.
8. **Al lift-off**: Lift off resist with Al by acetone and ultrasound for 5 minutes.
9. **Thick resist spin**: The chip is spun with a thick resist in order to deposit a 10μ thick resist layer.
10. **Exposure2 and development, ASE mask2**: Expose resist for approximately 30 seconds and develop the resist for 5 minutes.
11. **ASE etch**: Groves are etched into the front side using the thick resist as a mask. The recipe is "shallow etch" and a depth of 100μm is etched.
12. **Resist strip**: Strip resist using acetone and ultrasound.
13. **RIE underetching**: Underetch Al structure by isotropically etching the Si underneath the Al for 5-10 minutes. Recipe ab_iso: 40sccm SF_6, p=80mTorr, P=30W.